Contents lists available at ScienceDirect

Progress in Polymer Science

journal homepage: www.elsevier.com/locate/progpolymsci



Best practices and recommendations for accurate nanomechanical characterization of heterogeneous polymer systems with atomic force microscopy



David W. Collinson^{a,1}, Richard J. Sheridan^b, Marc J. Palmeri^b, L. Catherine Brinson^{b,*}

- ^a Department of Mechanical Engineering, Northwestern University, Evanston, Illinois, 60208, USA
- ^b Department of Mechanical Engineering and Materials Science, Duke University, Durham, North Carolina, 27708, USA

ARTICLE INFO

Article history: Received 18 September 2020 Accepted 24 May 2021 Available online 9 June 2021

Keywords: Atomic force microscopy soft materials nanoscale polymers indentation viscoelasticity calibration

ABSTRACT

The past two decades have seen atomic force microscopy (AFM) evolve from an experimental technique to probe simple surface topography to one that can spatially map nanoscale material properties with exquisite sensitivity and high resolution. An expanding array of modes and analysis methods has made AFM a widely used technique for extracting nanoscale elastic and viscoelastic data from polymers and other soft materials. However, the assumptions required for interpretation of nanoscale mechanical data on polymers and the lack of clarity on the best practices for the different modes limits the quantitative accuracy of AFM methods and the interpretation of mechanical data. The analysis of AFM data becomes even more complex when multiple phases are present in a sample which further convolute measurements and the interpretation of the output data. Here, we present a comprehensive summary of modes and contact mechanics analyses relevant for AFM on polymers, along with assessment of sources of error and potential artifacts in measurement data on these soft, adhesive, viscoelastic and often heterogenous materials. As a result of the review into AFM best practices, we provide a series of recommendations for conducting quantitative AFM measurements on polymer systems. Finally, we investigate the impact of these advancements in the context of a specific case study: measurement of mechanical property gradients in nanostructured polymers.

© 2021 Elsevier B.V. All rights reserved.

Abbreviations: AFM, atomic force microscopy: AM, amplitude modulated; AMAC, amplitude modulated approach curve; BE, band excitation; BIMS, poly(isobutylene-co-p-methylstyrene); CNT, carbon nanotube; CR, contact resonance; DART, dual AC resonance tracking; DMA, dynamic mechanical analysis; DMT, Derjaguin, Muller, and Toporov; DPPC, (1,2-dipalmitoylsn-glycero-3-phosphocholine); DSI, dynamic scanning indentation; FEA, finite element analysis; FM, frequency modulated; FV, force volume; HNBR, hydrogenated nitrile butadiene rubber; IR, isoprene rubber; JKR, Johnson, Kendall, and Roberts; LDV, laser doppler vibrometry; LVDT, linear variable differential transformer; MAPP, malleated polypropylene; MD, molecular dynamics; NMR, nuclear magnetic resonance; PBAT, poly(butylene-adipate-co-terephthalate);PC, poly(carbonate); PCL, poly(caprolactone); PDMS, poly(dimethylsiloxane); PEDOT: PSS, poly(3,4-ethylenedioxythiophene)-poly(styrenesulfonate); PEMA. methacrylate); PFM, pulsed force mode; PiBMA, poly(isobutyl methacrylate); PLA, poly(lactic acid); PM, phase modulated; PMMA, poly(methyl methacrylate); PnBMA, poly(n-butyl methacrylate); PNC, polymer nanocomposite; PP, poly(propylene); PS, poly(styrene); PtBuA, poly(tert-butyl acrylate); PVA, poly(vinyl alcohol); PVAc, poly(vinyl acetate); SBR, styrene-butadiene rubber; SCO, spin cross-over; SEBS, styrene-b-ethylene-co-butylene-b-styrene; SEM, scanning electron microscopy; SIS, sequential infiltration synthesis; STZ, shear transformation zone; TEM, transmission electron microscopy; UV, ultra-violet; VE, viscoelastic.

Corresponding Author

E-mail addresses: davidcollinson2020@u.northwestern.edu (D.W. Collinson), richard.sheridan@duke.edu (R.J. Sheridan), marc.palmeri@duke.edu (M.J. Palmeri), cate.brinson@duke.edu (L.C. Brinson).

¹ Currently at Department of Materials Science, Stanford University, Stanford, California, 94305, USA.

1. Introduction

1.1. Nanomechanical mapping with AFM

Since atomic force microscopy (AFM) was developed in the 1980s, [1] AFM has been used for the characterization of surfaces and their properties by scanning a sharp tip attached to the end of a cantilever across a sample surface, where deflections of the cantilever can be related to nanoscale changes in surface topography and properties.

Since then, the past two decades have seen the rise of an expanding range of AFM modes and techniques [2-6] that map nanoscale mechanical properties with ever growing sophistication, transforming AFM into an indispensable tool for the characterization of the nanoscale properties of polymers and other soft materials. [7-9] Depending on the choice of the excitation signal and feedback mechanism(s) a range of quasi-static and dynamic AFM operational modes can be accessed. Quasi-static AFM modes, also commonly referred to as static modes, conduct force spectroscopy measurements by driving the tip of an AFM cantilever into contact with a sample surface while tracking the cantilever deflection as a function of the probe movement towards and into the sample. Dynamic AFM modes excite the cantilever at a specified frequency or range of frequencies close to the cantilever resonance while the tip is near (commonly referred to as 'non-contact mode'), or in intermittent contact (commonly referred to as 'tapping mode') with, a sample surface where perturbations to the cantilever oscillation behavior due to tip-sample forces allows the user to infer information about the surface properties. Table 1 provides a brief summary of current quasi-static and dynamic AFM modes and their capabilities for measuring mechanical properties. Beyond the "simple" acquisition of sample topography conducted by traditional AFM, the advanced modes have been developed to measure electrical, thermal, surface chemistry, [10] as well as mechanical properties - the focus of this review - which provide sources of contrast between sample components that is not available from other high resolution imaging techniques (SEM, TEM, etc.).

Despite the numerous advancements in AFM methods, the viscoelastic (VE), adhesive nature of polymers and soft materials presents a significant challenge in quantitative AFM measurement due to complex contact mechanics and non-linear sample deformation. Multi-phase materials provide additional complications to AFM measurement as the response of a material to AFM indentation is a convolution of contributions from a volume underneath the AFM tip and may include several phases. At the same time, local property measurements are the most insightful on multi-phase systems to shed light on complex material interactions. Perhaps the most well-known consequence of the finite probed volume is the 'substrate effect' (also known as the 'thin film effect' or 'stress interaction effect') where the measured force from an indentation into a sufficiently thin film will have a contribution from the supporting substrate, artificially increasing or decreasing the measured modulus of the film depending on the relative stiffness of the substrate.[39] While most well-known for its relevance in the study of supported thin films, the substrate effect is also an important consideration in the study of composite and blend systems generally, as the various bodies in the sample can influence indentations in the neighboring phase.

1.2. AFM and complex soft materials

1.2.1. Nanostructured polymers and the interphase

One of the most promising areas for local property measurement of polymers by AFM is in elucidating the nature of the polymer interphase. The interphase is a nanoscale (1-100 nm) region of polymer with altered properties relative to bulk regions resulting from chemical and/or physical interactions between local polymer chains and the surface of a neighboring domain. The changes in polymer conformations and dynamics within the interphase is thought to be responsible for many of the enhanced mechanical, dielectric, transport, and thermal properties observed in thin films and polymer nanocomposites (PNCs). [40,41] Polymer thin films, supported thin films in particular, [42] are in some ways analogous to PNCs due to similarities between the interactions of local polymer chains with an embedded nanoparticle and with a stiff chemically active surface. Advancements in understanding of the interphase impacts a variety of application domains including microelectronics and energy storage devices, drug delivery systems, structural composites and nanocomposites, polymer blends, polymer adhesion and tribology.

The interphase layer and its formation also tell a fundamental story about polymers and the underlying material physics. As-

pects of glass formation remain an unsolved problem in solid state physics, [43,44] with multiple theories still competing to explain the mechanisms of how a glass-former (such as a polymer) undergoes such drastic change in physical properties at the glass transition temperature. The ability to understand the interphase morphology, its local properties, and how it arises in real systems can provide useful information about entanglement, chemistry, and glass formation in polymers.

The drive in computational materials science towards big data and machine learning approaches to the development of novel materials requires high fidelity data sets with accurate representation of the sample microstructure for quantification and prediction. [45] Beyond the enormous range of material constituents available for fabricating PNCs, the interactions between filler particles and polymers add an additional wrinkle to attempts to predict or tailor the macroscale properties. Nanomechanical AFM has the potential for direct measurement of the impact of constituent materials and their interactions on the interphase and microstructure in heterogenous systems such as PNCs. However, conducting nanomechanical AFM on PNCs remains a significant challenge as the multiple phases present result in changes to deformation behavior and local sample topography, among other issues, that require careful treatment for quantitative measurements.

1.2.2. Biological materials and indentation on cellular bodies

AFM has seen significant use in characterization of biological materials and indentation measurements of the mechanical properties of cells, bacteria, proteins, and other soft biological systems. While early experiments were limited to static indentations and topography, advancement in high-sensitivity low force AFM modes, [46,47] experimental protocols, [11,14,48,49] and the combination of AFM measurements with complementary techniques [9] have made AFM a sophisticated analysis technique for biological systems. AFM studies on biological systems is a crucial and growing field, and there are several recent reviews on the subject [8,9,50]. Our review is focused on polymers and their composites and blends, but the outcomes and content of our review are broadly applicable to AFM on all soft materials, including biological materials.

1.3. Overview

In this review, we examine recent advances in the elastic and viscoelastic characterization of polymers and the impact of instrument calibration and other experimental considerations. Section 2 is an overview of the AFM modes that are most suitable for nanoscale characterization of elastic and viscoelastic mechanical properties of polymers. We also provide a summary of commonly used contact mechanics models for elastic properties as well as contact models that include viscoelastic material behavior for quasi-static and dynamic AFM modes. Section 3 summarizes sources of error within AFM mechanical property measurements from the calibration procedure as well as the measurement artifacts that result from non-linear deformation behavior and structural effects due to the presence of multiple phases in an indented system. In light of these considerations, we provide some recommendations and best practice for acquiring and interpreting AFM data on polymer systems. Finally in Section 4 we examine recent work on measuring local properties near surfaces in nanostructured polymers in the context of the lessons learned from Sections 2 and 3 and suggest future directions to refine AFM measurements for the detailed measurement of local mechanical properties in complex, heterogeneous polymers.

Table 1Summary of common mechanical AFM modes and their general capability at the time of publication for nanoscale acquisition of elastic and viscoelastic properties. Quasi-static, dynamic and dedicated viscoelastic measurement techniques are highlighted in blue, green, and orange respectively. F is the applied force to the surface, E, E' and E'' are the elastic modulus, storage modulus and loss modulus respectively, ω is the oscillation frequency, tan δ is the loss tangent, η is the material viscosity, and z is the distance between the apex of the cantilever tip and the sample surface. Appropriate cantilever choice for a given sample is required for accurate measurements in any mode, which is discussed further in Section 3.1.3.

Mode (Section)	Schematic	Physics	Viscoelastic Properties ^a	Drive Frequency (Hz) ^b	Compatible Storage Modulus (Pa) ^c	Contact Mechanics ^d	Refs.
Force Volume (2.1)	F(t)	Quasi-Static	$\mathit{E}(t), \eta$	10 ¹ 10 ³ 10 ⁵ 10 ⁷	10 ³ 10 ⁵ 10 ⁷ 10 ⁹ 10 ¹¹	Hertz, JKR, DMT, Sneddon	[2,10-13]
Pulsed Force (2.1)	****	Quasi-Static	$E(t)$, η			Hertz, JKR, DMT, Sneddon	[14-17]
Single Frequency (2.2.2)	F(z)	Dynamic	tan δ^c			-	[18-24]
Multi-frequency (2.2.3)	F(z)	Dynamic	E' , E'' , $ an\delta^e$			Sneddon	[6, 25-28]
Contact Resonance (2.2.4)		Dynamic	E', E"			Hertz, Schwarz	[29-33]
Dynamic Scanning Inden. (2.3.1)	<i>m</i>	Quasi-Static	$E'(\omega), E''(\omega)$			Hertz	[34]
Nano-DMA (2.3.2)	F	Quasi-Static	$E'(\omega),~E''(\omega)$			Hertz, DMT, JKR	[35-38]

 $^{^{}a}$ Generally accessible viscoelastic properties with each operating mode. Inclusion of ω indicates property can be measured over a continuous range of frequencies.

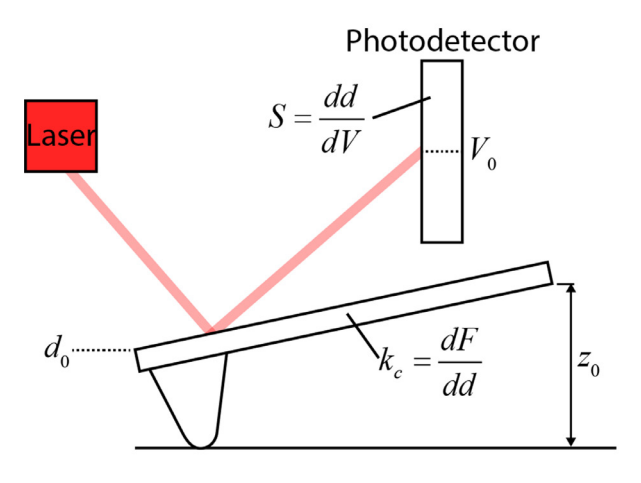
b Available analysis frequencies for dynamic modes are typically limited to the neighborhood of the cantilever eigenfrequencies. Stated values are approximate for free resonance in air or N₂. Quantitative force volume in air is typically limited to 10 Hz and below.

^c Demonstrated compatible storage modulus for quantitative analysis.

^d Commonly used contact mechanics available for analysis.

^e Measures cantilever dissipation which is inclusive of numerous effects as well as material viscoelasticity.

Initial Contact



Indentation

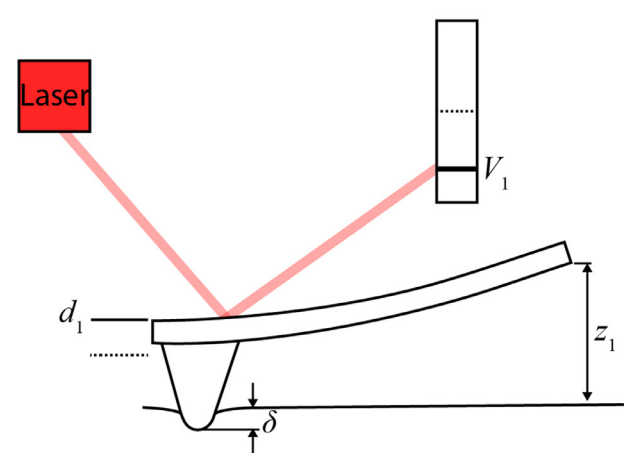


Fig. 1. Schematic of AFM operation during an indentation into a non-adhesive sample.

2. Elastic and Viscoelastic Property Measurement from Quasi-static and Dynamic AFM

The viscoelastic, adhesive nature of polymers make them difficult systems to study with AFM, and so it is often the case that there is not just one AFM technique that works across every system of interest. In this section, we provide an overview of the AFM modes which are most suitable for extraction of elastic and viscoelastic mechanical property data from polymer blends and composites. We first introduce quasi-static modes, then dynamic modes, in each section summarizing methods for elastic and viscoelastic characterization; we include a separate section on several dedicated viscoelastic modes. We also summarize commonly used contact mechanics models for elastic properties as well as contact models that include viscoelastic material behavior.

Central to all nanomechanical AFM techniques is the requirement to measure the forces acting on the tip as a function of the tip displacement towards and into the sample surface. Measuring both the forces acting on the AFM tip and the tip displacement requires independent measurement of the cantilever deflection and displacement. A typical AFM (Fig. 1) uses a four-quadrant photo detector to convert the deflection (d) of a cantilever to a voltage output (V) by tracking the location of a laser spot on the photode-

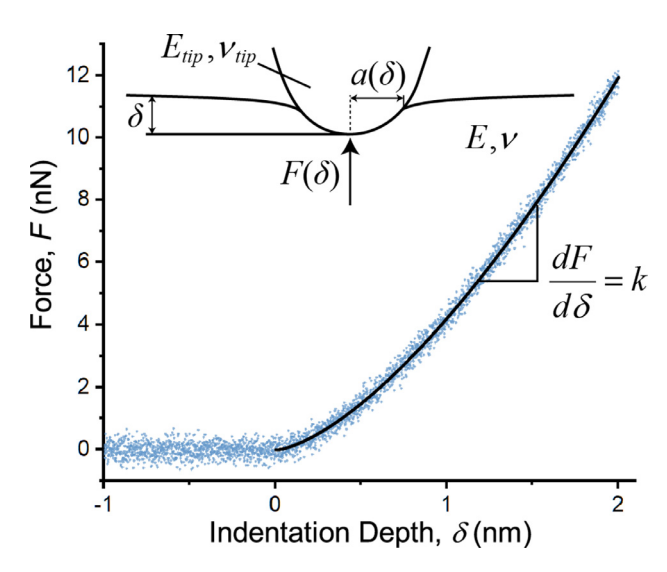


Fig. 2. Simulated experimental force-displacement $(F-\delta)$ curve for the indentation of a parabolic tip into a non-adhesive surface. The black line indicates the tangential slope at a given indentation depth. The gradient of the slope provides the contact stiffness, $k(\delta)$ at a given indentation depth. Inset: Schematic of the indented region where a is the contact radius, E and ν are the elastic modulus and Poisson's ratio of the indented material respectively and $E_{\rm tip}$ and $\nu_{\rm tip}$ are the elastic modulus and Poisson's ratio of the tip.

tector after it has reflected off the back of the cantilever. While other methods exist to actuate the cantilever, a piezo stack is typically used to drive the cantilever towards the surface. Here, we define the vertical displacement of the cantilever due to piezo motion as z. Use of the four-quadrant photo detector to track the deflection of the cantilever allows both the vertical and torsional deflections to be tracked independently. For a simple case where the piezo applies a linear ramp downwards, the indentation depth (δ) into a sample is the difference between piezo displacement, $\Delta z = z_1 - z_0$, and cantilever deflection, $\Delta d = d_1 - d_0$.

To convert a measured voltage output from the photodetector to the force acting on the tip (F), two calibration parameters must be known. The first is the deflection sensitivity (S), which is the measure of the nanometers of cantilever deflection per volt measured from the photo detector (also known as the inverse optical lever sensitivity). The second is the spring constant, k_c of the cantilever. The applied force of the AFM tip into surface and the indentation depth can be calculated with Eqs. 1-2 respectively.

$$F = k_c(d_1 - d_0) = k_c(S(V_1 - V_0))$$
(1)

$$\delta = (z_1 - z_0) - (d_1 - d_0) \tag{2}$$

A review of methods to fully calibrate the AFM instrument as well as the influence of calibration error on indentation measurements is provided in Section 3.1.

2.1. Quasi-static indentation

Considering the system represented in Fig. 1, a profile of deflection (d) vs z-position (z) can be produced by tracking the cantilever deflection and motion as the AFM probe moves towards the surface. Through calibration of the deflection sensitivity of the AFM and the cantilever spring constant the d-z profile can be converted to a force (F)-displacement (δ) profile providing a means for force spectroscopy. An example of a typical force-displacement $(F-\delta)$ profile is presented in Fig. 2 for a parabolic tip indenting into a non-adhesive surface. While the cantilever can move quickly on the length-scale of the experiment $(10^{-1}$ to 10^6 nm s⁻¹), the dynamics of the cantilever motion are ignored, and indentation

is considered quasi-static. While other quasi-static modes (such as contact mode) exist, force spectroscopy analysis as described above, and its derivatives forms the basis of quantitative quasi-static mechanical property measurement in AFM.

For the tip geometry schematized in Fig. 2, it is clear that the contact area, represented by the contact radius, a, between the tip and the sample increases with indentation depth, such that the force required to push the tip further into the material increases. The local slope of the F- δ profile provides the contact stiffness, $k(\delta)$, (Eq. 3) and, for a given a, the reduced modulus, E_R (Eq. 4). [51] The lack of direct measurement of the contact radius in AFM during indentation prevents extraction of the reduced modulus without prior knowledge of the tip shape.

$$\left(\frac{\partial F}{\partial \delta}\right)_a = k = 2E_R a \tag{3}$$

$$\frac{1}{E_R} = \left(\frac{1 - \nu^2}{E} + \frac{1 - \nu_{tip}^2}{E_{tip}}\right) \tag{4}$$

To describe the development of contact area as a function of applied force and indentation depth (and subsequently to extract the sample mechanical properties by fitting the full F- δ curve) requires contact mechanics models that can predict the contact radius for a variety of contact conditions and material behavior. Choosing the right contact model is key to an accurate measurement of the local modulus not just in quasi-static indentations, but dynamic indentations (Section 2.2).

2.1.1. Contact mechanics

Since the introduction of Hertzian solution of the stress and deformation fields for contact between non-adhesive elastic bodies. [52] contact mechanics have continued to evolve to account for additional complexities. The Derjagun-Muller-Toporov (DMT model), developed [53] in 1975 and the Johnson-Kendall-Roberts (JKR) model, introduced [54] in 1971 extended the description of the contact between two spheres to include adhesive interactions with competing interpretations of contact behavior. [13] The conflict between the DMT and JKR models of adhesive, elastic contact was resolved by the work of Maugis and Dugdale, who demonstrated that they are in fact two regimes on either end of a continuum of possible adhesion behavior. [55] Elastic contact mechanics models commonly used with AFM to extract a modulus by fitting the F- δ profile are provided in Table 2 below. While the Oliver-Pharr [56] contact model is widely used in nanoindentation studies, typical nanoscale AFM indentations use tips without a well-known area function and the residual indent, if any, is too small to quantify so Oliver-Pharr contact mechanics is not typically used in AFM studies.

While the original Hertzian equations were developed for spheres in contact, the work of Sneddon [58] has shown that for all smooth, axisymmetric punches the applied force, F relates to the indentation depth, δ as given in Eq. 5.

$$F = \alpha \delta^n \tag{5}$$

Where n=1 for a flat punch, n=1.5 for paraboloids and spheres, and n=2 for cones. α is a constant that is dependent on the material properties and geometry of the tip and sample. The Sneddon relationship between force and displacement depth is given in Table 2 for three typical tip geometries: parabolic, flat, cylindrical punch, and conical. However, due to manufacturing defects or tip wear, AFM tips may not be ideal representations of any of these three geometries. In these cases, the exponent, n can be kept as a free parameter when fitting AFM-force displacement curves to improve the fit of force-displacement curves for non-ideal tip geometries and the accuracy of the extracted modulus. However, using n as a fitting parameter assumes that the non-ideal

Table 2Summary of the equations used to fit AFM force-indentation data for non-adhesive and adhesive elastic bodies. All equations are given assuming that one of the indented bodies is an elastic half-space.

Contact Mechanics	Tip Geometry	Descriptive Equations
Hertz [57]	Sphere ^a	$F(\delta) = E_R((a^2 + R^2) \ln(\frac{R+a}{R-a}) - 2aR),$ $\delta = \frac{a}{2} \ln \frac{R+a}{R-a}$
Sneddon [58]	Parabolic Flat Punch Cone	$F(\delta) = \frac{4}{3} E_R \sqrt{R} \delta^{\frac{3}{2}}, \ a = \sqrt{R} \delta$ $F(\delta) = 2 E_R R \delta, \ a = R$ $F(\delta) = \frac{2 \tan \theta}{\pi} E_R \delta^2, \ a = \frac{\tan \theta}{\pi} \delta$
DMT [53]	Parabolic ^a	$F(\delta) = \frac{4}{3} E_R \sqrt{R} \delta^{\frac{3}{2}} - F_{ad},$ $a = \sqrt[3]{\frac{R}{E_c}} (F + F_{ad})$ $F_{adh} = F_{adh}^{\text{ext}} = F_{adh}^{\text{ret}} = 2\pi wR$
JKR [54]	Parabolic ^a	$a = \left(\frac{R}{E_R}(F(\delta) + 2F_{adh} + \sqrt{4F(\delta)F_{adh} + 4F_{adh}^2})\right)^{\frac{1}{3}}$ $\delta = \frac{a^2}{R} - \sqrt{\frac{4F_{adh}a}{E_RR}},$ $F_{adh} = F_{adh} = \frac{3\pi \nu R}{2}$

^a The parabaloid Hertz equations are also valid for spherical tips for small indentations

experimental F- δ behavior is due to non-ideal tip geometry and not plasticity, viscoelasticity, or some other phenomenon.

Each of the contact mechanics models listed in Table 2 allows for an extraction of the elastic modulus from the indentation data, but accurate measurement also requires a judicious choice of the contact model that best represents the contact conditions between the tip and the sample surface as well as the deformation behavior of the material. An adhesion map developed by Johnson and Greenwood [13] (Fig. 3(b)) can be used to choose the appropriate elastic contact model for a given experiment based on the work of adhesion (w) and the Tabor (μ) or elasticity parameter (λ) as calculated by Eq 6..

$$\lambda = 1.16\mu = \frac{2.06}{D_0} 3\sqrt{\frac{Rw^2}{\pi E_R^2}} \tag{6}$$

where D_0 is the interatomic interaction distance. D_0 is typically taken to be between 1-5 nm; one study measured the interaction distance between polystyrene (PS) and silicon to be 1.5 to 2.5 nm. [59] With a known R, the F_{adh}^{ret} at pull-off (Fig. 3(a)) can be used to calculate w as shown in Table 2. For a given force curve, the ratio of the maximum indentation force F_{max} to F_{adh}^{ret} along with the calculated λ can be used to find the adhesive contact regime and appropriate contact model to use from the Johnson-Greenwood map in Fig. 3(b). Fig. 3(c-h) shows schematically the deflection of the cantilever and the tip-sample contact during the complete force-displacement curve shown in Fig. 3(a). The difference in sample adhesion for JKR and DMT cases results in different tip-surface contact conditions as illustrated. The schematics are ordered by stages, starting with approach (I), snap-on (II), extension (III), retraction (IV), pull-off (V) and departure (VI). The choice of appropriate contact model for the fitting of collected forces can be automated to some extent by software that extracts $F_{\rm adh}$ and F_{max} in conjunction with a known tip shape and estimated sample modulus to find the appropriate contact mechanics regime from Fig. 3(b). Sample viscoelasticity and other phenomena may violate assumptions such that none of the contact mechanics models perfectly describe the force curve, causing automated processes to break down. Often, manual intervention is required to determine which contact mechanics model is the best approximation to the collected data.

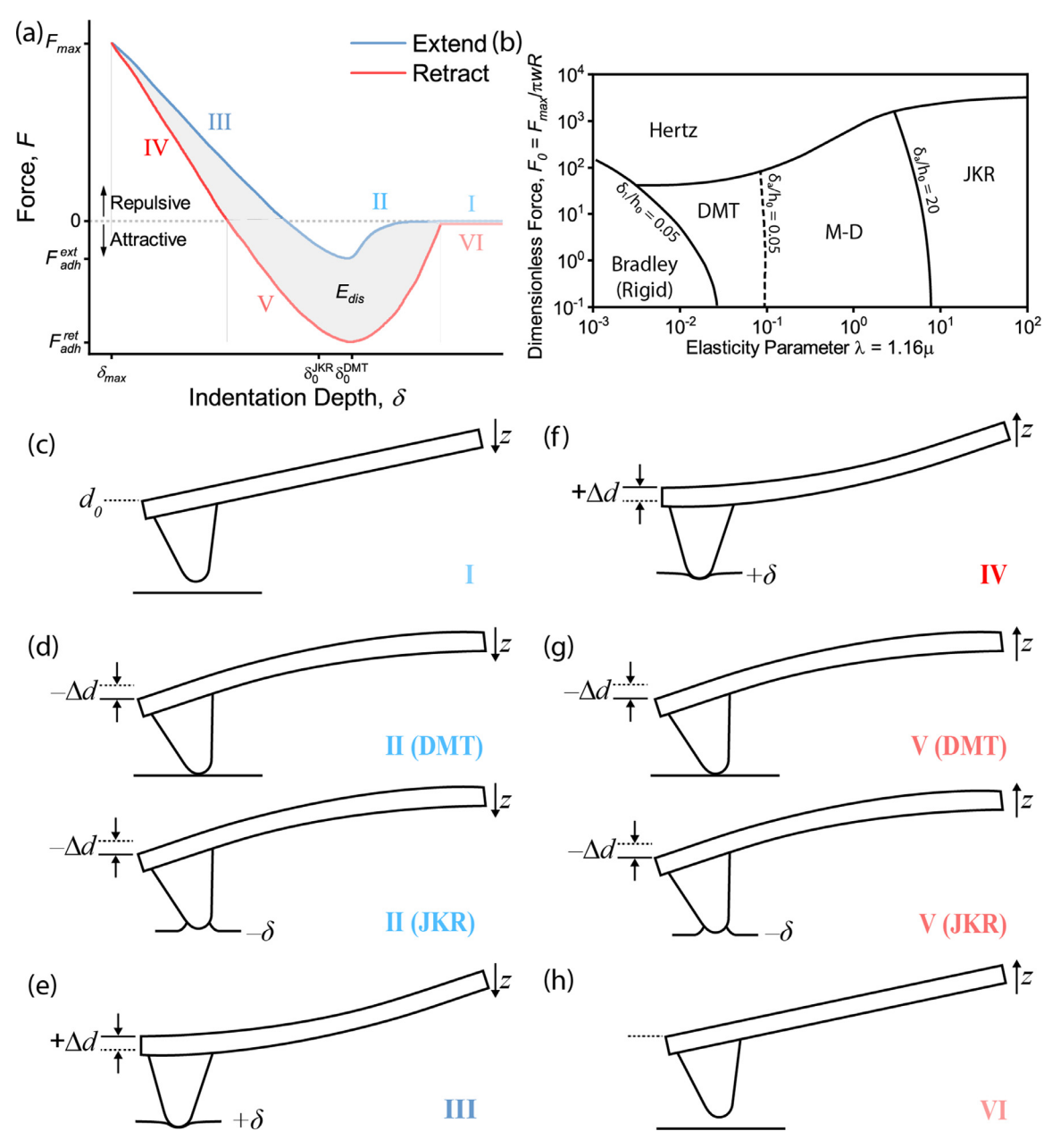


Fig. 3. (a) Schematic of a typical force curve on an adhesive, viscoelastic material. Within a single extend-retract cycle there are multiple regimes which are indicated with roman numerals I-VI. Key F- δ points are also indicated. (b) Map of adhesive contact regimes as established by Johnson and Greenwood. [13], Copyright 1997. Adapted from with permission from Elsevier Science Ltd. [13]. (c-h) Schematics of the AFM cantilever in each of the regimes (I-VI) indicated in (a). During (c) Stage I, the tip approaches the samples (+z) and has not interacted with the sample. (d) Stage II is in the 'attractive regime' where the tip is pulled towards the sample (-d) and the tip snaps onto the surface as it moves closer. In the DMT regime, the 'snap-on' of the tip onto the surface is a result of long range adhesion forces that are relatively weak compared to the material modulus and the DMT 'snap-on' is not associated with any surface deformation. In the JKR regime, the surface is pulled towards the tip (- δ) due to strong, short range adhesive forces. The surface deformation alters the point of zero indentation depth (a). Stage III occurs when the tip is pushed further into the sample (+ δ) and the deflection of the cantilever is positive (+d), when the sample surface is applying a net repulsive force to the tip resisting the tip motion.(f) At Stage IV the tip has reached the maximum indentation depth and the tip has begun to retract (-z) but the restoring force due to the material elasticity is still stronger than the adhesive force and a net repulsive force is applied to the tip. Eventually the indentation cycle reaches stage V (g) and the surface is no longer applying a net repulsive force (-d) but the adhesive forces maintain tip-sample contact until the pull-off force (F_{ad}) required to overcome the adhesion is reached. (h) Once the adhesive forces are overcome, the tip is freed from the sample (Stage VI) and continues to move away from the surface (-z). The schematics of the tip in Stage II (d) and V

2.1.2. Extensions for viscoelasticity

AFM measurements of viscoelasticity and polymer relaxation near the glass transition temperature (T_g) are a difficult topic to study and significant debate continues in the field as to the best approach for viscoelastic interpretation of AFM indentations. [10,25,35,50,60-65] While continuum approaches brought over from bulk scale testing have been widely applied and useful for estimations of viscoelasticity during indentation, the com-

plexity of the viscoelastic model is limited by the number of spring and dashpot elements used and assumptions made about the contact area and surface deformation. [66] Despite the limitations to viscoelastic modelling of the AFM indentation, numerous studies have used various viscoelastic interpretations of F- δ curves for capturing the surface viscoelasticity of polymers and other soft materials, some of which are highlighted below.

The simplest option to describe the viscoelastic behavior in materials characterized by AFM are spring-damper models that represent the material behavior as group of springs and dashpots attached in parallel and/or series. These methods provide relationships between the force and displacement that account for the time dependence of the sample modulus. Applying the correspondence principle to Hertz indentation theory [67] yields Eq. 7 for a three element viscoelastic solid and a constant loading rate, $U = F_{\rm max}/t_{\rm max}$.

$$\delta^{3/2}(t) = \frac{3UT}{4\sqrt{R}} \frac{1 - v^2}{E_{\infty}} \frac{t}{\tau} - \left(1 - \frac{E_{\infty}}{E_0}\right) \left(1 - e^{-t/\tau}\right) \tag{7}$$

Where E_{∞} and E_0 are the long- and short-time moduli respectively and τ is the characteristic relaxation time. The viscoelastic model of Eq. 7 was applied experimentally by Chyasnavichyus et al.,[10] to describe their 'loading rate spectroscopy' AFM data. Time constants extracted from the fitting Eq. 7 to the indentations can then be used along with the modulus values to estimate the storage and loss modulus of the material. Central to the application of Eq. 7 is the assumption of a constant loading rate during indentation.

Efremov *et al.* [14,50] applied a viscoelastic model for Hertzian indentation Eq. 8-(9) developed by Ting [68] to the approach and retract curve of AFM indentations on cellular and other biological samples at low (<10 Hz) and high (2 kHz) indentation rates in fluid and found excellent agreement between Ting's model and the experimental data when modelling the time dependent modulus either with a three element solid model or power law rheological behavior.

$$F(t,\delta(t)) = \frac{4\sqrt{R}}{3(1-\nu^2)} \int_0^t E(t-\xi) \frac{\partial \delta^{1.5}}{\partial \xi} d\xi, 0 \le t \le t_m F(t,\delta(t)) = \frac{4\sqrt{R}}{3(1-\nu^2)} \int_0^{t_1(t)} E(t-\xi) \frac{\partial \delta^{1.5}}{\partial \xi} d\xi, t_m \le t \le t_{ind}.$$
 (8)

$$\int_{t_1(t)}^{t} E(t - \xi) \frac{\partial \delta}{\partial \xi} d\xi = 0$$
 (9)

Here, $F(t, \delta(t))$ is the time dependent indentation force, ξ is a dummy variable for integration, $t_{\rm m}$ is the time until the maximum indentation point and $t_{\rm ind}$ is the total time for an indentation. The viscoelastic properties of the indented material can be calculated by evaluating Eqs. 8-9 for the displacement history during a given indentation by optimizing the fitting parameters of a chosen relaxation function to fit the experimental data.

Extending viscoelastic contact mechanics to include JKR adhesion is much more complicated due to the rate dependence of the work of adhesion and the hysteresis in adhesion for viscoelastic materials where the energy required for separating the tip and sample is greater than bringing them together. [67] The viscoelastic form of the JKR contact model is as shown in Eq. 10 for a known loading history. [69]

$$a^{3}(t) = \frac{3R}{4} \left[\frac{3R\pi \left(C_{0}K_{I}(t) \right)^{2}}{2} + C(t) * F(t) \right] + C_{0}K_{I}(t) \sqrt{\left(\frac{3\pi R}{2} C_{0}K_{I}(t) \right)^{2} + 3\pi R(C(t) * F(t))} \right]$$
(10)

Where C(t), C_0 , and K_1 are the creep compliance, instantaneous compliance, and the stress intensity factor at the crack tip by considering the adhering and peeling between tip and sample as a crack healing and growth. C^*F is a convolution where $C * F = \int_{0^-}^t C(t-\xi) \frac{\partial F}{\partial \xi} d\xi$. Accurately describing JKR contact with viscoelasticity requires additional rate-dependent parametrization of tipsample cohesion, making viscoelastic JKR unwieldy for application to AFM, where contact conditions are not particularly well-known. Assuming rate-independent adhesion parameters $(K_{\rm I}(t) = K_{\rm C})$ allows for a more readily applicable viscoelastic JKR model for an

elastic tip contacting a viscoelastic half-space. [69] While not physically reasonable for the unloading portion of indentation curves on polymers with rate-dependent behavior, there is some experimental evidence on elastomers [70,71] that the energy release rate does not vary significantly during the loading portion of an indentation curve, making $K_{\rm I}(t) = K_{\rm C}$ a reasonable approximation for the approach portion of an AFM indentation.

Alternatively, Attard's approach [60,72-74] discretizes the surface into axisymmetric nodes and numerically solves a set of equations to calculate the deformation and pressure at each node. From the calculated pressure and deformation, the force-displacement curve for the approach and retract portion of the curve can be reconstructed to fit indentations onto adhesive, viscoelastic materials. The greatest benefit of Attard's approach is the flexibility in choice of models to described adhesive forces and viscoelastic behavior. Recent tools for the simulation of AFM indentation has incorporated Attard's model to approximate AFM tip-sample interactions. [75] An extension of Attard's approach has been recently developed to include transverse elements for modelling in-plane surface interactions. [66]

2.1.3. Extensions for hyperelasticity

Lin *et al.* have extended the Hertzian contact model to use Mooney-Rivlin hyperelasticity to fit indentation curves on hyperelastic materials Eqs. 11-(12) by estimating the average strain underneath an AFM tip. [76] The use of a Mooney-Rivlin model as opposed to elastic models improves fitting on large indentations in hyperelastic materials.

$$F = \pi R^{1/2} B_1 \left(\frac{\delta^{5/2} - 3\sqrt{R}\delta^2 + 3R\delta^{3/2}}{\delta - 2\sqrt{R}\delta^{1/2} + R} \right) + \pi R^{1/2} B_2 \left(\frac{\sqrt{R}\delta^{5/2} - 3R\delta^2 + 3R^{3/2}\delta^{3/2}}{-\delta^{3/2} + 3\sqrt{R}\delta - 3R\sqrt{\delta} + R^{3/2}} \right).$$
(11)

At infinitesimal strains, Hertzian mechanics applies, and Eq. 11 is reduced to Eq. 12

$$B_1 + B_2 = \frac{4E_0}{9\pi (1 - \nu^2)} \tag{12}$$

Where E_0 is the initial Young's modulus of the hyperelastic material. B_1 and B_2 are material constants. For Eqs. 11 and 12, setting $B_2 = 0$ yields the neo-Hookian version of the hyperelastic contact model. Additional equations covering hyperelastic force-displacement behavior for a variety of strain energy potential functions have been summarized in ref. [77].

2.1.4. Scanning quasi-static modes

Force volume (FV) and pulsed force mode (PFM) are similar modes that allow for extraction of quasi-static force curves as shown in Fig. 3 from the applied z-piezo displacement and the measured cantilever deflection while scanning across a sample by oscillating the cantilever well below resonant frequencies (and thus differentiating these modes from dynamic AFM modes in Section 2.2 that oscillate near or at the resonant frequency). FV uses a linear ramp profile at low frequencies (<70Hz) and was the first scanning quasi-static mode developed [78] to directly extract contact stiffness and modulus over an $n \times n$ array of locations on a sample by ramping the z-piezo at a constant rate until a set maximum deflection threshold is reached. The inertial effects associated with the transition from extension to retraction of the cantilever during (Fig. 3e-f) FV's linear ramp limits quantitative accuracy at fast scanning rates above 10 Hz without corrections for the inertia. [11,15] PFM was developed to address this limitation, using a sinusoidal ramp and active peak force control to reduce the cantilever acceleration at maximum extension enabling higher drive frequencies (theoretically up to 20-50 kHz depending on the cantilever).

[16,79] PFM has seen significant development since its introduction in the 1990s, and is now referred to in the literature with a variety of terms and is incorporated into a number of commercial AFMs under a variety of trademarks.

As the entire F- δ curve is measured for both of FV and PFM, the contact models described in Table 2 as well as the viscoelastic and hyperelastic extensions can be used to extract modulus, adhesion energy, and relaxation times from the acquired data in both FV and PFM. While fitting algorithms for elastic contact mechanics models are generally included in most commercial and open source AFM software, more advanced analysis (*e.g.* incorporation of viscoelasticity) generally requires external fitting software.

For PFM, the rapid scan rate allows for arrays of force curves to be collected rapidly over a large area, providing high resolution maps of modulus, adhesion and dissipation that was not previously achievable with FV AFM. Algorithms for the fast, automated fitting of the acquired curves have been continually developed for real time property measurement with PFM while scanning. [76, 80-82] While the use of a piezo limits the maximum *z* rate that can be used in conjunction with PFM methods, some direct drive methods have been developed which can further increase the driving frequency by up to two orders of magnitude. [83] and broaden the dynamic range of a single cantilever. [84]

A benefit of not driving the cantilever on resonance as required by dynamic modes is that a wide range of indentation rates can be achieved with a single cantilever. This rate flexibility is particularly useful for studying viscoelastic properties, as discussed further in Section 2.3 and 3.2.4. Currently, PFM methods are typically used for construction of high-resolution property maps, but the sinusoidal ramp can complicate analysis on viscoelastic materials due to the varying indentation rate. FV is more appropriate for control of the indentation rate on viscoelastic material, or the specification of desired ramp profiles that may include a dwell time, secondary oscillations, or an external sample perturbation.

2.2. Dynamic indentation

AFM can also be operated by driving the cantilever at or near its fundamental resonant frequency or one of its higher eigenmodes. By driving the cantilever at or near resonance a high oscillation amplitude can be achieved with relatively little drive input. To perform dynamic AFM, a driving force excites a cantilever and then traces a sample surface while measuring the changes induced in the oscillation. The change in behavior between a freely oscillating cantilever and the same cantilever interacting with a surface during oscillation allow the surface properties to be probed by characterizing the perturbations to tip motion. A number of textbooks and reviews [5,20,85-88] discuss the physics of dynamic AFM in detail. Here we provide a brief overview so that mechanical property measurements with dynamic modes can be understood. Compared to quasi-static methods, dynamic AFM, particularly multifrequency methods, promises advantages in sensitivity to material properties as well improvements in the spatial and time resolution of measurement. [3]

2.2.1. Free cantilever oscillation

When a cantilever is far from the influence of the sample surface, the tip-sample force ($F_{\rm ts}$) is zero, and the cantilever can be modelled as a damped, forced harmonic oscillator (Eq. 13). In Eq. 13, m is the mass of the cantilever, f_1 is the resonant frequency, Q is the quality factor and $F_d(t)$ is the driving force acting on the cantilever over time, t. In the simplest case, $F_d(t)$ is a harmonic signal (Eq. 14) that oscillates the cantilever at the resonant frequency of the cantilever, f_1 and amplitude F_0 . The resulting cantilever deflection, d(t) can be described by Eq. 15. Here d_0 is the mean cantilever deflection, A is the tip oscillation amplitude, and φ is the

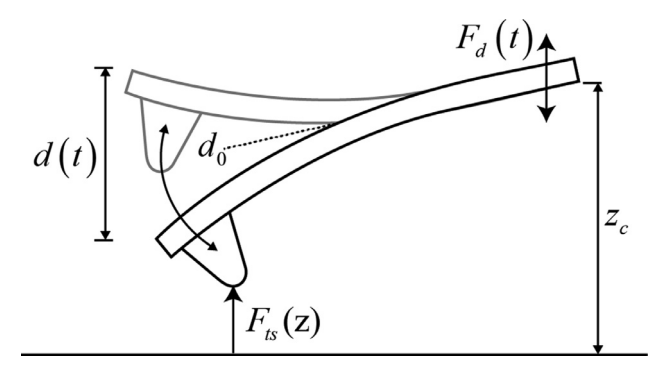


Fig. 4. Schematic representation of dynamic cantilever motion near the sample surface

phase lag between drive input $F_{\rm d}(t)$ and the output cantilever deflection d(t). For a freely oscillating cantilever, $\varphi=90^{\circ}$. The cantilever motion is schematized in Fig. 4.

$$m\ddot{d} + k_c d + \frac{2\pi m f_1}{O} \dot{d} = F_{ts}(z) + F_d(t)$$
 (13)

$$F_d(t) = F_0 \cos(2\pi f_1 t) \tag{14}$$

$$d(t) = d_0 + A\cos(2\pi f_1 t - \varphi) \tag{15}$$

As a mechanical system, the AFM cantilever has high order eigenmodes in addition to the fundamental resonance of the cantilever. Relative to the fundamental (n=1) eigenmode, the high order eigenmodes modify the effective cantilever resonant frequency, cantilever stiffness, quality factor and deflection sensitivity during oscillation. The scaling in cantilever properties (Eq. 16) can be estimated by solving for the roots (λ_n) of the characteristic equation of a rectangular cantilever $(1 + \cos(\lambda_n) \cosh(\lambda_n) = 0)$, where $\lambda_n = 1.875, 4.694, 7.855, 10.996$ for $n = 1 \rightarrow 4$.

$$f_n = \left(\frac{\lambda_n}{\lambda_1}\right)^2 f_1, k_n = \left(\frac{f_n}{f_1}\right)^2 k_1, Q_n = \frac{f_n}{f_1} Q_1$$
 (16)

Oscillating the AFM cantilever at higher order eigenmodes has been demonstrated as beneficial for improved sensitivity and property contrast while imaging in certain conditions compared to oscillation at the fundamental eigenmode of the same cantilever. [89-92] AFM modes utilizing high order eigenmodes will be discussed further in Sections 2.2.3-4.

2.2.2. Oscillation near a sample surface

As the oscillating cantilever approaches a sample surface, the tip motion is perturbed as a function of distance from the surface and analysis of these perturbations with respect to the free cantilever response allow characterization of the surface forces $(F_{ts}(z))$ acting on the tip. [93] Near a polymer surface, we can expect $F_{ts}(z)$ to have a profile qualitatively similar to the approach curve given in Fig. 3(a) that includes surface forces and deformation. In dynamic AFM, the amplitude, resonant frequency, and phase lag of the cantilever motion changes (Fig. 5) with decreasing z in response to the change in the relative magnitude and direction of forces acting on the tip. Both attractive and repulsive forces act on the AFM tip simultaneously, [20] and separating the influence of the various surface forces relevant in dynamic AFM has remained challenging. Reconstruction of the forces acting on the tip as a function of z requires either solution of the inverse problem of calculating the amplitude and phase lag as the tip approaches the surface, or direct measurement of the time resolved interaction force. [94-98]

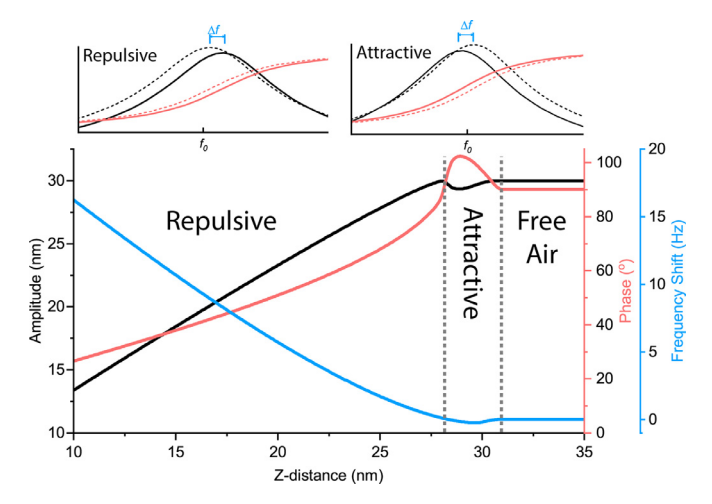


Fig. 5. A representative amplitude modulated approach curve (AMAC) with the free-air (F), attractive (A) and repulsive (R) regimes indicated for an adhesive sample. The amplitude and phase profiles as a function of z-distance is indicated as black and red, respectively. An additional profile showing the frequency shift as a function of z-distance for a frequency modulated (using a phase-locked loop) approach curve with equivalent cantilever and sample properties is also given in blue. Harmonic approximations indicating the shift in the amplitude (black) and phase (red) of the cantilever motion near resonance in the attractive and repulsive regime. All profiles are generated using the online VEDA software [102]. The sample is modelled as an adhesive, viscoelastic material similar to the material described in Fig. 3(a).

Previous work has established that dynamic AFM can operate either in net attractive or repulsive interaction regimes on approach to the sample surface dependent on whether the average force acting on the tip during an oscillation cycle is pulling the tip towards the surface or pushing it away. [99,100] As demonstrated by the simulated amplitude modulated approach curve (AMAC) in Fig. 5, when the tip begins to interact with the surface, the oscillation is initially attractive as adhesive forces are dominant and the oscillation amplitude and resonant frequency of the cantilever decrease while the phase lag increases (associated with regime II in Fig. 5). Once the tip is brought closer, the phase lag decreases as repulsive forces strengthen. Further reduction in z leads to operation in the repulsive regime with $\Phi_I < 90^\circ$ and an increase in resonant frequency with a further reduction in oscillation amplitude as repulsive forces due to material deformation are dominant.

The cantilever motion while interacting with the surface can be described by measuring the changes between the input and output oscillation amplitude (A), shift in resonant frequency (Δf) of the cantilever, as well as the phase lag (φ) between the input drive signal and measured cantilever deflection output signal. The highly non-linear character of the surface forces acting on an AFM tip as it approaches the sample prevent harmonic models being used to describe the cantilever dynamics and extraction of the instantaneous contact stiffness unless the cantilever is oscillating at very small amplitudes as demonstrated by Hölscher $et\ al.\ [101]$.

The impact of the surface on the cantilever dynamics can be better interpreted by considering the energy transfer between the tip and the sample. When the cantilever moves closer to the surface (decrease in z), the time averaged force ($\langle F_{ts} \rangle$), virial ($\langle F_{ts} \cdot z \rangle$) and energy dissipated by the cantilever in the surface (E_{dis}) develops as the relative contributions from the attractive and repulsive forces change with z. If the cantilever is operating on resonance, E_{dis} can be calculated from A and φ (Eq. 17). [103]

$$E_{dis} = \frac{\pi kA}{O} (A_0 \sin \varphi - A) \tag{17}$$

The change in phase lag can also be related to the virial, $<F_{ts}\cdot z>$ while operating at its resonant frequency by (Eq. 18)

$$\langle F_{ts} \cdot z \rangle = -\frac{kA_0}{2Q} A \cos \varphi \tag{18}$$

Additionally the average force acting on the tip during an oscillation cycle, $\langle F_{ts} \rangle$ increases as z decreases as described by Eq. 19 for a cantilever oscillating on resonance. [103]

$$\langle F_{ts} \rangle \approx \frac{kA_0}{2Q} \left(1 - \left(\frac{A}{A_0} \right)^2 \right)^{\frac{1}{2}}$$
 (19)

Measurements of the virial and dissipated energy can quantify the strength of conservative and dissipative forces acting on the tip. Detailed analysis of the changes in dissipated energy with *A* can identify the source of dissipation in the tip-sample interaction. [104] Sample elasticity and Van der Waals forces are both examples of conservative tip-sample interactions whereas sample viscosity and capillary effects are examples of dissipative tip-sample interactions. In addition to the average force measurement provided in Eq. 17, Knoll *et al.* provides a means to estimate the indentation depth in dynamic AFM modes through comparison of acquired AMAC curves on the soft material of interest with curves acquired on an infinitely stiff material with the same cantilever. [105]

The properties which can be extracted from a sample surface depends on both (a) the choice of oscillation properties to use for feedback while scanning and (b) whether or not the cantilever is simply sinusoidally driven (Eq. 14), that is, whether the driving frequency or amplitude is actively adjusted in response to changes in the interaction forces on the tip. There are two principal, single-frequency, dynamic operation modes:

- amplitude modulated (AM) AFM
- · frequency modulated (FM) AFM

In AM AFM, the amplitude of the tip oscillation (A_1) is kept at a constant setpoint smaller than the free air amplitude $(A_{1,0})$ by adjusting the height of the cantilever (z). The changes in z required to maintain a constant oscillation amplitude provides a profile of the AFM surface topography. If the tip touches the surface during oscillation, then the oscillation is classified as intermittent contact or tapping mode, otherwise if the tip is perturbed by attractive surface forces only, then the oscillation is classified as non-contact.

Material contrast can be observed during AM AFM scanning using a well-known technique called phase imaging [93] where changes in the phase lag during scanning across a sample provides information about transfer of energy between the tip and the surface. While changes in the phase lag (Eq. 20) have both elastic and inelastic contributions, [88] during AM AFM the amplitude is used for feedback control to adjust z position and maintained at a constant setpoint (A_1) . Therefore the first term, corresponding to elastic forces in Eq. 20 is constant during AM AFM scanning. As a result, only the dissipative, inelastic term in Eq. 20 will alter the measured phase lag during scanning in AM AFM. [106] The dissipated energy can be useful for mapping of soft materials as changes in material viscoelasticity, adhesion and hydrophobicity will result in contrast between components in the phase channel of collected data. Measurements of the dissipated energy on a SEBS triblock copolymer found that the dissipated energy measured via AM AFM and quasi-static modes are comparable. [63]

$$\sin \phi = \frac{\omega}{\omega_0} \frac{A_1(\omega)}{A_{0,1}} + \frac{QE_{dis}}{\pi k_c A_{0,1} A_1(\omega)}$$
 (20)

Alternatively, FM (frequency modulated) AFM scanning maintains a constant frequency shift between the resonant frequency

of the cantilever far away from the surface and the resonant frequency of the cantilever close to the surface while recording the oscillation amplitude and tip sample separation. As a result, $F_{\rm d}(t)$ is no longer a simple sinusoid, but rather $F_{\rm d}(t)$ is constantly adjusted to keep the cantilever oscillating on resonance at constant amplitude. The shift in resonant frequency (Eq. 21) and driving amplitude is dependent on the average forces active on the AFM tip and as such provides direct information on the average force acting on the tip during an oscillation. [101]

$$\Delta f = -f_0 \frac{\langle F_{ts} d \rangle}{k_c A^2} \tag{21}$$

A harmonic approximation of the cantilever dynamics by Schröter et al. [107] allows for the extraction of effective tip-sample contact stiffness (k_{ts}) and damping coefficient (α_{eff}) over an oscillation cycle as a function of z-position from the A and φ of the cantilever oscillation. The model of Schröter et al. differs from previous harmonic approximations of the cantilever oscillation near the sample surface due to calculating the measured $k_{\rm ts}$ over the entire oscillation cycle rather than attempting to determine the instantaneous force gradient. To calculate k_{ts} (Eq. 22) and α_{eff} (Eq. 23), the resonance peak must be fit with the equations for a driven harmonic oscillator to determine resonant frequency, ω , the amplitude of the external driving force F_d , the vibrating mass, m as well as the cantilever spring constant, k_c and the quality factor, O. For the approximation of the cantilever as a harmonic oscillator several conditions need to be met. Namely the cantilever must have a high quality factor (Q > 200) so that harmonics induced during cantilever oscillation are suppressed and that the induced harmonic frequencies do not coincide with the higher order eigenmodes of the cantilever. Additionally, the cantilever oscillation must maintain a sinusoidal waveform while interacting with the surface. These conditions can be quite easily met by a range of commercial cantilevers operating in air. However, as these are averaged values over an entire oscillation, both attractive and repulsive contributions are included in the averaged value, preventing Schröter's harmonic approximation from being used to extract local modulus and viscosity.

$$k_{ts} = k_{eff} - k_c = m\left(\omega^2 + \cos\varphi \frac{F_d/m}{A}\right) - k_c$$
 (22)

$$\frac{\alpha_{eff}}{m} = \frac{-\sin\varphi}{\omega} \frac{F_d/m}{A} \tag{23}$$

2.2.3. Dual frequency intermittent contact modes

While initially multi-frequency AFM was conducted by exciting the fundamental and passively measuring induced higher harmonic cantilever oscillations due to tip-sample forces, recent advancements in multi-frequency AFM have been achieved by simultaneously exciting a cantilever at two of its eigenfrequencies (f_n), typically the fundamental and another, high-order eigenfrequency Eqs. 24-(25) to acquire highly sensitive measurements of variations in surface forces. [92,108] Flexural and torsional modes can also be excited simultaneously to obtain properties in-plane and perpendicular to the surface, [109] but more attention has been paid to the simultaneous excitation of two flexural modes. The first mode can either operate in AM or FM mode for surface tracking, while the higher order mode can either be passively driven or also controlled through AM, FM or phase modulation (PM). [28]

$$F_d(t) = \sum_n k_n A_i \cos(2\pi f_n t)$$
 (24)

$$d(t) = d_0 + \sum_{n} A_n \cos(2\pi f_n t - \phi_n)$$
 (25)

The use of multiple oscillation modes improves the sensitivity of the high order mode to the force gradient [110] and there-

fore changes in material properties. The use of higher order eigenmodes can also complicate interpretation of phase data. Kiracofe *et al.* have established that there are three interaction regimes in dual frequency AFM, [111] with the relative kinetic energies of the two excited modes determining the regime. In the limit where $A_2 << A_1$, equations to extract mechanical properties from the measured deflection signal have been developed for several bimodal operation modes and subsequently applied for the mechanical property mapping of soft materials. [26,28,46,112] Of these, AM-FM has been the most widely adopted as it provides stable operation, relatively simple data analysis and high sensitivity. [28]

In AM-FM AFM, the first eigenmode is amplitude modulated for surface tracking, and the second eigenmode is frequency modulated to detect shifts in the resonant frequency (Δf_i) of the higher mode due to changes in sample stiffness and dissipation. A block diagram describing the inputs and outputs utilized in AM-FM AFM is given in Fig. 6. The first mode is driven at a large free-air amplitude ($A_{0,i}$) with a setpoint low enough (A_I) to enforce repulsive interactions with the sample surface ($\varphi_i < 90^\circ$). The second eigenmode is driven at a relatively low free air amplitude $A_{0,i}$, typically less than 10% the amplitude of first eigenmode to prevent excessive cross-talk. [28,113]

Two theoretical approaches for the analytical calculation of modulus have been developed for AM-FM. In both, assumption of Hertzian contact mechanics allows for the extraction of modulus from the measured variables by comparing the data acquired simultaneously from the two excited resonances. [110] The resulting equations from Garcia *et al.* to calculate the sample deformation and reduced modulus for a paraboloid tip is given in Eqs. 26-27,[19] which have been further generalized using Sneddon contact mechanics for a range of tip shapes. [46]

$$\delta = \frac{1}{2Q_1} \left(\frac{k_1}{k_2} \right) \left(\frac{f_2}{\Delta f_2} \right) \left(A_{0,1}^2 - A_1^2 \right)^{1/2} \tag{26}$$

$$E_R = \frac{4\sqrt{2}}{\sqrt{R}} Q_1 k_1 \left(\frac{k_2 \Delta f_2}{k_1 f_{0,2}}\right)^2 \frac{A_1^{3/2}}{A_{0,1}^2 - A_1^2}$$
 (27)

Here k_i , $f_{0,i}$, A_i , $A_{0,i}$ and Q_i , are the spring constant, resonant frequency, amplitude, free air amplitude and quality factor of the ith mode respectively. During a scan, each of these variables are held or controlled to set values, Δf_2 is the sole observed property that varies as a surface is scanned. E_R is the reduced modulus and δ is the sample deformation. Sample topography (h) as measured by AM-FM includes contributions from the sample deformation (δ) during indentation. The sample topography can be corrected by subtracting the $\delta(x,y)$ map from the h(x,y) map.

FM-FM AFM swaps the amplitude modulation of the fundamental resonance with frequency modulation. The local elastic modulus and deformation can be calculated by considering the measured frequency shifts of the first and second resonance as shown in Eqs. 28-29. [112] FM-FM has not seen the same widespread application as AM-FM due to limitations in the robustness of surface tracking.

$$E_{eff} = \sqrt{\frac{9}{RA_1}} \frac{k_2^2}{k_1} \frac{f_{0,1}}{f_{0,2}^2} \frac{\Delta f_2^2}{\Delta f_1}$$
 (28)

$$\delta = A_1 \frac{k_1 f_{0,2}}{k_2 f_{0,1}} \frac{\Delta f_1}{\Delta f_2} \tag{29}$$

An alternative method to calculate surface properties from AM-FM observables has been developed by Labuda *et al.* [28] and relies on the calculation of the virial of the first eigenmode, which is assumed to behave as a simple harmonic oscillator. The approach of Labuda *et al.* has been recently extended to incorporate the Kelvin-Voigt element describing the viscoelasticity of the sample surface. [25]

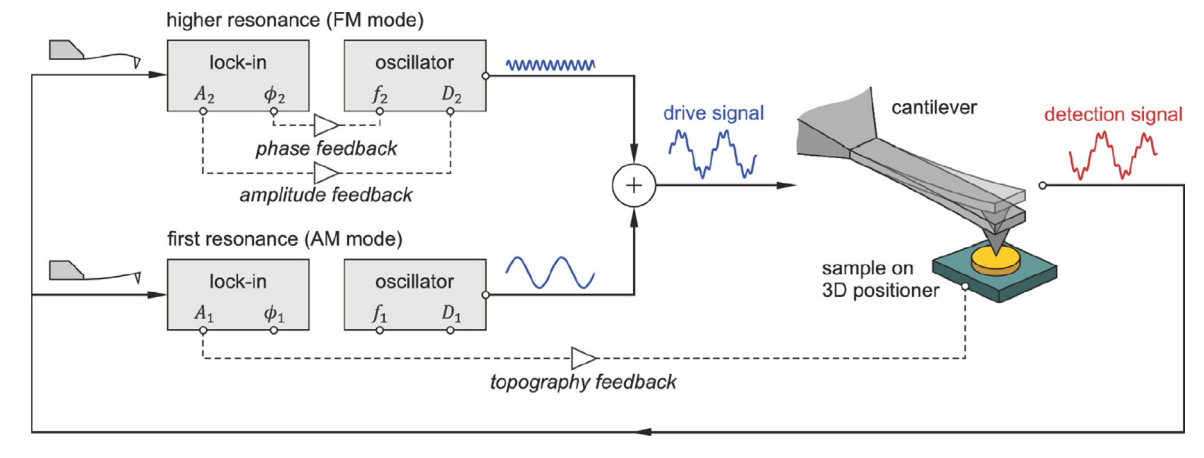


Fig. 6. Block chart describing control and feedback during AM-FM scanning. [27], Copyright 2017. Reproduced with permission from the American Chemical Society.

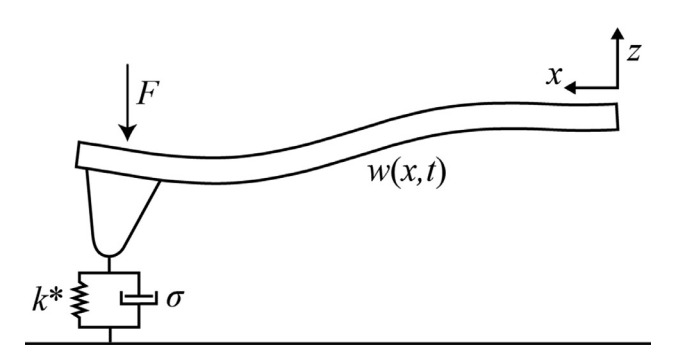


Fig. 7. Schematized representation of contact resonance AFM measurement for the mechanical model detailed in ref. 73

2.2.4. Contact resonance

The previous section on dynamics have focused on intermittent contact modes, where the tip is not in contact with the sample surface for the entire oscillation. Additional dynamic modes, commonly collected under the term 'contact resonance' (CR) AFM, [5] is conducted by holding the cantilever tip on the surface at a constant force setpoint while the sample is excited and measuring the amplitude and phase of the cantilever response across a range of frequencies to build the contact resonance spectra of the AFM cantilever (Fig. 7). While initial CR techniques used ultrasonic frequencies above the resonances of the AFM cantilever, [114,115] more modern techniques utilize the enhanced sensitivity by using excitation frequencies near the cantilever eigenfrequencies. The low oscillation amplitudes used along with the tip remaining in contact with the sample during analysis means that the tip-sample interaction is linear and therefore easier to relate to the contact stiffness compared to intermittent contact modes. From the spectra, the change in resonant amplitude and phase responses relative to the free air resonance spectrum can be used to calculate the stiffness and damping of the sample surface, but requires complex models of the beam deflection and the coupling between the AFM tip and the surface. A variety of characteristic equations have been developed to describe the modal behavior of the cantilever while coupled to the sample surface with varying degrees of complexity and a selection of models that cover a variety of situations are provided in Table 3.

To measure the contact stiffness k^* , the dynamic properties of the cantilever (c_B) oscillating on resonance in the free air $(f_n{}^0)$ must first be measured using Eqs. 30-31, where is $\lambda_n{}^0$ is root to the characteristic equation in the free air for the eigenmode, n and

L is the length of the cantilever.

$$\frac{\lambda_n^2}{f_n} = \sqrt{4\pi^2 \frac{12\rho}{b^2 E}} = c_B^2 \tag{30}$$

$$\lambda_n^0 L = c_B L \sqrt{f_n^0} \tag{31}$$

The tip is then brought into contact with the sample and held at a constant setpoint while a new resonance spectrum is acquired. The new $\lambda_n L$ is then calculated from the new resonance frequency of the coupled tip-sample system and input into a characteristic equation that describes the coupled system such as Eq. 32 and solved for the contact stiffness k^* . For purely elastic behavior, only the real component of the wave number is used and input into the characteristic equation. Here Eq. 32 is taken from ref. [29] and includes the elastic and dissipative components of the tip-sample contact while ignoring lateral forces.

$$\begin{split} &\frac{2}{3} \left(\lambda_n L_1\right)^3 \left[1 + \cos \lambda_n L_1 \cosh \lambda_n L_1\right] \\ &= \left(\alpha + i\beta \left(\lambda_n L_1\right)^2\right) \\ &\left[\left(1 + \cos \lambda_n L' \cosh \lambda_n L'\right) \left(\sinh \lambda_n L_1 \cos \lambda_n L_1 - \sin \lambda_n L_1 \cosh \lambda_n L_1\right) \\ &+ \left(1 - \cos \lambda_n L_1 \cosh k_n L_1\right) \left(\sin \lambda_n L' \cosh \lambda_n L' - \cos \lambda_n L' \sinh \lambda_n L'\right)\right] \end{split} \tag{32}$$

Where, α (Eq. 33) and β (Eq. 34) are the elastic and dissipative components of the tip-sample contact model respectively

$$\alpha = k^* L_1^3 / 3EI \tag{33}$$

$$\beta = \sigma L_1 / \sqrt{9EI\rho A} \tag{34}$$

Here, ρ , E, and I are the density, elastic modulus, and moment of inertia for the rectangular cantilever. k^* and σ are the contact stiffness and damping coefficient of the Kelvin-Voigt element representing the elastic and dissipative components of the tip-sample contact. For elastic behavior, $\sigma=0$. L_1 is the distance between the base of the cantilever and the tip and L' is the distance between the tip and the free end of the cantilever where $L_1=L$ -L'. The relative position of the tip and therefore L' and L_1 can be determined experimentally by acquiring contact resonance spectra across multiple resonance peaks and solving Eq. 32 for multiple values of L_1/L to find the value of L_1/L at which the measured contact stiffness is in agreement for multiple eigenmodes. The reduced modulus is then calculated from Hertzian contact mechanics via Eq. 35. [119]

$$k^* = 3\sqrt{E_R^2 RF} \tag{35}$$

Simultaneous excitement of the torsional and flexural eigenmodes of a cantilever coupled to the sample surface allows for the

Table 3Range of elastic and viscoelastic contact resonance models for measurement

Reference	Beam Shape	Modes	Surface Forces	Contact elements	Tip position
Rabe et al. (1994) [116]	Rectangular	Flexural	Normal	Spring	Fixed
Wright et al. (1997) [117]	Rectangular	Flexural	Normal, Lateral	Spring	Fixed
Turner et al. (1997) [118]	Rectangular	Flexural	Normal	Spring, Dashpot	Fixed
(Rabe et al. (2000) [119]	Rectangular	Flexural	Normal	Spring	Arbitrary
Dupas et al. (2001) [120]	Rectangular	Flexural	Normal, Transverse	Spring, Dashpot	Arbitrary
Turner and Wiehn (2001) [121]	Rectangular	Flexural, Torsional	Normal, Transverse	Spring	Fixed
Hurley and Turner (2004) [122]	Rectangular	Flexural	Normal	Spring, Dashpot	Arbitrary
Rezaei and Turner (2016) [123]	U-shaped	Flexural, Torsional	Normal, Transverse	Spring, Dashpot	Arbitrary

shear and elastic modulus to be extracted and then used to calculate the material Poisson's ratio. [124] Similarly, the simultaneous excitement of the torsional and flexural modes of a U-shaped cantilever can measure the loss tangent in-plane with and normal to the surface. [125]

To improve the either the scan speed or quantitative measurement of viscoelastic properties multiple permutations of the contact resonance method have been developed [126-132], each with some compromise between scanning speed and quantitative accuracy. [31,32,133] From the various permutations, CR AFM modes can generally be classified into either point-by-point measurements or continuous scanning measurements. Band excitation (BE), [126] and FastForce Volume contact resonance (FFV CR)[132] are examples of CR AFM modes that uses frequency sweeps or chirps to collect the entire contact resonance spectrum across a surface on a point by point basis. Alternatively, the surface can be continually scanned with one or more features of the contact resonance spectrum tracked, as of this review, dual AC resonance tracking (DART)[128, 129] remains the only continually scanning CR AFM mode capable of viscoelastic property measurement by simultaneously exciting two frequencies either side of the contact resonance peak during scanning to estimate the full contact resonance spectra.

The sensitivity of CR AFM to changes in contact stiffness is dependent on matching the effective stiffness of the cantilever to the contact stiffness. [119] [134] As such, a single eigenmode is only compatible with a defined range of material moduli for a given tip radius. [135] The use of a soft cantilever with a low static $k_{\rm C}$ and higher eigenmodes can be beneficial for conducting CR AFM on polymers as a low force setpoint can be used to engage the sample while higher order eigenmodes can be excited for improved contact resonance sensitivity. [136] Full characterization of the a cantilever's eigenmodes can be used to optimize laser spot position on the cantilever and improve sensitivity. [137] CR can also be used to probe local chemistry by using an IR pulse or other optical techniques to excite the volume underneath the AFM tip and record the amplitude and decay of the cantilever oscillation in response. [138]

By far the biggest limitation for the CR AFM when studying polymers is that stiff samples (>1 GPa) with low damping are required due to the limitations from the transfer function [31] and assumptions made in the construction of the characteristic equations. [32,118,123] Hertzian (non-adhesive) contact mechanics is the only commonly used contact model for modelling of the tipsample contact, leading to issues when dealing with adhesion in a sample, although use of the Schwarz model has been demonstrated. [33] Temperature dependent CR AFM measurements also must take into account changes in the environment that can affect the resonant frequency and damping properties of the cantilever. [139] Historically, acoustic excitation of the cantilever has led to a 'forest of peaks' due to additional parasitic resonances, making stable operation especially difficult in liquid environments. However,

this issue has been mostly addressed with the introduction of direct excitation methods. [140,141]

2.2.5. Extensions for viscoelasticity

As discussed in Section 2.1.2, viscoelastic interpretation of AFM indentations onto polymer surfaces remain fraught, especially for intermittent contact, dynamic indentations, where the tip-sample interactions are not as well defined as quasi-static methods. What follows is a summary of recent approaches for interpretation of viscoelastic measurements with dynamic AFM techniques. While single frequency dynamic AFM modes are primarily qualitative imaging modes, the phase and amplitude data channels can provide a measure of tip-sample dissipation, which is the result of different contributions for polymer samples [18,142]:

- · Adhesion
- Viscoelasticity
- · Squeeze Film Damping
- · Hydrodynamic Effects
- · Capillary Effects

Of particular interest for the characterization of polymers and other soft materials is the contrast due to adhesion and viscoelasticity between components. The theoretical and experimental work of Proksch *et al.* [18] has demonstrated that single frequency AM AFM can be used to qualitatively map the loss tangent of viscoelastic materials (Eq. 36). For the specific case where the cantilever is driven at resonance, then an estimate of the loss tangent can be calculated as shown

$$\tan\delta \approx \frac{A_1/A_{0,1} - \sin\phi_1}{\cos\phi_1} \tag{36}$$

This measure of the loss tangent is in fact a measure of the cantilever dissipation and includes additional dissipative effects beyond material viscoelasticity including the long-range surface forces, hydrodynamic effects and is less precise than loss tangent measurements made with CR AFM. [133] Methods to reduce contributions to the cantilever dissipation that are not the result of material viscoelasticity is discussed in Section 3.2.

The loss tangent for AM-FM AFM can be estimated in a similar manner to AM AFM from the decrease in amplitude (A_I) for the first resonant frequency via Eq. 36. [25,143] Observables in AM-FM AFM can also be used to calculate the compressive viscosity (η_c) and local relaxation time (τ) as follows from Eq. 37 and 38 respectively [25]

$$\eta_c = \frac{1}{2\pi\omega_1} \frac{E_{eff} E_{dis1}}{V_1} \tag{37}$$

$$\tau = \frac{\eta_c}{F} \tag{38}$$

Where E_{eff} is the effective elastic modulus from Eq. 27, E_{dis1} and V_1 are the dissipated energy and virial of the first flexural eigenmode and can be calculated from Eqs. 17-18 respectively. FM-FM

AFM also allows the calculation of viscosity through consideration of the two resonances during mapping from Eq. 39. [112]

$$\eta = \sqrt{\frac{2}{\pi^2 R A_1}} \frac{k_2^2}{Q_1 k_1} \frac{1}{f_{0,2}^2} \frac{\Delta f_2^2 (\Delta F_{0,1} f_{0,1} - \Delta f_1 F_{0,1})}{\Delta f_1^2 F_{0,1}}$$
(39)

For VE analysis of CR AFM, the dissipative component of Eq. 32 is no longer assumed to be zero and the wavenumber becomes complex $(\lambda_n L_1 = (a_n + ib_n))$. The elastic component, a and the dissipative component, b can be calculated by fitting the amplitude and phase data of a contact resonance spectra [29] or the amplitude and quality factor of the resonance peak. [144,145] Once a and b are known, Eq. 32 must then be numerically solved for a and b with the elastic solution providing an initial guess. The storage and loss modulus can be directly related to the contact stiffness and dissipation as follows in Eq. 40 if the contact area, a is known. [29]

$$E_R^* = E_R' + iE' \gamma_R = \frac{k^*}{2a} + i\frac{\pi f_n^c \sigma}{a}$$
 (40)

Challenges in measuring the contact radius of the tip has led to a comparative analysis between a sample of unknown properties and a calibration sample to obtain quantitative measurement of the reduced storage (E'_R) and loss modulus (E''_R) . By first performing a contact resonance measurement on a sample with known properties $(E'_{R,cal}$ and $E''_{R,cal})$, calibration values for the contact stiffness (α_{cal}) and damping (β_{cal}) and resonance frequency $(f^c_{n,cal})$ can be calculated and then used with Eq. 41 for subsequent measurements by measuring α , β , and f^c_n on the sample with unknown properties.

$$E_{R}' = E_{R,cal}' \left(\frac{\alpha}{\alpha_{cal}}\right)^{m}, E' \prime_{R} = E' \prime_{R,cal} \left(\frac{f_{n}^{c} \beta}{f_{n,cal}^{c} \beta_{cal}}\right)^{m}$$
(41)

By considering the dynamics of the free cantilever in conjunction with a Kelvin-Voigt representation of material viscoelasticity, the loss tangent can be determined from the CR measurement without intermediary steps or knowledge of the contact radius with Eq. 42, and differs as a measure of loss tangent from Eq. 36 due to its assumption of full tip-sample coupling rather than intermittent contact.

$$\tan \delta = \frac{\left(x_n^0 L\right)^2 \gamma^2 \beta}{\alpha} \frac{f_n^c}{f_n^{free}} \tag{42}$$

Alternative viscoelastic, dynamic AFM modes also exist that revolve around interpretation of the multi-frequency waveform that is induced by tip-sample interactions. For intermodulation AFM, [64,146-148] two excited frequencies interact and form what are termed intermodulation products during contact with the surface. The amplitude and phase of the intermodulation products can be recorded and used to calculate conservative and dissipative forces. Importantly, the technique can reconstruct a force-amplitude curve by continuously varying the oscillation amplitude while the cantilever is held at a constant z and the intermodulation products are recorded. Recently, another alternative dynamic method has been introduced, termed 'Single-Impact Atomic Force Spectroscopy' intended for operation in liquids that extracts viscoelastic surface properties through a wavelet transform analysis of the impulsive excitation of the AFM cantilever from a single tip-sample impact. [65]

2.3. Dedicated viscoelastic AFM techniques

While some of methods described in Sections 2.1.2 and 2.2.5 are capable of measuring viscoelastic properties (contact resonance) or dissipation (PFM, tapping mode, AM-FM), using an AFM to directly

measure viscoelastic properties across a broad range of frequencies and temperatures, particularly on soft adhesive materials, remains a work in progress. [7] For multi-component polymers, including composites and layered systems, the capability to map the viscoelastic properties at the nanoscale across multiple frequencies is highly desirable for developing our understanding of the altered dynamics of the polymer near interfaces. [149] To achieve this, dedicated VE AFM techniques require the ability to measure the viscoelastic properties across a range of temperatures and frequencies so that master curves can be constructed for nanoscale data and shift factors can be calculated.

Complicating viscoelastic analysis in frequency space for intermittent contact modes is that the constant impact between the tip and the sample induces resonances in the sample surface in addition to the driven tip oscillation. [89] Dynamic modes that drive the tip at or near the resonance of the cantilever are limited in their frequency dependent analysis to the eigenfrequencies available for a given cantilever. The relatively high resonant frequency of typical AFM cantilevers (>10kHz), also limits the ability of dynamic AFM to measure the nanoscale properties of a viscoelastic material and compare to the measurement made by a DMA or Nanoindentation without the use of time-temperature superposition.

One of the most obvious initial solutions for local VE properties of polymers is to use the AFM to perform a nanoscale "creep test" where the AFM tip is driven into a sample and held to maintain a constant load while the change in deflection is recorded. [150] However, nonlinearities associated with drift and creep in the z piezo in addition to possible plastic deformation of the sample result in this technique being inaccurate for long dwell times. [150] In addition, this early technique is very slow, with limited scan rates. What follows is an overview of modern AFM techniques that promise quantitative measurement of viscoelastic properties across a range of time scales and temperature. [151]

2.3.1. Dynamic scanning indentation

The dynamic scanning indentation (DSI) method introduced by Kolluru and Eaton et al. leverages the sinusoidal ramp of existing PFM modes to apply an oscillatory load to a sample surface while remaining constantly in contact (Fig. 8(a-b)). [34] As PFM is a quasi-static mode, the driving frequency of the sinusoidal ramping can be varied across multiple decades from 10 Hz to 2000 Hz. The force-displacement curves result in classic viscoelastic hysteresis loops (Fig. 8(a)) and the time resolved force and displacement exhibit the corresponding phase shift. With the inclusion of a temperature controlled cell, DSI is able to construct master curves of the storage modulus, loss modulus and loss tangent of styrene butadiene rubber as well as polyisoprene rubber by fitting the displacement $(\delta(t))$ and force profiles (F(t)) similar to bulk DMA analysis. To convert the fitted curves to modulus, a Hertzian contact stiffness and a constant contact radius is assumed due to the relatively deep indents, high rate of indentation and the adhesive materials studied. The loss tangent can be measured directly from the lag between the displacement and force profiles. Comparison to DMA data is favorable with quantitative agreement between in shift factors and viscoelastic data across multiple AFMs and rubbers. The use of the PFM mode enables DSI to be a relatively fast scanning mode compared to previous viscoelastic modes. However, as the tip remains constantly in contact with the sample while scanning, there will be large lateral forces on the tip and the sample.

2.3.2. Nano-DMA

There are several examples of techniques [35-37,47] termed 'nano-DMA' or 'nanorheology' that utilize an external actuation to oscillate the sample or AFM tip from across a broad range of

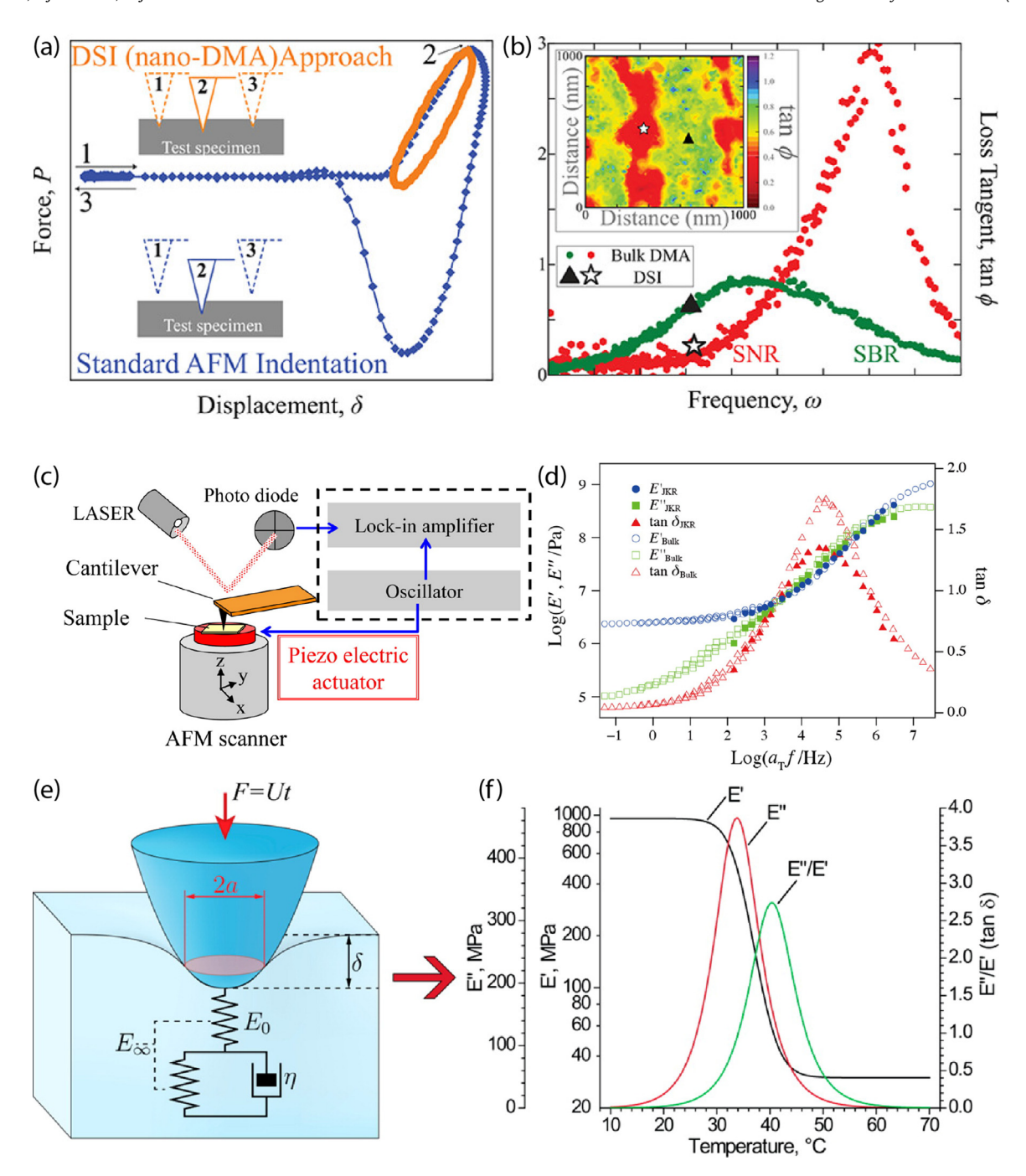


Fig. 8. (a) Comparison of a typical PFM force curve (blue) to a DSI force curve (orange). In a typical PFM force curve, tip detaches from the surface during each cycle. For a DSI curve, the sample remains in contact with the surface and the resulting force curve is cyclical as a result of material viscoelasticity and the sinusoidal ramp (b) Map of loss tangent as generated by a 64×64 pixel scan of a SBR/SNR blend. A data point take acquired from the SBR phase (triangle) and the SNR phase (star) are plotted on the loss tangent master curve generated by a DMA for each rubber. [34] Copyright 2018. Adapted with permission from the American Chemical Society. (c) Schematic of the AFM setup for nano-DMA experiments (d) Master curve generated by the Nano-DMA technique (Solid symbols) compared to a master curve acquired by a DMA (open symbols). [36], Copyright 2013. Adapted with permission from the American Chemical Society. (e) Schematic of the simple linear solid (SLS) model of viscoelastic contact during a loading-rate spectroscopy indentation. (f) Master curve generated for PnBMA under the SLS contact assumptions. [10], Copyright 2014. Adapted with permission from the American Chemical Society.

frequencies (1 Hz to 20kHz) while the AFM tip is held on the sample at a constant setpoint. A schematic of the experimental setup developed by Igarashi *et al.* [36] for viscoelastic measurements is provided in Fig. 8(c-d). By measuring the deflection response of the cantilever while the sample is oscillated, storage and loss modulus data can be constructed across a broad range of frequencies. While the displacement of the piezo used to oscillate the sample cannot be measured directly, conducting

a frequency sweep on a rigid substrate provides a reference for experiments conducted on soft materials. JKR theory for an oscillating tip on soft, viscoelastic materials [36] is used to extract the storage and loss modulus data from the measured dynamic stiffness. The nano-DMA technique and associated methods can be differentiated from contact resonance due to the use of quasi-static analysis of the cantilever motion and sub-resonant frequencies.

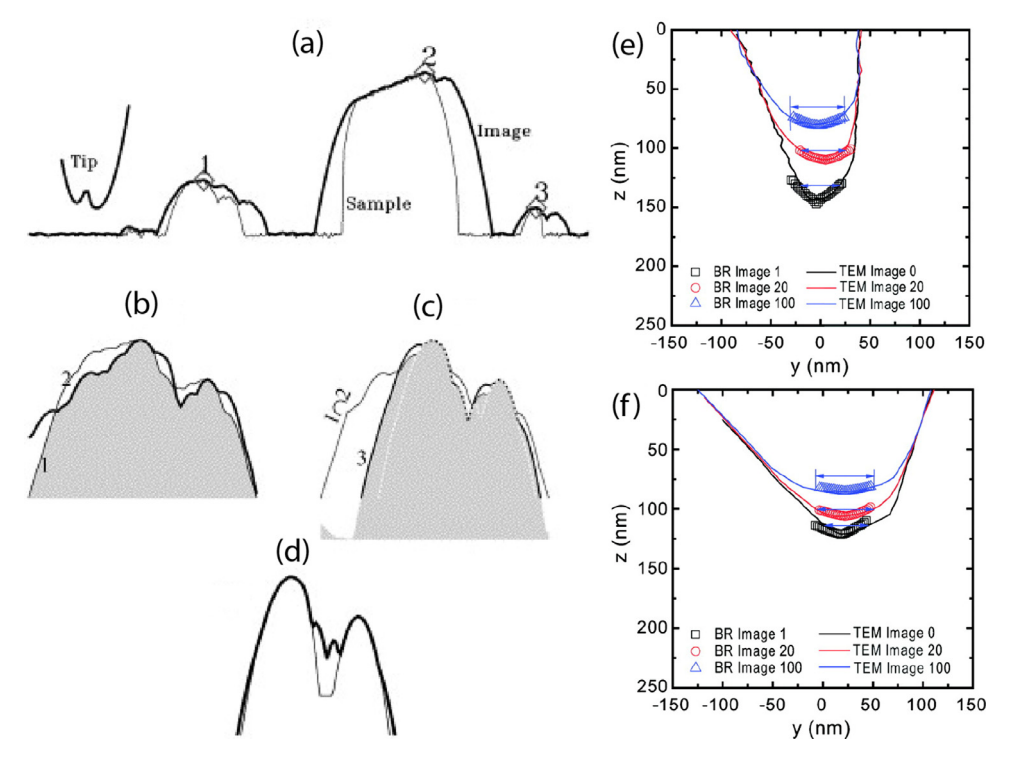


Fig. 9. Overview of scanning across a sample to perform blind tip reconstruction. (a) The true sample surface (thin black lines) and the dilated profile (thick black lines) measured by the tip pictured. Three local maxima are labelled '1', '2' and '3' at the apex of each surface feature. A multi-step tip reconstruction is then performed with (b) showing the overlap (grey shaded area) in the image maxima 1 (thin line) and maxima 2 (thick black line). (c) The intersection acquired from maxima 1 and 2 (thin black line) in (b) is then modified by including maxima 3 (thick black line) with the resulting intersection (shaded grey area) showing improvement in the tip estimation. The full blind tip reconstruction is shown in (d) with the reconstructed tip profile (thick black line) compared to the actual tip profile (line). [161], Copyright 2000. Reproduced with permission from Elsevier Science Ltd. Comparison of tip profiles extracted from blind tip reconstruction during repeated contact mode scanning on a ultrananocrystalline diamond sample (colored data points) to outlines of the same AFM tip imaged in TEM for (e) a SiN_x coated Si probe and (f) an unsharpened SiN_x probe. [165], Copyright 2010. Adapted with permission from the American Chemical Society.

Nano-DMA measurements have strong quantitative agreement with DMA data on rubbers (Fig. 8(c-d)) and the capability to create high resolution scans of heterogenous rubber blends and composites. The broad frequency range of nano-rheology AFM is useful for the local characterization of the dynamics at the nanoscale, exemplified by the work of Ueda *et al.* to examine the nano-rheological behavior of a bound rubber layer compared to the bulk rubber in a rubber-carbon black nanocomposite. [152]

2.3.3. Loading rate spectroscopy

In comparison to the frequency-space analysis conducted by the 'nano-rheology' and 'DSI' techniques, the loading rate spectroscopy method provided by Chyasnavichyus et al. examines the viscoelastic response soft polymers under constant loading rates at varying temperatures. [10,153] By changing the indentation frequency of a FV indentation from 0.125 Hz to 10 Hz, the loading rate could be varied from 37.5 nm s^{-1} to 3000 nm s^{-1} for a constant z-piezo displacement. By modelling the compliance of the PnBMA as a simple linear solid (Fig. 8(e-f)), Chyasnavichyus et al. were able to extract the viscoelastic properties by fitting the time dependent displacement data with Johnson's modified Sneddon model. The long-term modulus (E_{∞}) and instantaneous modulus can be measured independently at very slow and fast indentation rates respectively and used to convert the loading rate spectroscopy data to E' and E". Loading rate spectroscopy is limited in its analysis of viscoelastic behavior due to the assumption of simple linear solid behavior of the tested material and the conversion of time-dependent creep compliance measurements to storage and loss modulus. The use of a force volume mode also limits the scanning capabilities of the technique for collection of high-resolution scans on a polymer surface. Similar methods have been employed by other groups to extract viscoelastic property data from cells in fluids by adjusting the scanning rate in FV or PFM. [11,14] However, these studies have lacked the additional step of master curve construction using temperature variance.

2.4. Conclusions

In addition to the development of new contact resonance and bimodal dynamic AFM modes in the past decade, dedicated viscoelastic measurement modes have improved the quantitative accuracy of viscoelastic measurements and allowed for full nanoscale viscoelastic master curves on polymers. It is noted that the dedicated VE techniques are generally quasi-static modes with the tip in constant contact with the surface during analysis, eliminating other contributions that may obscure the viscoelastic material response (Section 3.2.4) and accessing a continuous range of frequencies. A number of more complicated AFM methods or analysis techniques that promise improved or more detailed measurement of surface properties have been introduced, but a lack of a centralized, open resource for the software required to conduct or analyze data from these modes has prevented mainstream uptake. No AFM mode is a one-size-fits-all solution to nanomechanical mapping on polymers and other soft materials. When choosing an AFM analysis technique to use for a given study, the additional hardware requirements, acquisition time, accuracy and flexibility of each technique must all be considered.

For rubbers and rubber composites, the soft, highly dissipative response limits the application of contact resonance techniques. While dynamic AFM can provide fast mapping of surface

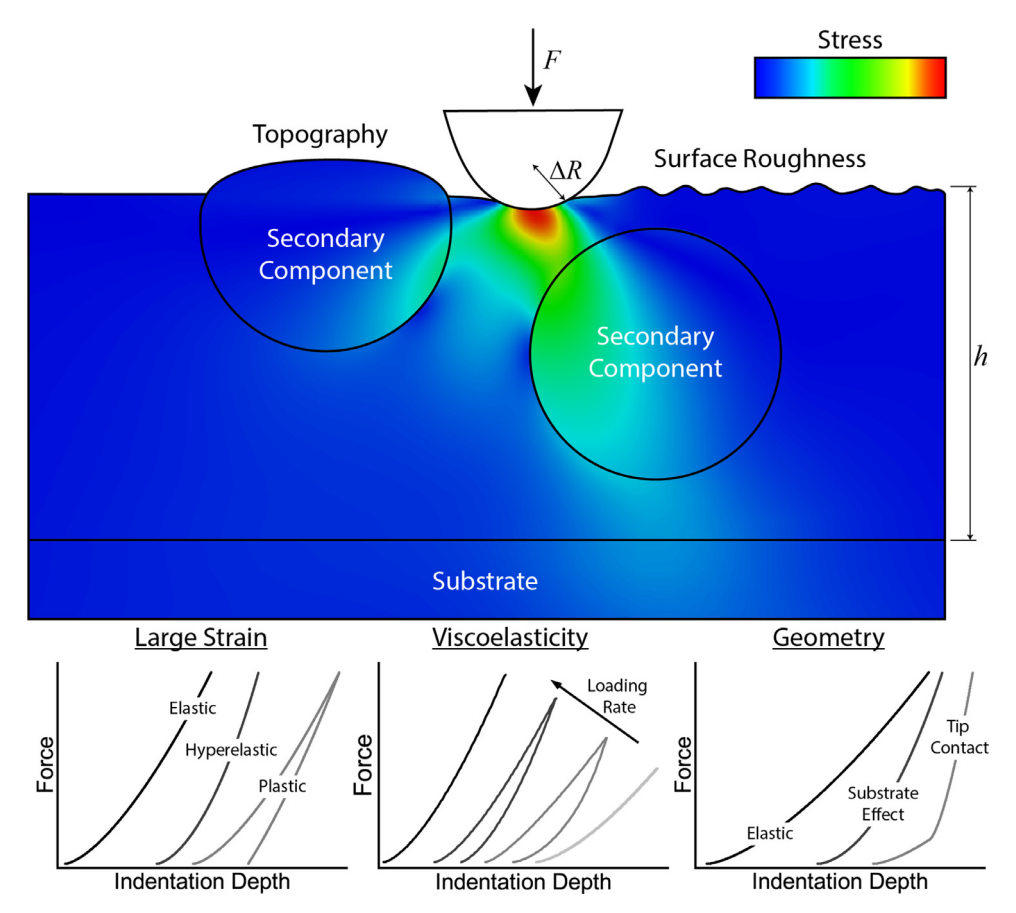


Fig. 10. Summary of non-linear impacts on an AFM measurement in heterogeneous polymers. The stress field shown is generated from a 2D plane strain FEA (finite element analysis) where the secondary component has a higher elastic modulus than the indented material for demonstration purposes. The higher elastic modulus of the secondary component means that for a given indentation depth the induced stress is higher than if the secondary components had a modulus similar to the indented material. Each of the three lower plots represents a class of non-linear deformation behavior that can impact AFM indentation on polymers. Adhesive effects have been excluded and the force curves have been shifted horizontally for clarity. For large strain conditions, the elastic curve demonstrates the ideal Hertzian case. The hyperelastic material behavior results in a stiffer response due to material incompressibility. The plastic case is the result exceeding the yield stress of the indented material, causing permanent deformation and hysteresis in the force curve. Viscoelasticity influences the indented material response based on the induced strain rate in the polymer through changes in tip shape, indentation rate and operating temperature. Finally, the geometry of the system can modify the indentation, as a nearby stiff secondary component such a particle or a substrate will result in an artificially stiff response from the indented material due to the spatial constraints. An AFM tip may also initially begin to indent into one component but as the indentation increases may directly contact a neighboring component, causing a change in deformation behavior.

dissipation and the loss tangent, acquisition of quantitative viscoelastic analysis will require either viscoelastic analysis of FV and PFM force curves or the use of one of the dedicated viscoelastic techniques. For predominantly glassy polymer blends, contact resonance can provide quantitative viscoelastic properties and the choice of exact contact resonance technique will depend on whether accuracy (band excitation) or acquisition speed (DART) is preferred. Both AM-FM AFM and quasi-static techniques can provide maps of mechanical properties, with AM-FM better for sensitivity and resolution while quasi-static methods can better interpret changes in adhesion and use appropriate contact mechanics in response for quantitative accuracy. However if, for example, a parametric study on a set of supported homogenous polymer films with different films thicknesses is required, then resolution and acquisition speed may not be a primary concern and AFM modes that provide the most accurate, direct measurement of mechanical properties would be preferred. While the above examples are not an exhaustive list of every experimental system and possible AFM modes that can be utilized, they illustrate what must be considered before choosing an AFM mode and embarking on a study using nanomechanical AFM.

3. Nanomechanical AFM experiments

The contact mechanics models discussed in Section 2.1.1 are predicated on the assumption of ideal contact conditions, where the volume beneath the tip is comprised of a single material and the contact area is symmetric. Indentation of polymers of scientific and engineering interest, including PNCs, polymer blends, biomaterials, films and other systems are rarely as experimentally simple as the picture described by contact mechanics models due to complexity from the presence of multiple components and the non-ideal behavior of the materials. Here we examine recent work that aims to the best possible measurement of mechanical properties on complex polymers, and the approaches to avoid, minimize, or correct for sources of error in AFM mechanical property measurement. This includes an examination of current AFM calibration methods and sources of error in each AFM measurement, a description of mechanical phenomena due to multi-body effects, nonlinear material behavior, environmental conditions, and the influence of sample topography on the measurement of mechanical properties. Multiple recent textbooks [86,87] and reviews [154,155] aptly demonstrate how AFM errors manifest in topography maps and so are not discussed further in this review

3.1. Calibration and operation of the AFM

It is important to recall that in AFM operation (see Fig. 1), in order to obtain the force from the measured voltages, the deflection sensitivity, S, and cantilever spring constant, k_c , must be known; in order to obtain the indentation depth the piezo displacement, z, must also be known. In addition, to calculate the modulus of the sample, E, the tip radius, R, and sample Poisson's ratio, v, must be known. The choice of AFM tip for any given experiment therefore requires calibrations to be performed to obtain estimates for R, S, and k_c . In addition to these standard calibrations, it is also important to understand errors and uncertainties in z displacement, deflection offset, contact point and Poisson's ratio. A substantive overview of AFM calibration is provided by Butt et al. in a previous review, and we augment that work by summarizing significant findings and new understandings in the intervening 15 years. [2] In this section, we first review the state of the art for each calibration typically performed for quantitative AFM experiments, providing detail on the assumptions, inherent errors, and uncertainties associated with each one. Then we summarize other sources of experimental error and make recommendations on best practices (Section 3.2) for calibration and minimization of errors for mechanical property measurements via AFM.

3.1.1. Tip radius

Table 2 shows that probe radius is a crucial component of any attempt to determine modulus through indentation. Although manufacturers often quote a range and nominal value for tip radius of their probes (e.g., "8 nm nominal, max 12 nm" or "< 10 nm"), quantitative nanomechanical AFM requires confirmation of the exact tip shape. [156] Directly acquiring some data about the tip shape is necessary for accurate characterization of the contact area [157] and helps identify tip shape drift over the course of an experiment, as well. [158] Of the methods to characterize probe radius, electron microscopy is possibly the most direct. However, electron microscopy requires substantial expertise to acquire a sharp image without altering the tip shape through heating or deposition. Furthermore, the process is laborious and offers substantial risk to the probe while handling.

A solution to these issues was introduced by Villarruba, [159] who demonstrated that scanning a suitable calibration sample having numerous sharp apexes with the AFM probe of interest would allow an estimate of the tip profile to be introduced via a blind tip reconstruction algorithm (Fig. 9(a-d)). And while advances in blind tip construction algorithms have been achieved since the work of Villarruba, [160-163] this method still requires careful choice of samples to be used for blind tip reconstruction. Probes sharper than the imaging features can result in tip estimates that are biased large and the scale of the substrate roughness also limits the depth to which the shape of the probe can be estimated. This technique's main drawbacks are the risk of altering the tip shape over the course of the calibration scan due to the hard, sharp surfaces required and the algorithmic uncertainty of the estimated tip shape. Despite these limitations, a comparison between TEM images and tip profiles from blind tip reconstruction show reasonable agreement for the tip apex (Fig. 9(e,f)). Sokolov's group has reported uncertainties of ~10% for large (~1 μ m) probes and ~35% for sharper (22 nm) probes with Villarrubia's method.[164]

Indirect, *in situ* techniques to estimate the tip radius have been demonstrated using the bistability of dynamic AFM operation [166,167], adhesion measurements, [168] local modulation of tip height and contact area with a well-defined roughness, [169] and tip-sample capacitance. [166] Alternatively, studies have avoided direct characterization of the tip radius by using a material with known, well-defined mechanical properties as a calibration stan-

dard. [170,171] Compared to direct imaging of the AFM tip, indirect methods are limited by the assumptions of the models used to extract the tip radius from a measurement and often an 'effective tip radius' is returned rather than the actual tip profile.

3.1.2. Deflection sensitivity

The deflection sensitivity, *S*, which defines the relation between cantilever deflection and voltage measured from the photo detector (Fig. 1), is a function of the specific optical configuration and alignment of the light source, cantilever, and detector. Although other configurations are possible, [172,173] most AFM instrumentation works on the principle of the optical lever, with a focused monochromatic laser or super-luminescent diode light source and a four-quadrant photodiode detector. (See Fig. 1) The variance that will be observed in the deflection signal, *V*, will be approximately the integral of the thermal spectrum up to the frequency specified by either the low-pass filter or the sampling rate of the analog-to-digital converter attached to the photodiode. The optical lever sensitivity should be maximized (i.e. minimize *S*) when optimizing a detector-noise-limited AFM because the detector noise level is independent of *S*.

"Hard contact" calibration of deflection sensitivity requires collecting an indentation curve against a substrate that is stiff enough that approximately all the piezo displacement, z, is transmitted to the deflection of the cantilever, d. (See Fig. 1) Then S is the inverse of the slope of the contact portion of the voltage-displacement curve. Although this is a straightforward process, there are several drawbacks to this "hard contact" deflection sensitivity method. First, the indentation must occur on a very hard, clean substrate; it is necessary to image the neighborhood of the indentation to ensure there is no contamination present, a step that is often omitted. Second, a substantial stress on the probe tip is required, especially for stiff cantilevers, and can often lead to alteration of the tip shape, drastically increasing the uncertainty of the probe radius in a manner that is difficult to quantify. This alteration of the tip shape can be avoided by operating in an uncalibrated mode until after the data collection is complete. However, uncalibrated operation increases error due to the third drawback, namely that the unavoidable drift in the deflection sensitivity over time demands regular re-calibration including time-consuming sample exchanges. Finally, the resulting deflection sensitivity is highly correlated with the z displacement calibration, which is especially problematic for systems operating under open-loop z position control. [174]

A "non-contact" calibration of deflection sensitivity is possible when the spring constant is obtained through a method other than the thermal method. [175] In this case, the equipartition theorem can be inverted to solve for deflection sensitivity. [176] This non-contact calibration sidesteps every drawback of contact calibration: the tip shape is preserved, there is no correlation with z calibration, and re-calibration can be performed in seconds under almost any conditions and we recommend it whenever k_c is obtainable by means other than the thermal method. An important limitation is that the thermal cantilever fluctuations are inversely proportional to k_c , so a very stiff cantilever may require unreasonable measurement times to achieve an appropriate signal-to-noise ratio.

3.1.3. Cantilever spring constant

The calibration of the cantilever spring constant has been the target of many creative efforts over the years. [177,178] However, at this time there are three methods that are in widespread use.

The most common procedure to estimate a cantilever spring constant for many years was the thermal method. [176] In this method, given a deflection sensitivity and a thermal power spectrum, the equipartition theorem specifies a spring constant. While this method can be performed on any AFM with minimal extra equipment, the measurement is very sensitive to the quality of the

estimate of deflection sensitivity; any error in S is doubled in k_c . Furthermore, this method is typically associated with a hard contact calibration of S through indentation onto a sapphire calibration sample, inviting tip damage or contamination. While the thermal method can be used in conjunction with a non-contact deflection sensitivity calibration, the error in measurement of k_c can vary between 15-50% dependent on the laser spot location on the cantilever, accuracy of the deflection sensitivity calibration and other factors. [175,179] Generally, we recommend avoiding the thermal method for spring constant calibration when possible.

The Sader method for spring constant calibration relies on the hydrodynamic behavior of cantilevers in air. [180] Derived first for rectangular cantilevers and then expanded to arbitrary plan view geometries, [181] this method offers a good approximation of the spring constant without the need for special equipment. Recently the Sader method has been applied in a new modality, [182] sometimes called $Qf^{1.3}$ scaling, [183] where measurements are considered relative to a reference cantilever (or equivalently, a tabulated hydrodynamic coefficient) and it is no longer necessary to know the exact plan dimensions, density of the air, or hydrodynamic function as long as reference data is available for equivalent cantilevers. The uncertainty of the Qf1.3 scaling method lies in four parts: the uncertainty in the estimation of the reference factor, the uncertainty in the correspondence of the cantilever being calibrated to the reference cantilever, the uncertainty in the estimation of the quality factor, Q, and the uncertainty in resonant frequency, f. When Q and f are properly measured from the thermal spectrum for a sufficiently long integration time, the reference factor is the main source of error [148] and is on the order of 10-15% for cantilevers listed in sadermethod.org. [182]

The premier method to calibrate the cantilever spring constant, k_c , is currently to use a laser Doppler vibrometer (LDV) [184] to measure the thermal velocity power spectrum of the cantilever, followed by applying the equipartition theorem to directly calculate the effective spring constant at the focal point of the laser without additional calibration. [185] There are small errors introduced by the need to locate the tip position precisely and in modeling the cantilever eigenmode, but fundamentally the measurement is limited by detector noise. [181] In other words, the calibration can be sufficiently precise, given enough measurement time, to be a negligible factor in the overall uncertainty of modulus measurements. This calibration method requires specialized instrumentation (i.e. the LDV) that is not standard equipment on commercial AFMs, so it is rarely performed by end users and more commonly used by probe manufacturers. Factory LDV calibrated probes are quoted to guarantee accuracy within 10%, so the actual standard uncertainty is probably 5% or less. An additional user calibration is unlikely to improve upon that uncertainty. For calibration of the spring constant of high order eigenmodes, the increased sensitivity of the stiffness to the tip shape and added mass limits direct application of the Sader method, [185] but cantilever specific scaling have been applied to estimate the stiffness of high-order eigenmodes based on the $Qf^{1.3}$ scaling modality. [183]

Recently a 'Standardized Nanomechanical Atomic Force Microscopy Procedure (SNAP)' was introduced in an effort to standardize the calibration procedure for AFM cantilevers to improve reproducibility of measurements, where using cantilevers with vibrometer calibrated spring constants was able to significantly reduce the variation in results between labs by using the precalibrated spring constants from LDV to calculate the deflection sensitivity from the thermal power spectrum. [186] This noncontact approach eliminates a host of problems caused by contact deflection sensitivity estimation, but also requires that special care be taken to use correct static-to-dynamic spring and sensitivity corrections.

Table 4 Calculated ratios of dynamic-to-static spring constants, ξ , and optical lever sensitivities, χ . [187], Copyright 2014. Adapted with permission from AIP Publishing LLC.

Cantilever Model No.	ξ	χ
Rectangular	1.030	1.090
AC160TS	1.101	1.254
AC240TS	1.043	1.117
BL-RC150VB(L)	1.035	1.106
BL-RC150VB(S)	1.042	1.128
FMR	1.029	1.089
NCHR	1.036	1.107
TR400(S), TR800(S)	1.054	1.130
TR400(L), TR800(L)	1.072	1.176
Triangular	1.181	1.412

N.B. The use of the χ coefficients \underline{must} be combined with a consistent positioning of the light source on the extreme end of the cantilever.

3.1.4. Dynamic vs static calibration

For simplicity, we have omitted any discussion up to this point regarding the difference between the static (k_{stat}) and dynamic (k_{dyn}) spring constant or the corresponding static (S_{stat}) and dynamic (S_{dyn}) deflection sensitivity of a cantilever. These twin properties arise due to the difference in mode shapes between endloaded, quasi-static bending and free-end, resonant bending in the small angle limit. [187] Non-contact calibration methods (e.g. thermal method) will measure the dynamic cantilever properties whereas contact methods will measure the static cantilever properties (e.g. indentation on a hard surface). Ignoring the difference between the static and dynamic cantilever properties results in substantial systemic error. We can define correction factors to convert between these properties as shown in Eqs. 43a and 43b-

$$\chi \equiv \frac{S_{dyn}}{S_{stat}} \tag{43a}$$

$$\xi \equiv \frac{k_{dyn}}{k_{stat}} \tag{43b}$$

Most AFM manufacturers have included a default value of 1.08 or 1.09 for χ and ignore ξ entirely. However, studies have shown that the size, shape, and alignment of the cantilever and light source can change these values, introducing an error of up to 100% in some cases when used for the contact calibration of k_c . [187] Therefore, for the most accurate absolute modulus estimates, researchers should use the tabulated estimates of Sader, Lu, and Mulvaney [187] to correct their calibrations (Table 4), or use the method described in ref. [187] to estimate the necessary values, either through finite element calculation or by comparing force and amplitude ramps.

3.1.5. Poisson's ratio

The sample Poisson's ratio, ν is typically of secondary interest to AFM practitioners. However, an estimate of ν is necessary to calculate a final absolute Young's modulus through the equations in Table 2. Some papers have cited uncertainties as high as 0.1 for polymers, a 25% error for glassy polymers. [164] This error is somewhat suppressed when propagated through to the modulus error, but nevertheless the uncertainty of ν contributes an additional 7% to 15% error to the modulus estimate. Therefore, it is crucial to obtain a better estimate for a specific material at experimental conditions to produce quantitative modulus maps. The ability to measure this material property locally at the nanoscale is sorely needed but so far remains elusive on polymers.

3.1.6. Piezo displacement

Fine position control in AFM is often provided by piezoelectric translation mechanisms. These mechanisms have well-known

nonlinearity, hysteresis, and creep in their voltage response profiles. [188,189] For small, repeated motions, the motion of a piezo stage can be approximated as proportional to the applied voltage. The random uncertainty of this positioning is limited by the voltage source noise and can be effectively very small (under 10 picometers). The voltage-displacement proportionality is a calibration factor that should be estimated at the specific amplitude and frequency of the desired experimental conditions to minimize the systematic uncertainty. Wagner et al. [174] was able to estimate the calibration factor for a relatively small displacement of 8 nm with a relative error of 7%. However, it is not clear if efforts were made to match the frequency and amplitude of calibration to the subsequent experiment. Holman et al. [189] showed that, for larger amplitudes the calibration factor can change by as much as 30% depending on the voltage range, and the hysteresis shift factor can add a bias of 10 - 15% of the voltage range. These offsets were modeled empirically to as low as 0.1% error but it is impractical to do so in the context of an AFM without precise real-time position measurement.

Responding to these problems, manufacturers have added capacitive or LVDT position measurement to the translation mechanism to enable "closed-loop" (feedback-controlled) mode operation. In this mode, the applied piezo voltage is controlled to produce the desired position transducer voltage, eliminating piezo nonidealities. The transducer itself needs a calibration, but this calibration is generally valid over a larger range of frequencies and amplitudes. Along with systemic calibration error, closed-loop systems introduce extra random sensor noise that is usually specified by the instrument manufacturer and is on the order of 100 picometers.

3.1.7. Deflection offset

In determining the force resulting from cantilever deflection, it is necessary to set up the system such that the apparent deflection is zero when the cantilever is experiencing zero force (see Fig. 1). Originally, this was a matter of carefully aligning the reflected beam in the center of the four-quadrant detector. However, this manual alignment is subject to various low-frequency drifts [190] and will substantially bias force measurement over time. The use of "relative" force measurements, where a force offset voltage V_0 is subtracted from each indentation, mitigates this drift problem. The algorithms that a manufacturer might use to calculate V_0 in real time are typically undocumented, so we do not discuss such algorithms here. In force curve analysis, practitioners typically obtain the V_0 from least squares fits of low-order polynomials to the approach and departure regions of the force curve (Fig. 3) manually, although algorithmic options exist. [76] The systemic bias from the choice of fit region and the order of polynomial is difficult to quantify, especially in the presence of interfering physical phenomena such as long-range potentials, surface reflections, and adhesion snap-off and ring-down. Such physical interference is best removed by altering experimental conditions or by direct modeling of the interfering phenomenon. The random noise from such fits is (under modest assumptions) [191] proportional to the detector noise and inversely proportional to the square root of the number of data points fitted. Thus, with any substantial number of fitted points this noise can typically be neglected.

3.1.8. Displacement offset

As discussed in Section 2.1, simple AFM contact models are defined in terms of the indentation depth, which must be calculated in terms of the measured cantilever deflection, d and the displacement, z. Similar to the cantilever deflection, an offset is required to shift the output of the calibrated z sensor so that it reads zero when the unperturbed tip and surface would hypothetically be co-

incident. In the case of pure, non-adhesive Hertzian contact, the zeroed displacement is equivalent to the point of contact, z_0 .

There are many ways of choosing z_0 that range from informal to algorithmic. [192,193] However, the resultant output of these methods varies greatly, and many have narrow/specific applicability. The importance of z_0 is often overlooked, even though it has been shown that modulus estimates can be very sensitive to the selection of the contact point. [76,80,194]

One paper [195] provides rigorous inference and uncertainty quantification of z_0 , where they found an uncertainty of approximately 10 nm was found on the contact point of an approximately 700 nm indentation (1.4 % error). Even in this case, with modest noise levels and unimpeachable data analysis, the relative uncertainty due to z_0 is responsible for about 40% of the overall uncertainty in the Young's modulus estimate. However, the algorithm is specific to Hertzian contact, computationally intensive, and mathematically complex, and thus is unlikely to find wider application.

Other authors have attempted to automate force curve analysis more generally, including finding the contact point, Lin, Dimitriadis and Horkay [76,80] have offered a decision tree of least squares fits hoping to capture a large variety of interaction laws and interference issues, including z_0 determination. Melzak et al. [196] and Fujinami et al. [82] propose that the contact point should be inferred entirely from fitting data well into the contact regime through linearization. Benítez et al. [193] developed a thresholdbased algorithm around local linear regressions. All of these algorithms are manageable in complexity and comparable in performance and robustness. However, they lack rigorous uncertainty quantification or discussion on biases of their contact point determination. A need remains for a rigorous, robust, and tractable method to infer the uncertainty in z_0 from AFM force-displacement curves. In the meantime, the effect of this source of error can be minimized in practice by increasing indentation depth when possible, as will be explained further in the following sections.

3.1.9. Hertz model error propagation

We have listed examples of publications that confront the question of uncertainty and error propagation directly. However they are narrowly focused on a specific system and location in parameter-space, making their conclusions difficult to generalize. [174,197] In a recent work, we analyzed the first-order linear error propagation of a simplified model from which we drew general recommendations on how to best eliminate modulus measurement error in practice, which we will summarize here. [198] Applying the chain rule for each of the error sources discussed in this section to the inference of the Young's modulus *via* the paraboloid Hertz contact model (Table 2), along with some algebraic manipulation, we obtain the equation for the relative error in the estimated modulus.

$$\left(\frac{\Delta E}{E}\right)^{2} = \left(\frac{1}{2}\frac{\Delta R}{R}\right)^{2} + \left(2\frac{\Delta \nu}{\nu^{-1}-\nu}\right)^{2} + \left(\frac{\Delta k_{c}}{k_{c}}\right)^{2} + \left(1 + \frac{3}{2}\frac{d}{\delta}\right)^{2} \left(\frac{\Delta S}{S}\right)^{2} + \left(1 + \frac{3}{2}\frac{d}{\delta}\right)^{2} \left[\left(\frac{\Delta V}{V_{1}-V_{0}}\right)^{2} + \left(\frac{\Delta V_{0}}{V_{1}-V_{0}}\right)^{2}\right] + \left(\frac{3}{2} + \frac{3}{2}\frac{d}{\delta}\right)^{2} \left[\left(\frac{\Delta z}{z_{1}-z_{0}}\right)^{2} + \left(\frac{\Delta z_{0}}{z_{1}-z_{0}}\right)^{2}\right]$$
(44)

With this equation, we can understand the influence of each of the key parameters and their calibration or measurement uncertainty on the accuracy of the modulus calculation. Eq. 44 can be divided into two parts, representing systematic (whole-image, from R, ν , S, and k_c) and random (pixel-wise, from V, V_0 , z, and z_0) errors. A remarkable feature that is immediately recognizable is the presence of a dimensionless factor, d/δ , the ratio of deflection to indentation depth. This ratio is a measure of the fraction of the compliance of the system that is due to the movement of the cantilever versus the movement of the substrate. If this quantity is allowed to grow, all else being equal, it will scale the random

error components as well as the deflection sensitivity component. This dependence of error on d/δ is also in direct agreement with the findings of Wagner *et al.*,[174] where the deflection sensitivity calibration was the dominant component of modulus error due to excessive compliance of their cantilever.

When the correlation between S and k_c introduced by noncontact (or contact) thermal calibration is accounted for in the error propagation, the dependence of the modulus error due to k_c (or S, respectively) seems to disappear at a special indentation ratio of $d/\delta = 2/3$ as a consequence of oppositely-signed contributions from deflection sensitivity error via deflection and indentation. This surprising result was demonstrated experimentally for several polymer systems in [198]. In these experiments, the modulus sensitivity to k_c approached zero for real force curve fits at the "magic" indentation ratio of $d/\delta = 0.55$, remarkably close to the ideal value of 2/3. Note that calibration is still important when testing at the magic ratio value for d/δ ; error in k_c still affects distances, depths, and forces measured in the system even at these special conditions.

3.1.10. Scanning considerations

As the AFM rasters across the sample surface, measurement of the surface properties is influenced by any changes in topography, contact mechanics or operating conditions. Ensuring accurate mechanical property measurement during AFM scans can be influenced by the control loop feedback settings, choice of cantilever used, driving frequency, operating environment, and the scanning mechanism. 'Video-rate AFM' or fast scanning AFM, has seen intense research interest to capture dynamic processes, particularly biological, over short time scales. [199,200]Fast scanning AFM generally requires operating in fluid with small cantilevers and with custom hardware to enable the fastest scanning speeds. [201] Here optimization of scanning parameters for accurate mechanical property measurement is discussed.

For dynamic AFM, selection of cantilevers for mechanical property measurement has multiple aspects that must be considered, especially for viscoelastic properties. Generally for dynamic AFM the cantilever stiffness should be set to match the expected contact stiffness of the material for best sensitivity to changes in material properties. [202] When measuring viscoelastic surface properties and obtaining viscoelastic contrast, attention should be paid to the expected relaxation times of the phases present and whether the fundamental resonant frequency of a cantilever or one of its higher eigenmodes is suitable to discriminate between them. For quantitative dynamic AFM, analytical calculation of mechanical properties in AM AFM and AM-FM AFM (Sections 2.2.3 and 2.2.5) requires assumptions about the interaction between the oscillating tip and the surface forces which set boundaries on the free air amplitude, A_0 and the setpoint, A_{sp} . The most impactful is the assumption of Hertzian contact, where adhesive forces are required to be insignificant, both relative to the magnitude of repulsive forces acting on the tip and that the length scale of adhesive forces is small relative to the amplitude of oscillation. [18,25,28]

Reducing the impact of adhesion on property measurements in AFM generally requires deeper indentations and higher forces be applied by increasing A_0 so that the repulsive force exerted on the tip is larger than the attractive forces. Targeted measurement of dissipated energy due to surface viscoelasticity, adhesion, or some other mechanism can be achieved by careful selection of $A_{\rm sp}/A_0$. [203,204] While cantilever selection is often dictated by choosing a $k_{\rm c}$ and $\omega_{\rm i}$ to enable sensitivity to changes in surface properties, cantilevers with low Q may also dissipate energy to higher harmonics during contact, artificially increasing the measured dissipation and resulting in a systematic error during property measurements. [205]

For scanning in AM AFM, the cantilever resonant frequency, f_n , and quality factor, Q_n , for a given eigenmode will also influence the control loop and response to changes in the surface properties and topography while scanning. The mechanical bandwidth (B_n) of a given cantilever and excited eigenmode is related to the resonance frequency and quality factor [206] as follows in Eq. 45

$$B_n \propto \frac{f_n}{Q_n} \tag{45}$$

A large B_n is desirable to minimize the response time ($\tau_n \propto$ $1/B_n$) to a change in the sample topography or properties. Since an oscillating cantilever requires a number of cycles to respond to a change during a scan, increasing the resonant frequency of the cantilever reduces the time required to complete a given number of cycles, and reducing the Q-factor reduces the number of cycles required. [207] Active damping control, often called 'Q-control' in AFM, can be used to increase the scan rate and improve sample tracking by modifying the excitation signal. [206] While scanning in dynamic AFM, 'snap-to-contact' instabilities can occur due to mode hopping, resulting in poor surface tracking and risk of tip or sample damage. By selecting a cantilever or eigenmode with a stiffness such that $k_{\rm C}>k_{\rm ts}^{\rm max}$ or a free-air amplitude such that $k_c A_0 > F_{adh}^{max}$ within the attractive regime, the 'snap-to-contact' instability can be removed, as the restoring force of the cantilever oscillation will always be larger than the force exerted on the tip by surface forces. [208] On rough surfaces, multiple contact asperities between the tip and the surface can increase the maximum restoring force, k_cA_0 required to maintain stable scanning in the repulsive regime. Generally, the free air amplitude should 2-3× larger than the surface roughness to prevent the tip decoupling from the surface in AM AFM, [200] although this is dependent on the setpoint ratio. [209]

For contact resonance techniques, the cantilever should be chosen to optimize sensitivity to changes in contact stiffness. [135] If the fundamental resonance of a cantilever is not suitable, then the higher eigenmodes can be considered for contact resonance measurements. [136] If higher eigenmodes are used, then careful positioning of the laser is required so that the spot position is aligned with an antinode. [137] Accurate measurement of surface mechanical properties requires that many of the extraneous influences on the cantilever's motion is controlled for, so measurement of the free air resonance should be conducted close to the sample surface [5] and corrections for hydrodynamic damping should be made to the contact resonance measurement. [210] An increase in scan speed during the measurement of mechanical properties has been shown to influence the measured viscoelastic properties using DART-CR and BE CR AFM, with a higher loss tangent measured with increasing scan speed. [32] As such, while continually scanning techniques such as DART-CR are preferable for fast acquisition times, the best accuracy is achieved with full spectrum, point-by-point measurements. DART-CR AFM with soft cantilevers and their high-order eigenmodes were used to compare the mechanical properties of several biopolymers and fillers, where it was found that removing erroneous measurements due to scanning artifacts improved the quality of the acquired dataset. [211,212]

For quasi-static modes, cantilever selection for quasi-static modes should be such to optimize the cantilever deflection relative to the anticipated indentation depth to reduce systematic error based on the tip radius and expected sample modulus. [198,213] Scan speed artifacts can be significant in PFM compared to FV, as feedback control is necessary to keep the tip engaged at a constant force setpoint while scanning. Beyond limitations to the scan speed of PFM due to the driving mechanism, accurate measurement of adhesive forces require that acquisition rates are 2-3 orders of magnitude smaller than the fundamental resonant frequency of the cantilever in order to minimize the influence of hydrodynamic drag

and inertia. [16] Increasing the density of data points collected in PFM scans can improve surface tracking and setpoint control, as the feedback loop more easily responds to the smaller changes in sample height and properties between pixels. Adjusting the oscillation amplitude so that 10-30% of the data for a single curve is acquired while the tip interacts with the surface is a good rule of thumb for providing enough of a base line for contact point determination while providing sufficient resolution for model fitting to acquired force curves. The z-modulation loop amplitude should be sufficiently large so that the base line is maintained across changes in topography, sample modulus and adhesion.

While conducting AFM images in liquid can be beneficial to improving scan speed, allowing in-situ imaging of biological samples, and minimizing adhesion due to removal of capillary effects, operating in liquid lowers the Q of the cantilever and may introduce additional noise. [214] Additionally, the hydrodynamic effect becomes significant in liquid [215], limiting the maximum speed of cantilever motion in quasi-static modes without baseline correction. [50,216] The hydrodynamic effect is most important for materials with low tan δ (<0.1) and when using the first resonance mode or in static mode operation. Estimation of the impact of hydrodynamic damping can be conducted by measurement of Q and f_0 near the surface [210] or from a predictive model of hydrodynamics effects. [217] Another source of dissipation during scanning is squeeze-film damping, which is the result of the fluid between the cantilever and the sample surface being compressed during a cantilever oscillation. As the distance between the cantilever and the sample surface is critical to the impact of squeeze film damping on an AFM measurement of dissipation, [215] any correction for squeeze film damping must take into account the change of surface topography across the scanned area. A nap pass can be conducted to remove squeeze film damping effects by measuring the cantilever response at a small set distance above the sample surface. [142]

Prior to scanning with all modes, approaching and engaging with the surface can be a major cause of tip damage and fracture in AFM, impacting the validity of subsequent measurements. [218] Using small-amplitude AM AFM while engaging the surface can reduce the load on the tip as the tip is encouraged to engage the sample surface within the attractive regime. Reducing the zpiezo ramp rate during the engage process can also reduce the impact load, minimizing the possibility of tip fracture.

3.1.11. Recommendations and best practice

Here, we summarize calibration recommendations in Table 5 resulting from this review on the current state of the art for AFM calibration to obtain accurate property measurements.

Operation parameters of AFM experiments are very system and mode specific and can be optimized further for a specific property measurement. Some general suggestions on setting up a nanomechanical experiment for the most common modes are given in Table 6. Establishing the best operating procedures for a given sample and mode will generally require some iteration, although simulations of indentation can be helpful for providing a sense of what is required for accurate property characterization of a given polymer system and accelerate the development of experimental procedures.

3.2. Influence of mechanical phenomena on property measurements

To create the methods and models to describe AFM operation and extract surface properties, assumptions are made about the cantilever dynamics, tip-surface interactions, and material behavior. However, all of these approaches assume that the AFM tip is probing a sample which can be represented as a semi-infinite half space with an expected material deformation behavior. In many

polymers studied by AFM, idealized models of the tip-sample interaction and indentation can break down (Fig. 10) due to complications from underlying substrates, inhomogeneities or embedded phases with different properties than the indented polymer. The magnitude of deviation from the idealized case can vary depending on where the AFM tip is indenting on the sample, with irregularities in the tip shape, depth of indentation and adhesive interaction strength complicating the applicability of the contact mechanics expressions used to convert force and displacement to properties (Table 2). Furthermore, when the length scale of indentation approaches 1-10 nm, the measured properties may be influenced by free surface effects and variations in polymer dynamics. This section reviews the body of work that seeks to understand these complications to measurement of the mechanical properties in heterogeneous polymer systems.

3.2.1. Stress Interaction effect ('the substrate effect')

When indenting into a material, the probe is sensitive to material properties in the perturbed volume underneath the tip. The size of the perturbed volume depends on the indentation force and the tip shape (Fig. 11(a)) and extends beyond the material directly underneath the tip radius. [219] If the probed volume includes a second component or another material with different material properties, then the measured response from the AFM will have contributions from multiple components. [220] This 'stress interaction effect' can occur in all samples with multiple components, but is especially prevalent when indenting into soft materials supported by stiff substrates (Fig. 11(b)), [221] and as such this phenomena is also commonly referred to as the 'substrate effect' or 'thin film effect'. The stress interaction effect will alter the measured mechanical properties artificially by skewing the forcedisplacements measured - for example, for a given indentation depth the corresponding stress field and consequently indentation force reported will be higher if the tip is in the neighborhood of a stiff substrate or inclusion compared to an ideal case (Fig. 11(b-d)). The skewed measurements introduce apparent property gradients that are not the result of real changes in inherent material properties but simply reflect changes in the fraction of two components in the probed volume. In soft composites and blends, the substrate effect can blur the determination of where one component ends and the other begins. Under confinement of the indented material between the tip and the secondary phase, the induced stress in the material can dramatically increase. [222] In some cases, the substrate effect can be leveraged to conduct 'stiffness tomography' to map the stiffness of samples vertically as well as in the x-y plane. [223,224] Subsurface features and structures can be resolved using highly sensitive contact resonance techniques to resolve 50 nm features up to 300 nm from the surface. [225-227]

For the case of supported soft materials on stiff substrates, analysis of the top down substrate effect (Fig. 11(b)) for a range of tip geometries, soft materials and film thickness regimes (Table 7) have been compiled. Broadly, for all studies corrections are needed to account for the substrate effect ((Fig. 11(b)) when the contact radius becomes some significant fraction of the film thickness (a/h). A traditional rule of thumb has been that the indentation depth, δ should not exceed 10% of the total film thickness to avoid substrate effects. However, Clifford et al. [170] suggests that the 10% rule is often not reliable and determining the onset of the substrate effect in supported films must also take into account the difference in elastic modulus between the indented material and the substrate, the Poisson's ratio of the indented material and the adhesion between the indented material and the substrate. For cases where the indented material is viscoelastic, then the effect of a stiff, elastic substrate must be included while fitting creep compliance curves and other viscoelastic tests. [228] Recent efforts have

 Table 5

 Recommended calibration steps for accurate property measurements with quantitative AFM modes. Supporting citations and reasoning is provided in the sections noted.

Calibration step	
(Section)	Current best practice and recommendations
Tip radius, <i>R</i> (3.1.1)	Blind tip reconstruction before and after an experiment by scanning a standard roughness sample with comparison against SEM or TEM images for validation of tip reconstruction algorithm parameters. Scans used for blind tip reconstruction must be conducted at sufficient pixel resolution and density that the entire tip is sampled. Parameters for the reconstruction algorithm can be established according to Flater <i>et al.</i> [160]
Cantilever Spring constant, k_c (3.1.3)	Calibration with LDV before use in AFM or Sader ($Qf^{1.3}$) method at a tip-sample separation that is at least $2\times$ the width of the cantilever. For the Sader method, acquire as much thermal spectrum data as reasonably possible before fitting to minimize error.
Deflection Sensitivity, S (3.1.2)	Noncontact calibration through the equipartition theorem with predetermined cantilever spring constant. Optical lever sensitivity should be maximized for the chosen cantilever through choice of spot location
Force Setpoint, F_{max} (3.1.9)	Choose a setpoint point that maintains $d/\delta \approx 2/3$ for the calibrated spring constant, tip radius and expected sample modulus
Poisson Ratio, v (3.1.5)	Estimate ν from bulk data at the appropriate frequency and temperature. If operating near T_g for a given analysis frequency be aware changes in operating temperature or analysis frequency can change the polymer's ν .
Detector and z-sensor, V and z (3.1.6-8)	Maintain $V_0 \approx 0$ by zeroing the photodetector before indentation. Fitting the baseline of the force curve can remove residual offsets in the deflection channel. For the z-position, eliminate features in an experiment (such as the water monolayer) that may complicate contact point determination (z_0) . Maintain δ much greater than the intrinsic noise values Δz_c , Δz , Δd .
Dynamic-static conversion factors, ξ and χ (3.1.4)	Use tabulated data (Table 4) for specific cantilever geometries with a consistent spot location. Measure static and dynamic deflection sensitivity factors to estimate the dynamic-static conversion factor for a given cantilever and laser spot position.

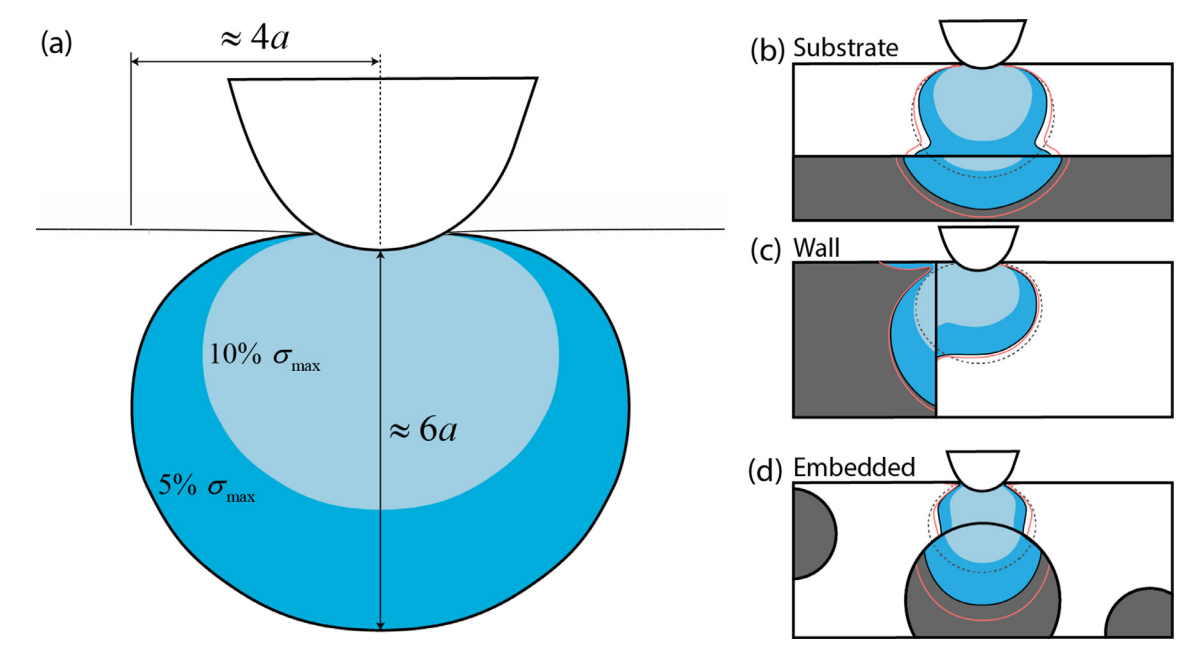


Fig. 11. Perturbated zone underneath the AFM tip visualized by considering where the von Mises stress of the material is at least 5% (dark blue) and 10% (light blue) of the maximum von Mises stress, σ_{max} . Perturbated zone in (a) homogeneous infinite media, near a (b) stiff substrate, (c) wall and (d) embedded phase. The stiff phase is represented as dark grey. The dotted light grey line indicates the perturbed region in (a) where the von Mises stress is at least 5% of the σ_{max} . The solid red line denotes the region where the von Mises stress in the confined geometry is at least 5% of the σ_{max} from (a). In all the confined geometries, the symmetric stress field in (a) becomes distorted and the maximum stress is elevated due to the stiff, second phase. The stress fields are adapted from axisymmetric (a, b, d) and three-dimensional (c) FEA simulations of indentation into rubbery polymers.

also been made to include substrate effects on viscoelastic analysis of indentations into living cells. [229,230]

There is limited analysis on the temperature dependence of the substrate effect for polymers. Work by Song, Kahraman and Collinson *et al.* [222] using both molecular dynamics and finite element simulations of AFM indentation has established that as sample temperature increases through $T_{\rm g}$, the magnitude and extent of the stress interaction effect decreases due to increased viscous dissipation for unconfined polymers (Fig. 12(e)). However, for highly confined films an accompanying increased incompressibility

with temperature combats the impact of increased viscous dissipation (Fig. 12((b-c)) and an increase in the relative stress interaction strength is observed (Fig. 12a-e). These results indicate that changes in the continuum properties of the polymer with temperature can convolute interpretation of experimental data. For example in Fig. 12(g-h), the heightened properties of thin films observed in the rubbery regime compared to the same film in the glassy regime may be the result of an increase in Poisson's ratio (i.e. incompressibility) rather than polymer-substrate surface interactions.

Table 6General experimental methods for accurate nanomechanical measurement of viscoelasticity in air with the most prevalent scanning nanomechanical AFM modes. Supporting citations and reasoning is provided in Section 3.1.10

Setting	Quasi-Static	Amplitude Modulation	Contact Resonance	
Cantilever Selection ^a	 Choose k_c to satisfy d/δ = 2/3 Lower f cantilevers will limit z-modulation speed and amplitude due to ring-down. 	 Choose k_c to overcome adhesive forces and match tip-sample contact stiffness. For VE, chosen ω_i should be sensitive to material relaxation time. 	• Choose cantilever with $k_{\mathrm{c,i}}$ to optimize sensitivity to Δk	
Setpoint	 Choose F_{max} to operate in linear VE regime if possible. Larger F_{max} aids scan stability 	 Choose A₀ to limit snap-to-contact behavior Choose A_{0,i} and A_{sp,i} to satisfy assumptions on contact and forces acting on the tip during oscillation A_{sp} should be optimized for VE contrast. Large A₀ improves assumption of Hertz contact in air A final tune of the cantilever should be conducted close to the surface (≈500 nm) before scanning 	 Drive amplitudes for CR should be small compared to contact force to satisfy linear tip-sample contact A final tune of the cantilever should be conducted close to the surface (≈500 nm) before scanning Use the free hydrodynamic function to correct contact Q 	
Scanning	Increasing pixel density and decreasing scan speed can improve scan stability • Choose z-modulation amplitude so 10-30% of the ramp is in contact. • Modulation speed can be reduced to increase contact data	 Operating in dry N₂ minimizes water monolayer, a source of dissipation. Lower scan speeds improve accuracy in dissipation measurements. Scan speed is limited by cantilever bandwidth A₀ should be 2-3× the surface roughness for surface tracking 	 Parametric CR (e.g. DART CR) accuracy can be improved with lower scan speed. Point-by-point, full spectrum methods is preferred for accuracy, with scanning methods preferred for speed 	
General	 Increase gains until height channel trace and retrace overlap for surface tracking Increasing gains until just below feedback instability provides more aggressive tracking for uneven surfaces Operating in liquid can allow for faster scanning due to decrease in Q. Hydrodynamic drag can be identified by hysteresis in the approach and retract components of the baseline deflection (QS) or in the phase and Q. Hydrodynamic effects can be minimized by reducing scan speed, using small cantilevers or applying baseline corrections. Engaging with the surface should be conducted using small amplitude AM AFM and slow z-piezo modulation if possible so that the surface is detected within the attractive regime, minimizing tip-sample forces before scanning. Laser spot location should optimize optical lever sensitivity. For dynamic methods utilizing high-order eigenmodes, the laser spot should be situated on an antinode. 			

^a Simulation of AFM for a given cantilever and varying surface viscoelasticity can aid in selection of a cantilever with appropriate dynamic range and approximate scan settings.

Table 7Analytical and semi-empirical models developed to account for the substrate effect for indentation on soft materials supported by a stiff substrate. In this table, h is the indented film thickness, a is the contact radius, δ is the indentation depth and R is the tip radius In the first column the compatible contact mechanics and tips used for indentation in the study are provided

Contact Mechanics	Material	Constitutive Model	Film Thickness	Substrate- Film Boundary Condition	Ref.
Hertz (Sphere) $R = 15-25 \text{ nm}$	PnBMA	Elastic	0-200 nm $(a/h = 0 - 14)$	Fixed	[231, 232]
Hertz (Sphere)	Polymer Brush	Elastic	1 - 100 nm	Fixed	[233, 234]
Hertz (Sphere)	Hydrogel	Elastic	a/h = 0.02 to 2	Fixed and	[194]
R = "sharp", 2 μ m, 5 μ m	•			Sliding	-
Sneddon (Conical, $R = 20 \text{ nm}$)		Elastic ($\nu = 0.5$	1 μ m to 15 um ($\delta/h = 0.1$ to 1)	Fixed	[235]
	Polyacrylamide, Fibroblasts	only)			
Hertz	Polyacrylamide	Neo-Hookian	52-134 μ m ($\delta/h = 0.1$ to 0.4,	Fixed	[236]
(Sphere, $R = 100 - 250 \mu m$)			R/h = 0.3 to 6.2)		
Hertz (Sphere, $R = 1030, 232 \text{ nm}$)	PMMA	Elastic	a/h = 0 to 5	Fixed	[237]
Sneddon	Analytical	Viscoelastic (creep)	(a/h = 0.01-10)	Fixed	[238]
Hertz (Sphere, $R=1.5$ -4 μ m)	Fibroblast	Viscoelastic (dynamic)	$(a/h \approx 0.3-2)$	Fixed and Sliding	[239]

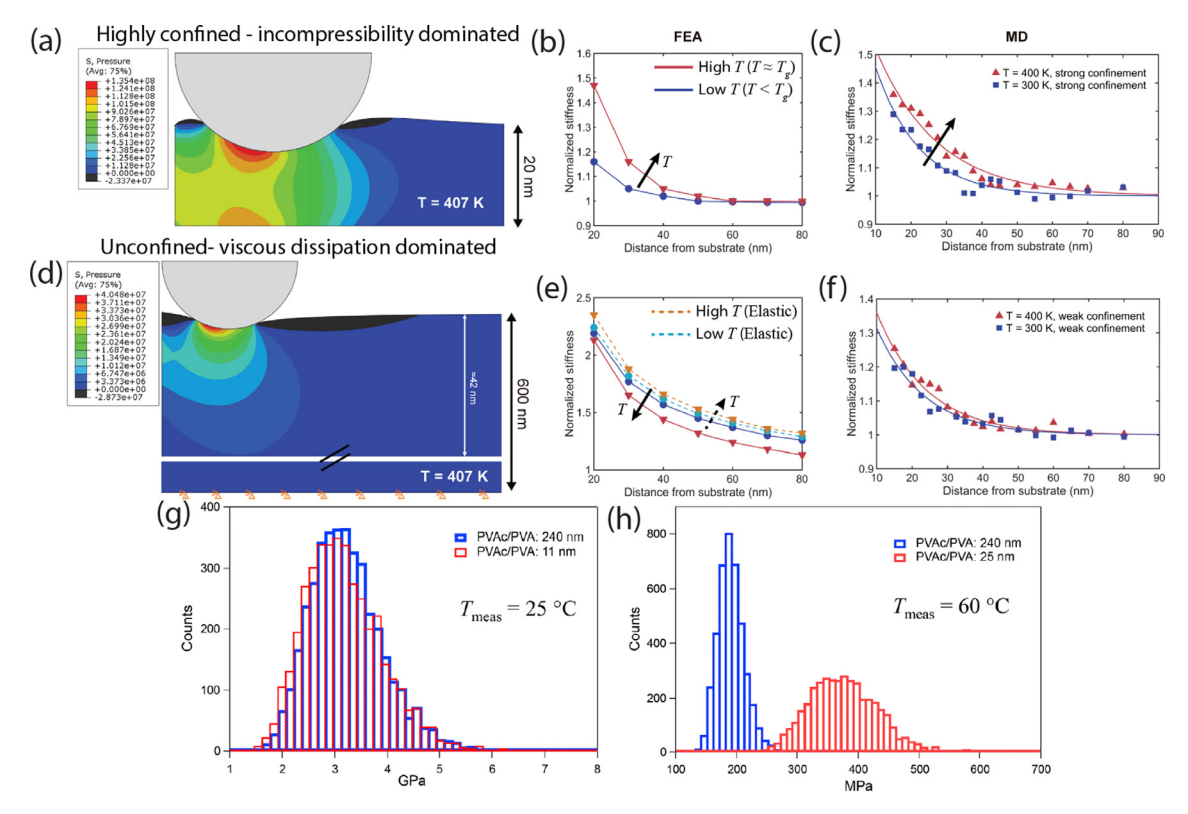


Fig. 12. (a-f) Consider MD and FEA results of indentation of a polymer near a wall as in Fig 11c; (a-c) consider a very close substrate as in Fig 11b in addition to the wall. (a) Contours of hydrostatic stress near the fixed boundary condition are shown in a (a) 20 nm and (d) 600 nm thick film from a FEA simulation of a 5 nm indentation with a 20 nm tip radius. The center of the tip is 20 nm from the interface. Normalized stiffness profile as measured by (b) FEA simulation and (c) CG-MD of an AFM indentation below T_g and near T_g into the highly confined film. Arrows indicate the change in stiffness profiles with temperature (e) Normalized stiffness profiles of AFM indentations into the loosely confined film below and near T_g with viscoelastic effects included and excluded from the material model. For the elastic simulations, the modulus and Poisson's ratio of the indented material is still altered to reflect the material properties at each temperature. (f) CG-MD of the highly confined film identical to the system in (d), but with a softer boundary condition specified for the substrate. [222], Copyright 2019. Adapted with permission from the Royal Society of Chemistry. Histogram of measured JKR modulus on thick and thin PVAc films at (g) 25°C (h) 60°C. The T_g of the PVAc is 38°C. Data is acquired from a 64×64 set of FV AFM curves. [240], Copyright 2016. Reproduced with permission from Elsevier Science Ltd.

3.2.2. Tip effects

For imaging of surface features, the size of the tip represents a limit to the achievable resolution with AFM as the finite tip size controls the extent of the probed volume during indentation. Bahrami et al. finds the spatial resolution of adhesion measurements to be twice the contact radius at pull-out and the local modulus resolution to be four times the maximum contact radius while operating in PFM. [241] The finite size of the tip also comes into play when indenting across two components. As the tip moves across an interface, the proportion of the two materials that are indented by the tip change resulting in a sigmoidal profile across the interface of the two materials that reflects the mixed contact stiffness. [242] While methods to account for the effects of tip dilation in topography have been well established, [243] methods to account for the finite tip size in the spatial variation of mechanical properties are less developed, although comparison to FEA models can be helpful for interpreting data [224].

Characterization methods for tip radius have already been discussed in Section 3.1.1, but do not cover how the size of the tip can influence applicable contact mechanics or the impact of changes to the tip shape that may occur during scanning due to wear or contamination. At small and large indentation depths, changes in the shape of an AFM tip can adversely affect the applicability of a contact mechanics model to an acquired force displacement curve. The following section aims to alert microscopists on how to iden-

tify and address the worst-case scenarios that may be observed as a result of non-ideal tip shape and contamination.

The careful measurement of the AFM probe radius (Section 2.1.1) is particularly important for contact mechanics models that rely on treating the indenter as a sphere (e.g. JKR). [164,244] While early work on quasi-static modes had suggested that a tip radius on the order of 100s nm is required for quantitative analysis, [164,245] more recent work has suggested it is possible to obtain reasonable, quantitative data with sharp AFM tips (R < 30 nm) as long as the tip is well characterized. [198,224,246,247] For nonideal tip geometries Sneddon's model can be used to fit a force displacement curve to a power law function (Eq. 5) for Hertzian contact as long as the tip shape is satisfactorily described by a smooth axisymmetric profile. If a tip cannot be easily described by one of the common Sneddon shapes (paraboloid, punch, cone, etc.), Segedin's model can be used instead which models the tip shape with an arbitrary polynomial series. [248] To be applicable, Segedin's model requires classical elasticity theory to hold at large indentation depths and detailed knowledge of the true tip shape. At small indentation depths, defects in the tip profile as a result of manufacturing or scanning induced wear [158] can mean that tip surface in contact with the sample is not well represented by a smooth, axisymmetric profile. [157] In almost all AFMs, the cantilever is orientated at an angle to the sample surface, which can induce lateral forces as the tip contacts the sample. [249]

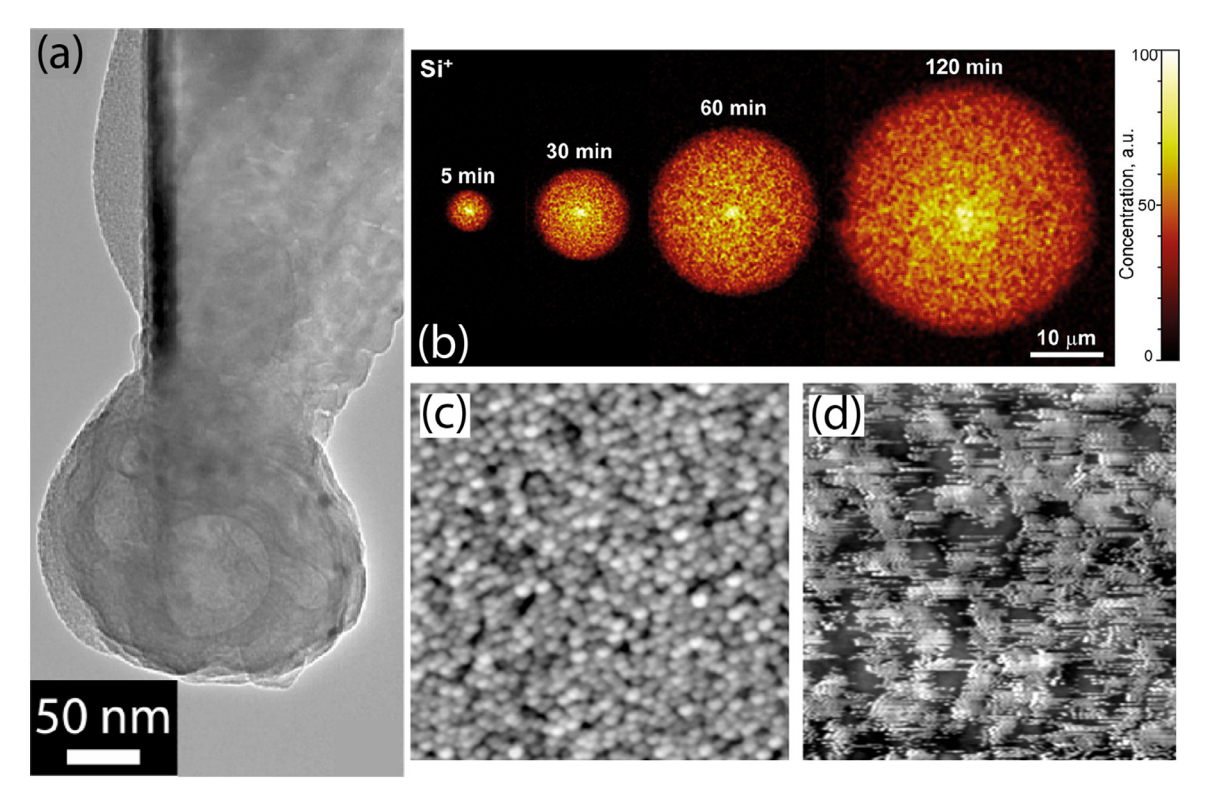


Fig. 13. (a) TEM image of organic tip contamination on an as-received commercial cantilever. [156], Copyright 2016. Adapted with permission from AIP Publishing LLC. (b)ToF SIMS map of contamination on the surface of a lead zirconate titanate thin film from an AFM tip held stationary on the surface. [251], Copyright 2018. Adapted with permission from the American Chemical Society. AM AFM height image of an Au film (c) before and (d) after tip contamination with liquid 1-decanethiol. [255], Copyright 2007. Reproduced with permission from AIP Publishing LLC.

Tip contamination results from foreign material adhering to the tip, either during scanning [250] or during storage with Fig. 13(ab) demonstrating a case of heavy tip contamination and the resulting modification to a sample surface that can result from such contamination. Deposition of low molecular weight PDMS or silicone oils from the storage boxes for commercial AFM probes has been shown as a common vector for contamination of the AFM cantilever. [251,252] Significant contamination of an AFM tip cantilever is observable as hysteresis in the force curve during the snap-on and lift-off during an indentation cycle [252] and can significantly distort acquired images (Fig. 13(c-d)). In comparison to hysteresis as a result of water capillary layers, the tip contamination can persist through changes in humidity and environment. Various cleaning procedures have been shown to reduced tip contamination by Silicone oil with differing levels of success. Options to remove contamination include: solvent washing, UV exposure, $O_2/Plasma$ and etching. [251,253,254]

While predominantly an issue for hard samples, AFM tips can experience wear during use on polymer materials, particularly on composites that contain hard, ceramic components. The commensurate evolution of tip shape during scanning can frustrate the consistent collection of data. The three main mechanisms of tip wear in AFM are: plastic deformation [256], attrition of atomic layers [165,168,256] and tip fracture [165]. To avoid tip fracture Chung et al. suggested that the loading rate during an engage should be less than 0.1 nN s⁻¹. [257] During contact mode scanning, Chung et al. found at least some wear of Si AFM tips is unavoidable on hard samples, with tip shape evolution observed for <10 nN loading due to surface layer oxidation of the tip. Vahdat et al. have suggested that a safe limit to prevent tip wear in AM AFM can be estimated from a universal parameter that considers the tip radius, cantilever properties and sample properties which can be ap-

plied to polymers as long as the contact mechanics are DMT or Hertzian. [218] The estimation of safe scan parameters does not consider side loading during scanning or the danger of tip fracture due to sudden topographical or compositional changes.

Surface tilt is a global rotation of the sample such that the global surface normal is not aligned with the vertical z-axis and can cause the AFM tip to contact the surface at an angle not anticipated by most contact mechanics. The most obvious means of eliminating surface tilt is to prepare and mount samples to be as flat as possible. However, for some *in situ* samples, particularly biological systems, avoiding changes in the orientation of the surface may be impossible. It should also be noted that due to the angle of the cantilever as it is mounted in most AFMs, flat samples are still angled relative to the tip.

The most common method to correct for tilt in topography images is to execute plane fitting or line-by-line flattening algorithms, which are built into most commercial and open-source AFM software packages. [86,258] These algorithms can induce nonphysical topography into an acquired image and, as such, care must be taken not to overfit acquired images. However, the impact of surface tilt is incorporated into mechanical property measurements during the experiment so typical levelling operations are not applicable for property measurements. For correction of surface tilt on mechanical property measurements, a recent solution from Heinze et al. [259] adapts models to account for the cantilever angle in contact resonance modes with respect to a flat surface in order to accommodate a tilted surface. The method is demonstrated using contact resonance measurements on a colloidal glass bead and a starch granule (Fig. 14) and corrects modulus measurements for a wide range of local surface slopes. While demonstrated for CR AFM, the method can be readily applied to other AFM modes.

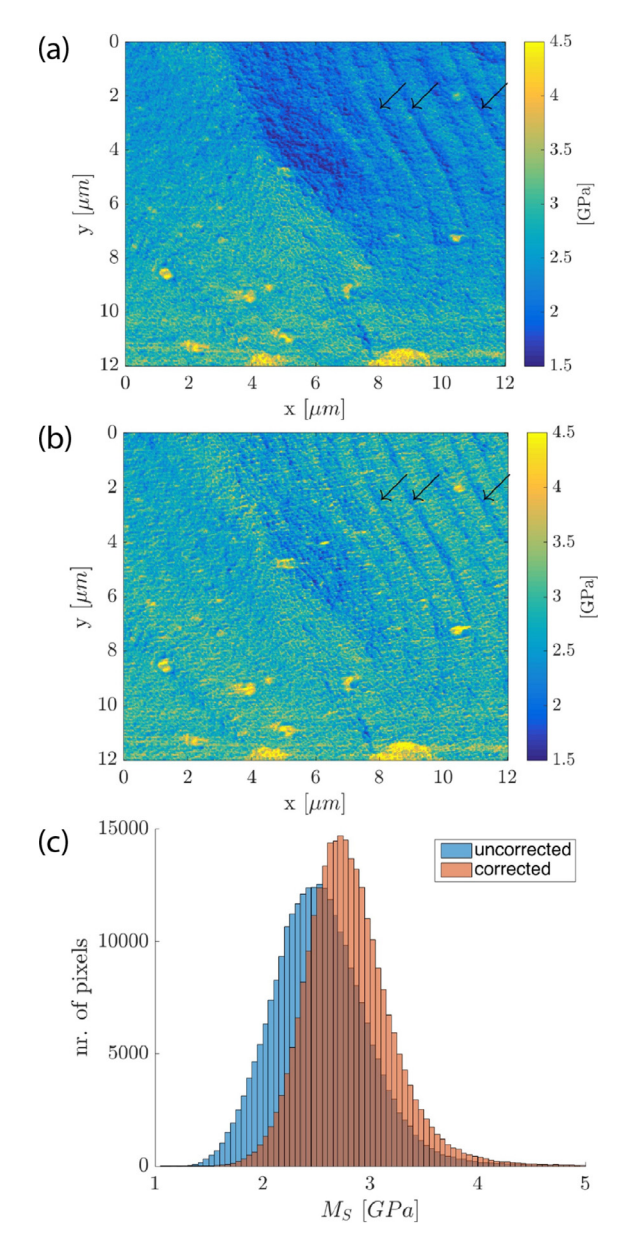


Fig. 14. Maps of the elastic modulus as measured by CR AFM on a starch granule (a) before and (b) after correction for surface tilt. (c) Histogram of the measured modulus before and after correction of the surface tilt. [260], Copyright 2018. Adapted with permission from Elsevier Science Ltd.

3.2.3. Sample heterogeneity

Accurate nanomechanical measurement of local property changes in polymer systems is a key goal of AFM studies, but care must be taken to separate changes in measured properties due to continuum or topographical effects from changes due to the underlying polymer chemistry and structure. [261] While, sample preparation for nanomechanical measurement should strive for surfaces with roughness that is at least an order of magnitude smaller than the tip radius used, in many cases this ideal is difficult to achieve. In multicomponent systems, surface preparation methods interact with the phases differently, often resulting in unavoidable topographical features. The influence of topography on the measured mechanical properties for dynamic and static modes is dependent on the local curvature of the surface and the number of contact asperities due to surface roughness. [157,262] Conversely, differences in surface deformation between components with differing mod-

uli for a given indentation force can result in false measurement of sample topography. Independent measurements of topography can be used to correct AFM measurements on samples [263,264] but are time consuming, so in-situ methods for interpreting mechanical property measurement in the context of changes in topography are preferred. In addition, prominent surface features and components may only extend a finite distance into the sample, in which case their response to indentation is, at least in part, defined by their structural compliance rather than material properties as they deflect into the surrounding material under load from the AFM tip. Meanwhile, components underneath the exposed surface may influence property measurements [265] without being immediately apparent in the height map (Fig. 10). Altogether, the surface topography of materials as it relates to mechanical measurement with AFM is distinctly three-dimensional and requires consideration for accurate interpretation of mechanical property

In multi-component systems the AFM tip will indent both components simultaneously as it rasters across phase boundaries on the surface. Fig. 15(a-d) illustrate the interface of a stiff fiber in a polymer matrix, where multiple contact points between the tip and the sample are possible. As a result, a 'dead zone' forms where often no quantitative information about the local properties can be gleaned due to the non-ideal contact. Changes in sample height [266] or modulus [224], can induce a variety of non-ideal tip-surface interactions leading to data interpretation difficulties. Fig. 15(e-f) demonstrates the convolution between the surface geometry and local stiffness with a sudden topography change in the height channel correlated to sudden changes in the stiffness channel. Without additional analysis, disentangling whether a sudden change in height causes a sudden change in stiffness due to the multiple contact points, or whether the sudden change in sample deformation has induced an artifact in the topography or some combination of two is near impossible. Additional data channels may help identify the extent of the dead zone which is dependent on both the relative stiffness of the indented components and tip geometry. For example, conductive AFM can be performed simultaneously with mechanical measurement [264] and the traces across the two interfaces can be compared (Fig. 15(c-d)). When the tip is close enough to a conductive fiber then a current between the sample surface and the tip is measured, enabling an independent confirmation of contact between the tip and the stiff fiber. Alternatively, the tip radius can be reduced to minimize the size of the dead zone, and some form of independent confirmation of interface location and the extent of the dead zone can be conducted through consideration of tip geometry and indentation depth. [224] In some circumstances, dead zones can be identified by examining force curves across the interface, where indentations that initially indent the soft phase before indenting a stiff, neighboring phase will show a distinct kink in the F- δ curve due to the increase in contact stiffness. [260]

When imaging a multi-component system where each component has contrasting moduli, the relative differences in deformation can produce a false topography. [105,267-271] If the sample deformation is known through accurate contact point determination for each component, then the deformation can be subtracted from the raw topography measurement to produce an improved estimate (Fig. 16) of the sample topography. Correcting height maps for deformation where possible is suggested prior to determining whether surface topography may be influencing mechanical measurements.

High local curvature or large changes in topography are also known to alter the measured phase across a sample in AM AFM. In order to determine whether phase contrast is the result of material properties or due to local surface features, a map of gaussian curvature can be calculated from the acquired topography maps.

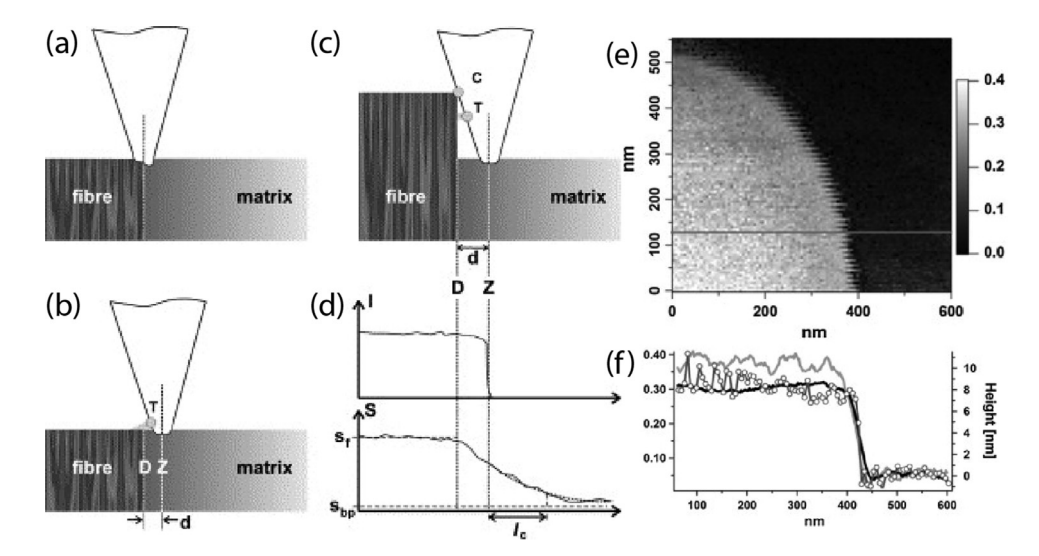


Fig. 15. (a) Contrast in moduli between the fiber and the matrix result in unsymmetrical indentation depth. (b) For conductive AFM, the tip will interact with the fiber when the distance is small enough for tunneling. (c) Step feature due to fiber protrusion means that the side of the probe will contact the fiber while the tip is indenting into the matrix (d) Resulting profiles of current, I and stiffness, S. The dead zone (D-Z) indicates the region where useful matrix information cannot be extracted due to tip fiber contact. [264], Copyright 1998. Adapted with permission from Elsevier Science Ltd. (e) Map of contact stiffness a polystyrene-polybutadiene interface from FV AFM shows the contrast in stiffness between the glassy and rubbery polymers. Distortion at the interface can be observed due to simultaneous tip contact across the two domains. (f) Trace of contact stiffness (grey line with dots), height (gray line), and normalized phase shift (black line) from AM AFM across the black line in (a). A clear correlation between all three traces in observed. [260], Copyright 2014. Adapted with permission from Elsevier Science Ltd.

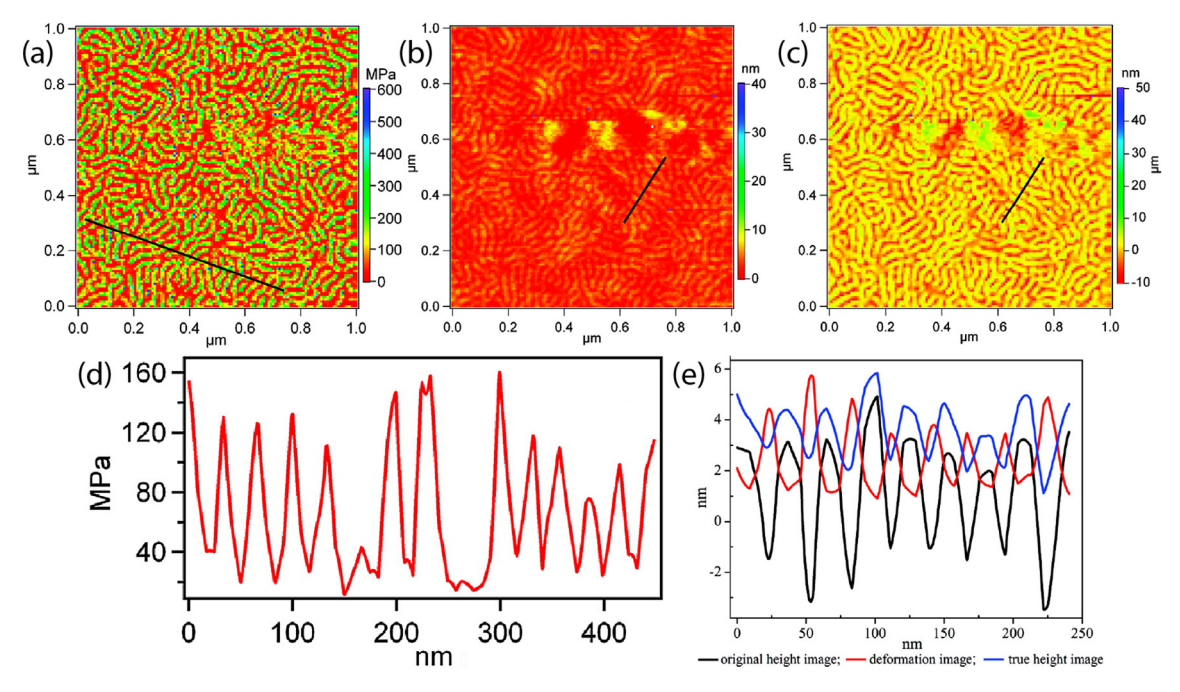


Fig. 16. AFM FV maps of (a) Youngs modulus, (b) original height, and (c) reconstructed height after correcting for sample deformation for a SEBS (poly(styrene-b-ethylene-co-butylene-b-styrene) triblock co-polymer. (d) Trace of Young's modulus along the black line in (a). (e) Traces of topography, deformation, and corrected topography acquired from along the trace indicated by the black line in (b) and (c). The corrected topography trace is calculated by subtracting the sample deformation from the original height profile. [268], Copyright 2010. Adapted with permission from the American Chemical Society.

Contrast in the calculated map of gaussian curvature can be compared to the phase contrast to check for correlations: any phase contrast as a result of material properties should not correlate to the contrast in the gaussian curvature. [272] For AM AFM, small feedback errors in the phase channel due to height changes can be corrected by comparing the relationship between the change in phase and amplitude near the amplitude setpoint and then subtracting the contribution to the phase map from the amplitude error. [87]

If an indented component has a finite volume and is surrounded by material either softer or stiffer than the indented phase, then the mechanical response of the embedded phase will be impacted by the compliance (Fig. 11(d)) of the surrounding material. Previous discussion on the substrate effect in Section 3.2.1 focuses on modelling the stress interaction effects for underlying, fixed substrates. But displacement of finite phases into the surrounding medium under indentation can be expected while scanning across multiphase systems. For example, in polymer

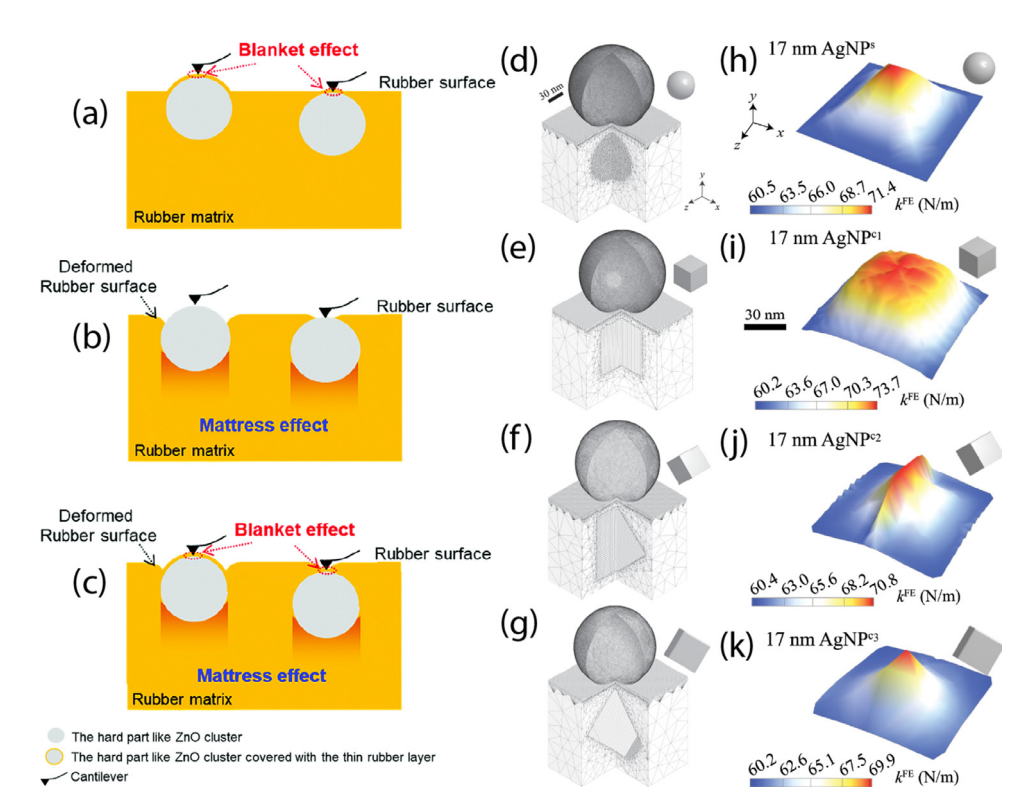


Fig. 17. Models for particles suspended in polymers for the specific example of Zinc Oxide (ZnO) embedded in rubber. (a) The blanket effect, where an embedded or protruding particle has a thin layer of bound rubber. (b) The mattress effect for supported and embedded particles where indentation on a particle causes deformation in the surrounding rubber, introducing structural compliance. (c) The combined blanket and mattress effect. [273], Copyright 2018. Reproduced with permission under CC BY-NC 3.0 – published by the Royal Society of Chemistry. FEA models of indentation over a (d) spherical, (e) cubic, (f) edge high cubic, and (g) vertex high cubic particles embedded 17 nm below the surface. The resulting maps of contact stiffness (k^{FE}) on and near the particles in FEA for the (h) spherical, (i) cubic, (j) edge-high cubic and (k) vertex high cubic particles reflect the underlying geometry of the embedded particle. [225], Copyright 2019. Adapted with permission from IOP Publishing Ltd.

nanocomposites, embedded, hard particles are softly suspended in the matrix (termed the 'mattress effect') and do not have fixed boundary conditions to constrain rigid body motion of the particle under a load from the AFM tip. (Fig. 17(b-c)). For deeper indentations, the mattress effect will reduce the measured modulus of the particle due to the compliance of the surrounding relatively soft matrix. The mattress effect can be minimized by reducing the applied force to the particle or working with larger particle sizes, if feasible. For indentations near particles, a common occurrence in AFM analysis on polymer nanocomposites – deflection and rotation of the particle – can occur due to the applied load from the tip. However, if the particle is approximately an order of magnitude larger than the tip contact radius then it can be approximated as a perfectly rigid substrate. [224]

Complicating the analysis is that particles may also have a layer of polymer (the 'blanket effect') over the surface of the particle (Fig. 17(a, c)), which increases the measured adhesion on the particle surface and reduces the measured modulus relative to expectations. [273,274] The 'blanket effect' may confound expectations for the measured snap-on adhesion and modulus as the thin layer of polymer will increase the adhesion and reduce the initial contact stiffness during indentation. Accounting for the blanket effect in protruding particles or indentation over shallow, embedded particles is more difficult and requires additional modelling and/or interpretation with FEA or semi-analytical equations. Subsurface features can be recognized by changes in the local modulus with increasing force setpoint but without corresponding change in adhesion or topography relative to a homogenous region. [226]

The highly complex geometry associated with indentation on embedded particles can make the application of contact mechanics models to indentation data difficult (Fig. 17(d-k)). FEA that models AFM indentation over and near embedded and suspended particles can be a useful aid for the interpretation of indentations on suspended particles and embedded inclusions, and development of empirical and semi-analytical relations have been developed to model the impact of varying permutations of inclusion geometry, material properties, and boundary conditions on indentation measurements. [225,275-280] A recent method for calculation and visualization of the quality of collected force curves on particles in cross-linked rubbers has been introduced by Ohashi and coworkers who use an 'R-factor' to evaluate the fit of the IKR and DMT models to experimental force curves in order to identify where indentations on a rubber composite compare well to theory [273].

When collecting AFM maps across the surface of a composite, the magnitude of the stress interaction effect (Section 3.2.1) will vary depending on the proximity of the tip to a neighboring component and indentation depth. Qu et al. [281] first applied this idea to AFM measurements on rubber nanocomposites to determine whether the measured bound layer could be explained purely by the substrate effect, and found that while the substrate effect contributed to an enhanced modulus, it was not sufficient to explain the measured bound layer. Collinson et al. [224] also demonstrated for rubber nanocomposites that AFM indentation into incompressible materials such as rubber, results in a stress interaction effect which can be empirically modelled as

$$\frac{E(x)}{E_{FF}(\delta)} = A \left(\frac{a(\delta)}{x}\right)^n + 1 \tag{46}$$

where E is the measured modulus at the distance from the substrate or particle x, E_{FF} is the far field modulus, A and n are fitting constants, and a is the contact radius. Eq. 46 is valid until the AFM tip begins to contact the substrate or particle directly. It was also found that the fitting constants A and n are relatively insensitive to the modulus of the indented or neighboring component as along as their modulus difference is at least 2 orders of magnitude, typical of most rubber nanocomposites. The stress interaction effect is best minimized by reducing the contact area during indentation, either through reducing tip radius or indentation depth. However, both options can introduce other experimental errors, which will be discussed later.

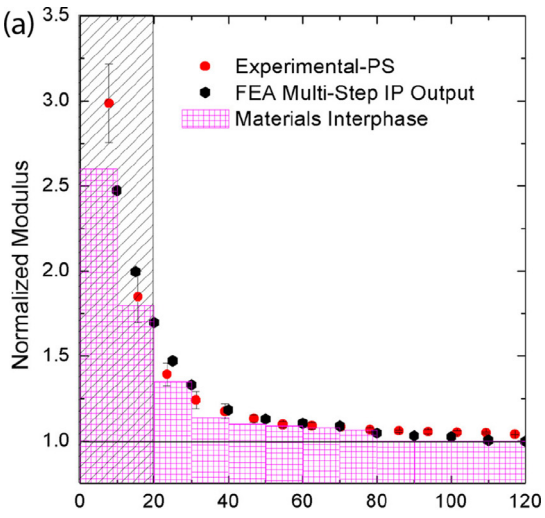
The analysis of the stress interaction effect and the interphase in Qu et al. can be taken a step further through quasi-static AFM indentation studies near model interfaces. By replicating an AFM experiment (configuration as in Fig. 11(c)) in FEA iteratively, a solution for the interphase modulus gradient (Section 1.2.1) can be obtained which will produce an effective modulus from the AFM matching the experimentally measured data (Fig. 18). This method of deconvoluting the substrate effect from local properties was first tested on SBR bonded to a Si substrate using thiolene click chemistry. [282] The process used to match the FEA model to the experimental measurements of stiffness is shown in Fig. 12(b-e). Zhang et al. used a similar method to estimate the interphase in a PS-Silica sample (Fig. 12(a)). [283] In both cases, the simulations are used to capture the purely geometric substrate effect, which then allows the inherent property value of the polymer near the substrate and its gradient to be determined quantitatively.

For any system that has significant property contrast, the substrate effect will influence any image or data point within several contact radii from a neighboring component or indentations on a sufficiently thin film. The extent of the substrate effect is contact radius dependent (Fig. 11(a)), so if possible, minimizing indentation depth is beneficial. When interpreting local gradients or trends with film thickness, comparisons should always be made to continuum predictions as the first step to establish if changes in properties are real or a result of changes in structural compliance within the probed volume.

3.2.4. Viscoelasticity and polymer dynamics

Contact mechanics that determine elastic modulus in polymers (Table 2) do not consider the transient response of the material. However, it is well known that the response of polymer to deformations are strain rate and temperature dependent [151] which means that the measurement of 'elastic' properties can vary depending on the strain rate induced by indentation and ambient conditions. Viscoelastic approaches to analysis of AFM data have already been provided in Sections 2.1.2 and 2.2.5. But if only elastic properties are desired, the presence of viscoelastic behavior during indentation will still require adjustment in the analysis of acquired AFM data. In addition to changes in modulus and relaxation time, the Poisson's ratio changes as the material transitions between glassy and rubbery regimes, and accounting for this change can be important to decrease error in conversion from reduced modulus to elastic modulus (Eq. 4). [10,61,213]

Three aspects of AFM indentation affect material viscoelasticity: probe radius (due to changes in strain rate and applied stress), drive frequency, and sample temperature. The dependence of strain rate on the tip radius can lead to changes in the viscoelastic behavior of the indented material between tips, even for constant loading rate and sample temperature. [284] However, the impact of the AFM tip on the sample surface can also induce additional, high frequency oscillations in the sample surface, complicating our understanding of the deformation frequencies experienced by the material during an indentation cycle. At a minimum, bulk viscoelas-



Distance from the Polymer-Substrate Interface (nm)

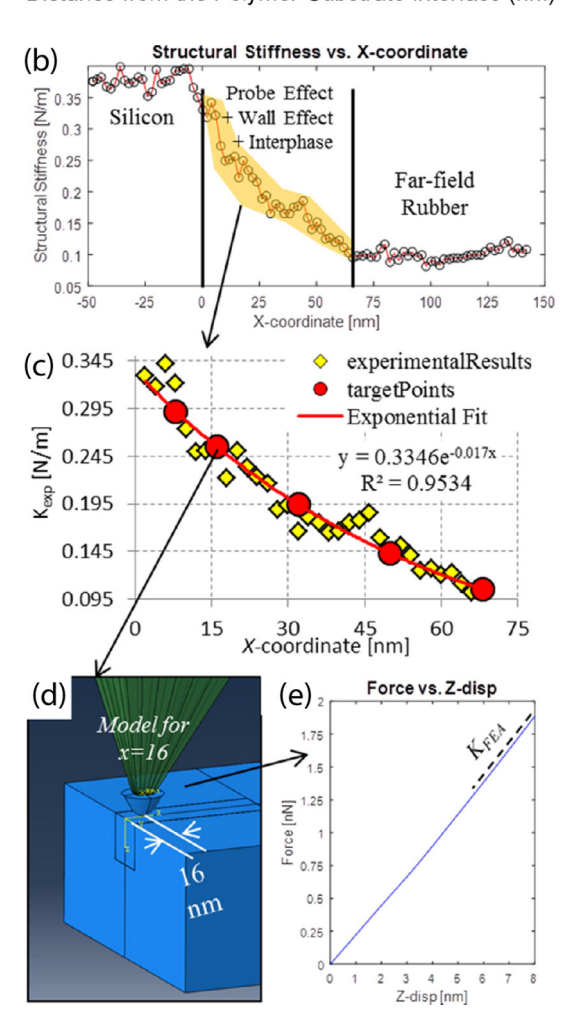


Fig. 18. (a) Agreement between PFM AFM data (red circles) near a PS-Silica interface and a FEA model (black circles) that includes modified local modulus (pink columns) due to the interphase due to silica-polymer interactions. [283], Copyright 2018. Reproduced with permission from the American Chemical Society. (b-e) Work flow for matching stiffness data collected across a covalently bonded rubber-Si interface (b) Experimental FV data showing stiffness gradient near the interface (c) Region of interest for an FEA model to reproduce the experimentally measured stiffness data (yellow diamonds at discrete points (red circles) (d) FEA model with the AFM tip at a specified indentation point with locally modified input moduli in the FEA model (e) resulting force-displacement curve from the FEA model. [282], Copyright 2016. Reproduced with permission from the American Chemical Society.

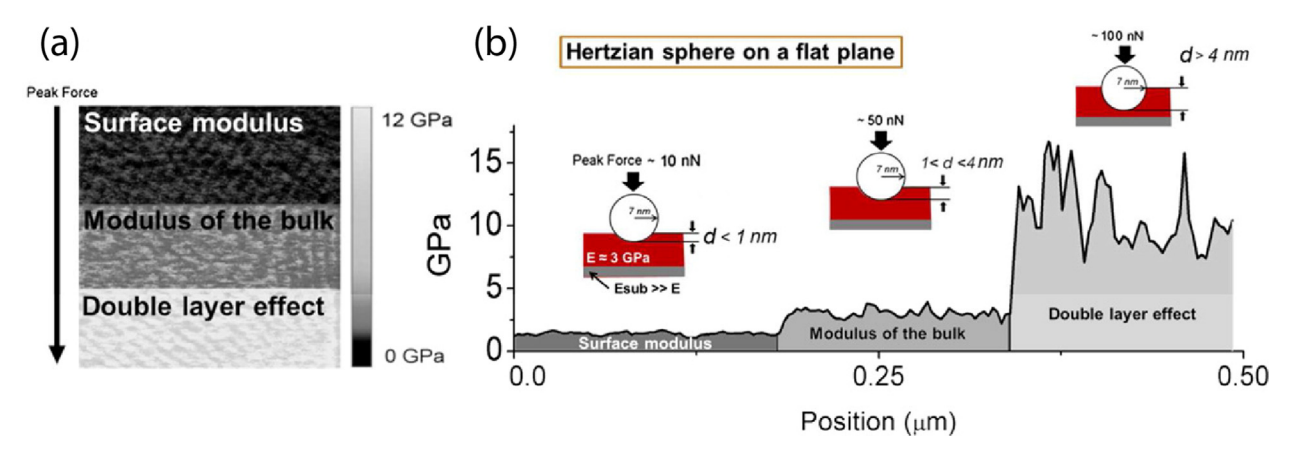


Fig. 19. (a) Increase in measured DMT modulus with applied force on a PS-PMMA blend (b) The decrease in modulus at small indentation depths can be attributed to a mobile surface layer. Intermediate indentation depths predominantly sample the bulk film properties. Large indentations cause plastic deformation and begin to interact the underlying substrate. [292], Copyright 2015. Reproduced with permission from the American Chemical Society.

tic properties of the material of interest acquired using equipment such as DMA or nanoindentation must be shifted using time-temperature superposition for comparison to results at the analysis frequency in AFM, noting that free surface effects may influence small AFM indentations more than nanoindentation measurements. [61,213]

Special consideration should be given to contact resonance techniques when evaluating soft, viscoelastic materials with large damping present at the MHz analysis frequencies common for contact resonance (Table 1). In these cases, the highly damped materials reduce the contact resonance spectra to the point that the response is a convolution of the piezo drive transfer function and the actual contact resonance of the tip-sample system. [31] As a result, contact resonance techniques remain limited in addressing soft compliant samples.

In both quasi-static and dynamic intermittent contact modes determination of the energy dissipated from viscoelastic effects requires parsing the viscoelastic material response from other causes of dissipation in the AFM measurement such as the work of adhesion. A rudimentary method to differentiate between the contributions to the dissipated energy from viscoelasticity and adhesion was demonstrated by Wang *et al.* by collecting static force curves on a SEBS triblock copolymer and assuming that the JKR model is able to fully account for the work of adhesion. The remaining dissipated energy between the fitted JKR curve and the experimental force curve was attributed to energy dissipated due to material viscoelasticity. [63] In tapping mode AM AFM, analysis of the change in dissipated energy with amplitude can help single out the various dissipative processes acting on the vibrating cantilever, including viscoelasticity. [104]

For shallow indentations with sharp tips, interpreting measured elasticity and dynamics becomes complicated relative to bulk measurements. It has been well-established in films that polymers experience free surface effects, increasing polymer mobility and reducing the barrier to molecular motion within a finite distance (1-20 nm) from the surface above and below $T_{\rm g}$. [285-290] Therefore, for shallow AFM indentations and small tip radii (Fig. 19), the AFM tip may predominantly sample a surface layer rather than the bulk polymer. [291-293] The reduction of the activation energy for primary (α) and secondary (β) relaxations at the free surface has been observed for multiple polymers using frictional force microscopy, [294-298] with the reduction in activation energy further exacerbated by the high stresses under sharp tips. [299] The decrease in activation energy for molecular motion at

the free surface may lead to conflict between nanoscale AFM indentation and bulk characterizations of viscoelasticity and dissipation at the same analysis frequency and temperature. Different polymers may also experience different susceptibilities to the free surface effect. [287,300-302] Additionally, as has been considered by Solares, [66] the act of indentation into the surface perturbs the shape and curvature of the surface itself, with its own energy cost which can contribute to the response of the material to indentation. Altogether, comparing small AFM indentations with bulk properties should not just consider the differences in analysis frequencies, but also any possible changes in the viscoelastic nature of the polymer surface.

While there have been suggestions that nanoindentation can induce a stiffening of the surface layer in contact with the tip [303], there has been additional evidence that such results may be artifacts due to uncertainty in contact point determination and adhesion at small indentation depths. [164,304] Shallow indentation depths are preferable for high resolution, but indentation measurements that can be compared to bulk or nanoindentation data need to probe a sufficient volume of bulk polymer such that contributions from a mobile surface layer are rendered insignificant. An often-used calibration method of tip radius for AFM studies is to compare the measured value to a bulk or nanoindentation measured modulus and adjust the tip radius until the moduli match. For polymers however, it is possible that small AFM indentations will measure a softer modulus and higher dissipation due to free surface effects. [302] A modulus as measured by AFM on glassy polymers that is smaller than what is obtained from nanoindentation or DMA, after accounting for differences in analysis frequency, should not be dismissed out of hand.

Glassybpolymer systems such as PS or PMMA are typically considered homogenous, but there is a significant body of work that suggests that elastic and dynamic heterogeneity exists in all glass formers, including polymers, above and below the glass transition temperature. [43,149,305,306] Depending on the polymer, the heterogeneity has a characteristic length scale between 1 – 5 nm, [307] relevant for high resolution AFM indentation, where contact radii are on a similar length scale. The dynamic heterogeneity at the free surface has been observed directly in AFM studies, [308-310] and the presence of these inhomogeneities should be considered when analyzing high resolution AFM data on glassy polymers as they may result in a natural variance in the measured properties across a surface that is averaged out by larger indentations.

3.2.5. Plasticity

A significant concern for sensitive property measurements with sharp AFM tips is the potential impact of plasticity. The high stress under AFM tips means that plasticity is always a concern, but there is evidence that the yield strength of glassy polymers are subject to indentation size [311] and strain rate [312] effects, and only begin yielding on the length scale of an AFM indentation at much larger stresses than what is expected from bulk yield strength. [279,313] For example, a simple continuum prediction of the applied force to exceed the typical yield strength of a typical thermoplastic indented by a stiff, R = 30 nm probe in Hertz contact is ≈ 0.1 nN, [314] but permanent deformation is not observed on glassy polymers utilizing sharp probe tips for forces up to 50-100nN. [246,247,283,292,315]

Consideration of the molecular mechanism for plastic deformation in polymers may help explain the limited permanent deformation under typical loads in AFM experiments. A deformation behavior, originally developed for metallic glasses, termed shear transformation zones (STZs), has been proposed as the yielding mechanism for glassy polymers [316] and is the cooperative rearrangement of polymer chains in a finite volume under shear. [317-319] Recent MD simulations on coarse-grained polycarbonate [315] finds agreement with the large yield strength found for experimental indentation into polymers. For a sufficiently sharp tip, although the peak stress is large, it may be concentrated in a small volume that does not reach the critical size to induce permanent deformation. [318] Indirect measurements suggest that the STZs in polymers have an approximate volume of 100 to 500 nm³, [317,320] comparable to the length scale of dynamic and elastic heterogeneity in polymers and larger than the highly stressed zone under a sharp tip. [307] MD experiments of plastic yielding under tension suggest that the yield is initiated at highly mobile dynamic heterogeneities in the polymer, supporting this observation. [321] Whether yield in polymers is due to STZs is not a fully resolved question, [311,322,323] but may provide a mechanism to explain the apparent capability of polymers to deform under sharp AFM indentations without permanent damage far beyond what is classically predicted from bulk properties.

However, indentation with large forces can still permanently deform a sample [31,312] with the onset of plasticity also depending on the loading rate. [313] Recognizing plasticity in force curves acquired from viscoelastic materials can be challenging, as force curve hysteresis can be attributed to viscoelasticity, the work of adhesion or plasticity. To determine if the surface is permanently deformed after conducting an AFM experiment, a subsequent height map that includes the indented area and the surrounding material can be acquired to determine if there is any residual deformation in the scanned area. To ensure minimal forces are applied during the subsequent scan, AM AFM is preferred for imaging. AM AFM scan parameters should be such that intermittent contact is made with minimal surface deformation so that the true sample surface is profiled.

3.2.6. Tip sample interactions

Adhesive interactions between the tip and the sample can change depending on the tip geometry and surface functionalization, the sample surface chemistry and stiffness and the operating environment. Long and short range molecular forces, capillary forces in air, and solvation forces as well as double-layer forces in liquid can all influence the tip during an indentation and have consequences not just for the contact mechanics, but also the AFM operation and choice of scan parameters. [142]

While adhesion generally is easily accounted for in static modes through DMT or JKR contact mechanics (Table 2), accounting for adhesion in dynamic modes is more difficult as only Hertzian contact mechanics are commonly available to describe the tip-sample

interaction. The error due to ignoring adhesive effects is demonstrated when examining DART and BE CR on polymer blends. While the loss modulus values acquired by BE compare better to DMA than DART, due to the use of the complete contact resonance spectra, scans across blends with a rubber component show higher modulus on BIMS (rubber) than PP (thermoplastic), attributable to adhesive effects. [31] Adhesion is also partly responsible for the overestimation of loss tangent as measured by dynamic modes. [18] The adhesion of polymers typically increases with temperature due to high surface mobility, [139] which can convolute interpretation of VE property measurements across different temperatures.

In ambient conditions, a monolayer of water approximately several nm thick exists on all hydrophilic surfaces. [324,325] The monolayer can strongly influence the measured adhesion force in AFM depending on the hydrophilicity of the tip and sample. [51,325] [326] The formation and rupture of capillary bridges between an AFM tip and the monolayer on a sample surface can occur at different tip-sample separation distances and result in force curve hysteresis, affecting the measurement of adhesive forces [327] and topography. [328] For hydrophilic samples, the size of the monolayer can increase as the relative humidity increases, increasing the required force to overcome the capillary effect, leading to day to day variation in uncontrolled environments. [329] One option to remove adhesive effects from a water monolayer is to simply immerse the tip and sample in a liquid environment. [10,19] Alternatively, a completely dry environment (operating in vacuum or under N₂) can also be used to minimize the monolayer.

For dynamic modes that are not able to include adhesive interaction in contact mechanics, the best option is to simply remove the adhesion due to the water monolayer through operating in a completely dry environment or in fluid. For dynamic and quasistatic modes, removing adhesion allows for more sensitive imaging as less force is needed to overcome adhesive effects and simplifies analysis.

3.2.7. Recommendations and best practice

Interpreting AFM data on polymers, which requires consideration of material behavior, tip-sample interactions and the presence of multiple components is a fraught and complicated affair. Table 8 provides a summary of our recommendations for identifying nanomechanical phenomena during AFM operation on polymers and possible means to address them. These are general suggestions, and can form the basis of more detailed, system specific lists of best practices and methods developed by an AFM user for their samples and operation mode.

3.3. Conclusions

Nanomechanical properties measured by AFM with sharp tips have often been compared to instrumented nanoindentation, despite the several orders of magnitude difference in the length scale of the two techniques. While there is a significant body of work in the measurement and understanding of mechanical phenomena on the 100s of nm length scale from nanoindentation measurements on polymers, a better understanding of nanoscale phenomena such as free surface effects is still required for AFM indentations where the indentation depth is on the order of 1-20 nm. Alternative methods for measuring the local properties of the free surface, such as particle embedding, [286] would be beneficial for validating the accuracy of nanomechanical AFM at small indentation depths. In a similar vein, continued development of the quantitative measurement of polymer viscoelasticity with dynamic and quasi-static AFM methods that fully incorporates surface level phenomena and heterogeneity seems to be the necessary next step to better interpret data acquired near the surface of polymers.

Table 8

Summary table of mechanical phenomena that can arise while conducting AFM on polymers, practical methods to identify a particular behaviour and assorted options to address the identified issue if desired. While some of the identified issues are occasionally desirable for some studies, it can be valuable to remove them to simplify data analysis and interpretation. Adverse effects on AFM measurements can either be eliminated, minimized, or controlled for. The preference is to eliminate or minimize identified issues, and when not possible to control for the issue in post-processing and analysis. Supporting citations and reasoning is provided in the sections noted.

Category (Section)	Issue	Identification (QS – quasi-static, IC – intermittent contact AFM, CR – contact resonance)	Solution (Eliminate, Minimize or Control)
Stress Interaction Effects (3.2.1)	Underlying substrate	QS, IC, CR – Artificially high material modulus that increases with indentation depth after accounting for non-elastic material deformation	Eliminate – Increase film thickness to preferably >10a. A film thickness of 10a is not always sufficient. Minimize – Reduce tip radius or indentation depth. Control – Use appropriate modified contact model Control – Use FEA to estimate substrate effect
	Neighboring body	QS, IC, CR – Artificially high material modulus that increases with indentation depth near a stiff body without direct tip contact	Minimize – Reduce tip radius or indentation depth. Control - Use appropriate modified contact model. Control – Use FEA to estimate stress interaction effect
Tip Effects (3.2.2)	Wear	QS – Gradual increase in measured adhesion and/or decrease in measured modulus while scanning. Increase in measured tip radius from SEM or blind estimation IC – Larger free amplitude or smaller set-point ratio required to reach the repulsive regime after scanning	Eliminate – Replace AFM cantilever Minimize – Reduce force applied to cantilever tip Control – Use appropriate tip radius for analysis
	Fracture	QS, IC, CR - Sudden increase in measured adhesion and/or decrease in measured modulus while scanning. Increase in measured tip radius from SEM or blind estimation	Eliminate – Replace AFM cantilever Minimize – Reduce speed/ applied force during engage and scanning
	Contamination	QS – Hysteresis in snap-on and snap-off points that cannot be removed by operating in liquid or a dry environment. Pull-off <i>F</i> -δ trace may show evidence of chain pulling. IC – Softer than expected modulus measurements in AM-FM and unstable surface tracking. Larger free amplitude or smaller set-point ratio required to reach the repulsive regime after scanning.	Minimize – Store samples and AFM cantilevers in dry, sealed environment. Minimize – Irradiate AFM tips with UV/Ozone or $\rm O_2/Plasma$
	Surface tilt	QS, IC, CR – A global gradient in the height channel QS, CR – Hysteresis in the trace and retrace channels for the height and stiffness.	Eliminate – Remount sample in AFM Control – Use a modified contact mechanics model that accounts for surface tilt
Topography (3.2.3)	Local surface roughness and curvature	QS, IC, CR – After correction for surface deformation, large local variations in the height channel QS, IC, CR – Significant local variation in the modulated parameter (e.g. amplitude set-point for AM AFM) above the baseline noise	Minimize – Examine surface preparation methods Minimize – Increase contact area to average measurement over a larger area Minimize – Slow scan speed to improve surface tracking. Minimize – Choose cantilever with higher bandwidth
	Surface deformation	QS, IC, CR – Track surface feature height and size as a function of applied force.	Minimize – Reduce applied force Control – Correct height map using measured deformation
Embedded Phases/Multicomponent Systems (3.2.3)	Interfacial zones	QS – A sudden change in contact stiffness during indentation as a result of the tip indenting on one phase followed by another. QS, IC, CR – Local hysteresis in the trace and retrace of the mechanical properties across the interface.	Minimize – Reduce indentation depth Control – Use independent data channels to estimate location of the interface Control – Estimate dead zone from tip shape and indentation depth.
	Embedded features	QS, IC, CR – A local change in contact stiffness that develops with applied force and is not associated with any change in the adhesion and/or height channel after controlling for expected material deformation behavior.	Eliminate – Replicate in situ system with a model system with a simplified, well-defined geometry Minimize – Reduce applied force Control - Incorporate FEA and/or analytical models to correct measurements for embedded component and matrix properties

(continued on next page)

Table 8 (continued)

Category (Section)	Issue	Identification (QS – quasi-static, IC – intermittent contact AFM, CR – contact resonance)	Solution (Eliminate, Minimize or Control)
Material Behavior (3.2.3-4, 2.1.3)	Viscoelasticity	QS - Hysteresis in force curve during contact CR - Increase in Q IC - High E_{dis} after controlling for dissipative tip-sample interactions.	Minimize – Change analysis frequency, tip radius or operating temperature Control – Incorporate viscoelasticity into analysis
	Plasticity	QS, CR, IC - Change in surface height after scanning	Minimize – Reduce applied force. Minimize – Reduce stressed volume Minimize – Increase indentation rate
	Hyper elasticity	QS - Increase in measured modulus with indentation depth	Minimize – Reduce indentation depth Control – Use appropriate contact model
Tip-Sample Interactions (3.2.6)	Long-range electrostatics	IC - Reduction in amplitude when approaching the surface in AM AFM as well as a change in the static deflection signal QS - Change in deflection as tip moves towards the surface.	Eliminate - Neutralize static charge on sample surface. Operate in humid or liquid environment. Minimize - Retune cantilever close to the surface $({\approx}500~\text{nm})$
	Water monolayer	Hysteresis in the snap-on/snap-off points of a force curve	Eliminate - Operate in liquid environment Minimize - Operate under N_2 or vacuum.
	Van der Waals adhesion	QS, IC, CR – Conservative adhesive force	Control – Use appropriate adhesive contact model
	Squeeze-film damping	QS, IC, CR – Squeeze-film damping will always be present except in high vacuum. IC – A reduction in amplitude and an increase in phase will be observed on approach to the surface	Minimize – Retune cantilever close to the surface (≈500 nm) Minimize – For samples with large height variation, perform a nap pass at constant height above the sample surface. Control – Incorporate squeeze-film damping into models of tip-sample interactions

For systems with multiple components, readily applicable methods for interpretation of indentations near interfaces and corrections for structural and geometric effects to remove stress interaction effects can help to insure that AFM measurements of property gradients can be attributed to structural or chemical changes in the underlying polymer and not continuum scale effects. Further development in this area will help comparison of high-resolution mechanical property measurements to complementary spectroscopy and simulation techniques.

As a practical matter, the contamination of sharp AFM tips and the variability in tip radius, particularly as received from manufacturers is an issue for ensuring repeatability and accuracy for sensitive methods. Reliable methods for cleaning and storage of AFM tips to remove and prevent contamination that can be standardized across the AFM community would be a useful step towards achieving consistent results with AFM on soft materials.

There are several future avenues to reduce the impact of nonideal sample surface preparation on AFM measurement. The development of corrective contact models that can consider global tilt would be beneficial but difficult to apply readily. Samples that have components with different contact mechanics would be aided by robust contact point determination that covers JKR and DMT behavior. As the choice of cantilever stiffness is generally set by the material to be imaged, there is limited ability to alter scanning behavior through cantilever choice. We can speculate on possible improving scanning with AFM mechanical property measurements. For example, direct drive of the cantilever in PFM can remove the limitations in scan speed from the z-piezo for faster scanning. Another option may be to develop a 'topographical pass' that is conducted before the property acquisition scan in order to optimize the scan parameters for property measurement and adjustment of the cantilever height is based on the collected data from the 'topographical pass' to optimize the feedback loop actively controlling the z position of the cantilever during data collection.

4. Application of AFM Modes to Nanoscale Property Mapping on Polymers

In this section, we summarize the application of AFM modes on soft, heterogenous materials, focusing on the best approaches to extract small-scale elastic and viscoelastic mechanical property gradients. These measurements are especially insightful for understanding the fundamental physics of "interphase" polymer as mentioned earlier (Section 1.2.1), as well as in characterizing important regions in applications and systems of immense technical interest. While both AFM indentation measurements with large tip radius and nano-indentation can provide accurate mechanical properties for homogeneous materials, high resolution (*i.e.*, <10 nm per pixel) mechanical property mapping requires implementation of AFM methods such as those described in Section 2 to probe nanoscale domains and extract property gradients in heterogeneous materials.

Accurate measurement of the gradient in polymer properties near interfaces in polymer nanocomposites (PNCs) and other similarly nanostructured systems is critical for understanding the bulk mechanical response and the underlying mechanisms that lead to gradients in polymer properties near interfaces, or the polymer 'interphase'. While the length-scale of the interphase varies depending on the measured property due to the different underlying physics probed, [274,283,330-333] here we focus specifically on changes in elastic and viscoelastic properties. Interpretation of elastic and viscoelastic property measurements requires assessment of the potential mechanical artifacts, and the ability to reliably resolve gradients resulting from changes in polymer properties rather than the substrate effect (Section 3.2.1) or contact between the tip and the substrate (Section 3.2.2). While AFM in-

dentation has been implemented to investigate interfaces in some complex, heterogeneous polymer composite systems, the complexity in AFM analysis of composites has led to the introduction of model nanocomposites as simplified systems to probe interfaces at the nanoscale, with lateral or transverse scanning across a single, well defined interface (Fig. 11(b-c)) allowing for more straightforward quantification of property gradients that may be present. [282,283,332,333] This section provides examples of how the AFM modes outlined in Section 2 can be applied to the study of nanoscale mechanical property mapping, the current limitations of AFM for this purpose and some recommendations for future research directions.

4.1. Quasi-static AFM

4.1.1. Introduction

Application of quasi-static techniques such as FV and PFM to polymers is relatively straight-forward and as such has seen consistent use in the nanoscale property mapping of polymers. The applicability of a wide range of contact mechanics models to quasistatic indentations and direct measurement of the tip-sample interaction force as a function of indentation depth permits detailed study of local mechanical properties in complex systems and separation of the contributions from adhesion, viscoelasticity and morphological effects. The application of PFM AFM to in situ polymer composites is more prevalent than FV due to faster data acquisition, although the impact of structural effects on AFM measurements are not always considered. [334-338] Predominantly elastic analysis of collected force curves has been reported in the literature, and while viscoelastic analysis methods that have been demonstrated on biological specimens [50] and polymers [10,66,153] show promise, high resolution viscoelastic property maps on soft materials are still limited. [11] The force sensitivity of quasi-static indentation is low compared with dynamic modes, although averaging measurements over an area or multiple scans can help alleviate this issue.

4.1.2. Use cases

FV AFM has been applied extensively to the measurement of polymer properties, but its long acquisition time has limited its use in studies require repeated, high resolution, image acquisition of the same surface over time or repeated measurements on a variety of samples. The benefit of the shorter image acquisition time of PFM compared to FV has been leveraged in several studies that examine the development of the interphase modulus during aging experiments of fiber composites [339-343] and tracking of the interface broadening (Fig. 20(a)) due to transport phenomena. [344,345]

FV AFM measurements on a natural rubber-CNT composite demonstrate the sensitivity to measuring changes in the F- δ curves that can be observed in the matrix, interphase regions, and on the CNTs. [346] PFM was used to map the dispersion of CNTs in PLA/PCL blends, where the detection of a weak interphase was attributed to weak polymer-particle interactions. [347] PFM AFM was also used to map the dispersion of PS grafted MWCNT, although analysis of any interphase layer was not included. [348] A temperature dependence study of the interphase with both FV and PFM AFM techniques measured a 30 nm interphase at room temperature that increased to \sim 65 nm just below $T_{\rm g}$ for a PEMA-PiBMA copolymer near a hydrophobized silica particle. [349] PFM AFM (Fig. 20(b)) was used to complete the processing-structure property loop for PBAT/PLA blends compatibilized with phosphoniumbased ionic liquids, with the ionic liquids being able to compatibilize the PLA and PBAT, thus improving their miscibility, leading to an increased interphase layer width between the two polymers as measured by PFM and improved macroscopic strain-tofailure. [350] The sensitivity and nanomechanical property resolution of PFM is demonstrated in Fig. 20(c-d), where PFM successfully resolves the impact of sequential infiltration synthesis (SIS) on the measured modulus of a PS-b-PMMA copolymer and the local changes in SBR modulus near a carbon black particle. The ~30 nm PS and PMMA domains were resolved in both the topography and modulus channels and the increase in modulus of the PMMA with successive cycles of SIS was clearly observed. [351]

Compared to dynamic modes, the lower signal to noise ratio of quasi-static modes has led to a series of studies that are designed such that collected data can be averaged to reduce the impact of noise. The efficacy of this statistical analysis has been successfully demonstrated in 'model samples' mimicking the complex interfaces in in situ composites or blends using a single, one-dimensional polymer-substrate interface that can be repeatedly scanned. For example, a study by Cheng et al. examined the interface between a stiff substrate and a PMMA film with PFM, where an interphase propagating ~100 nm away from the substrate into the bulk of the film could not be accounted for by substrate effects in complementary FEA. [333] Top-down indentations on supported homogenous films are also a useful means to average collected data for a single film thickness. Repeated measurements on films of varying thickness related polymer susceptibility to nanoconfinement with their high frequency chain stiffness. [352-354] FV modulus measurements of PVAc thin films above and below T_g demonstrated that the contribution from the substrate to the measured modulus is more pronounced in soft, rubbery films relative to glassy films of the same thickness. [240]

The development of model samples has also allowed researchers to more easily correlate AFM measurements to complementary experimental methods to aid in the interpretation of nanomechanical data. PFM AFM measurements of the local modulus across a silica capped PS thin film found a ~5% modulus enhancement in the center of a 266 nm film, in agreement with fluorescence measurements Fig. 21(a) showing increased molecular stiffness in the polymer layer on the same samples. [332] and in support of previous findings on the interphase between glassy polymers and a substrate. [283,333] Another study used the depth sensitive nature of PFM to resolve subsurface features that correlate to chemical information from scanning near field optical microscopy (Fig. 21(b)) in a PS-b-PtBuA thin film. [355] Recent work using combined PFM and tip enhanced Raman spectroscopy Fig. 21(c) demonstrate that the change in modulus at the interface between embedded PS nanoparticles and the surrounding resin is correlated to local infiltration of the resin into the PS at the interface. [356] Comparison of the gradient in modulus as measured by FV indentations across the junction between two thiolene hydrogels of different crosslink density to confocal microscopy measurements of the diffusion across the interface of fluorophores (Fig. 21(d)) demonstrated that changes in mechanical properties are not always directly associated with chemical changes with the measured gradient in mechanical properties spanning a shorter length than that observed from transport measurements. [357]

The combination of the direct F- δ curve acquisition and the development of simple model samples has allowed for the development of FEA models that can be iterated and compared to experimental data. [358] FV AFM was used by Brune $et\ al.$ [282] to create a profile of stiffness across the interface of a model silicon / styrene butadiene rubber interface coupled using thiol-ene click chemistry. By iterating the length and properties of the interphase layers in a FEA model such that simulated indentations produced a similar response profile to the experimental FV data an estimate of the bound layer extent and modulus could be determined. Comparison of PFM AFM measurements to FEA models of the AFM indentation across a PS-silica interface required the inclusion of a ~60 nm exponentially decaying interphase profile

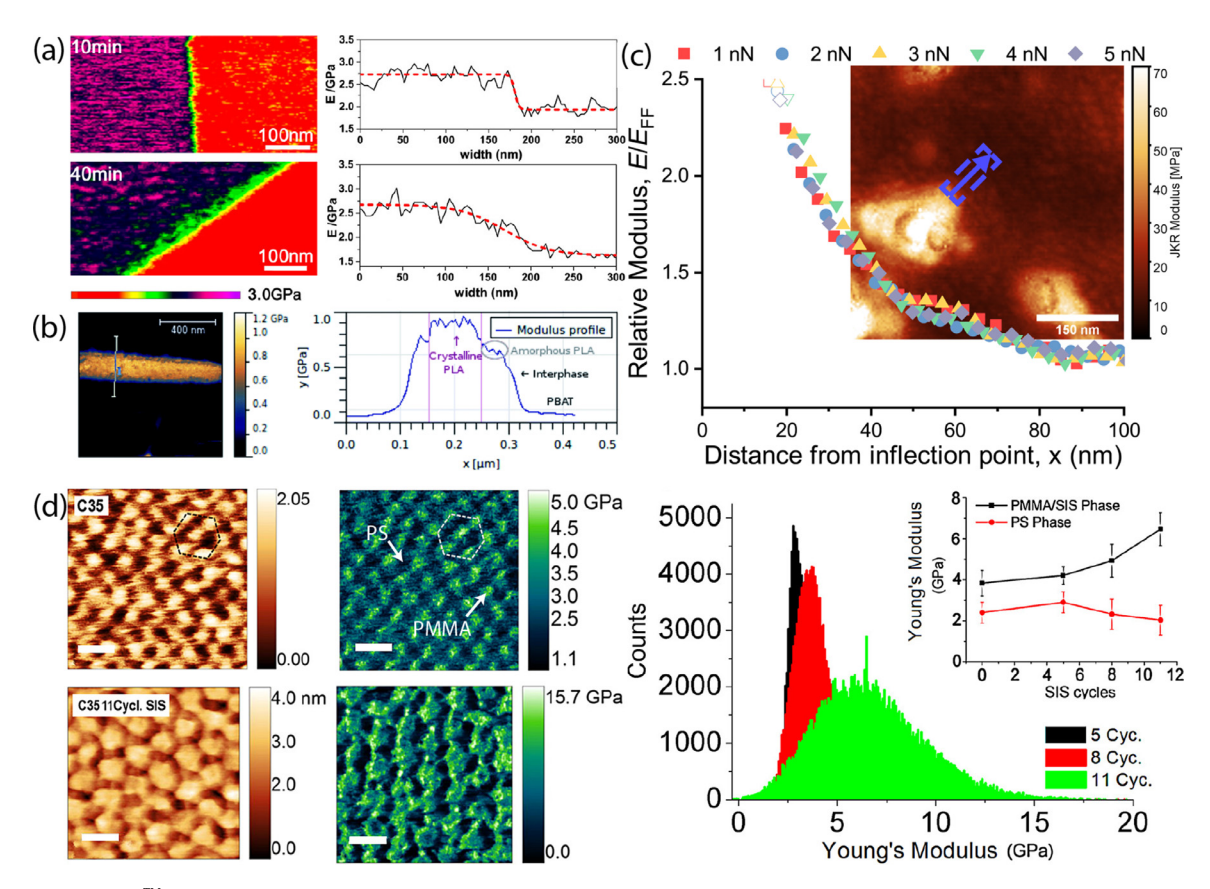


Fig. 20. (a) PeakForce QNMTM modulus maps and associated line scans across the interface between two epoxy phases 10 min and 40 min after mixing. The width of transition is observed to broaden over time due to chemical exchange mechanisms across the interface. [344], Copyright 2018. Adapted with permission from the American Chemical Society. (b) DMT modulus map collected with PeakForce QNMTM of a poly(butylene-adipate-co-terephthalate)/poly(lactic acid) (PBAT/PLA) blend compatibilized with an ionic liquid, bis-2,4,4-(trimethylpentyl)phosphinate. The profile on the right is collected from the line indicated in the map an clearly features hard crystalline and soft amorphous domains in the PLA as well as an interphase between the PLA and the PBAT due to improved miscibility between the phases owing to the presence of the ionic liquid. [350], Copyright 2016. Reproduced with permission from the Royal Society of Chemistry. (c) Normalized JKR modulus profiles across an in situ N121 carbon black-styrene butadiene rubber interface at multiple force setpoints. The consistent profiles at the setpoints probed suggest that the ~60 nm measured gradient in modulus is the result of a bound layer and not structural effects. [224], Copyright 2019. Adapted with permission from the American Chemical Society. (d) Topography and DMT modulus maps of a PS-b-PMMA thin film before and after being subjected to 11 cycles of sequential infiltration synthesis (SIS) to deposit Al₂O₃ on the surface of the PMMA pillars. Scale bars represent 50 nm. The bottom left histogram represents the modulus distribution before SIS and the inset is the hexagonal cell of PS pillars indicated in the maps of the pristine film. The bottom right histogram is the change in modulus of the PMMA cylinders with SIS cycles with the inset showing the diverging modulus measured on the PMMA and PS phases. [351], Copyright 2017. Adapted with permission from the American Chemical Society.

to agree with collected modulus data. [283] Accounting for structural effects on quasi-static measurements in in situ composites has been predominantly conducted by measuring the structural compliance during indentation and quantifying the impact on the calculated modulus. [223] Recent work by Collinson *et al.* [224] explicitly considers the impact of structural effects on measurements of the bound layer around carbon black in SBR with PFM and find a bound layer extent of approximately 60 nm (Fig. 20(e)), even after considering the influence of stress interaction effects and tip geometry.

4.2. Monomodal dynamic AFM

4.2.1. Introduction

Monomodal dynamic AFM has been used predominantly for the collection of topography and distribution of components within a material. Studies that use AM AFM and related techniques explicitly for property measurement are limited in analysis and extraction of surface properties. Recent developments have allowed for qualitative measurement of the loss tangent, and harmonic approximations of the amplitude modulated approach curve (AMAC) can extract some information about the average contact stiffness and dissipation (Section 2.2.5). The major benefit of AM AFM is the low

forces and high scan speed that make it well suited for nanoscale analysis of dispersed components, as long as sufficient contrast in the energy dissipated from the tip by the different components is generated during scanning.

4.2.2. Use cases

The high speed, stable imaging that is possible with AM AFM [359] make it well suited to mapping microstructure and characterizing the dispersion of components in complex systems. As a result, AM AFM has been the predominant single-frequency dynamic AFM mode used for the study of polymer composites. While the link between perturbations in tip oscillation and changes in material dynamics is indirect and convoluted, several studies have used AM AFM to map nanoscale property gradients in polymers. In these investigations, phase contrast is the predominant property used to characterize polymer surface properties. [133,310,360,361] In studies that use phase data, comparison to other data channels can help with interpretation of AM AFM measurements. [362] [63,264,267] One of the first studies [281] to consider structural effects on the measurement of the interphase layer in insitu HNBR-carbon black rubber composites used both torsional resonance AFM and AM AFM. AM AFM phase measurements estimated the interphase to be 19 \pm 8 nm wide at room tempera-

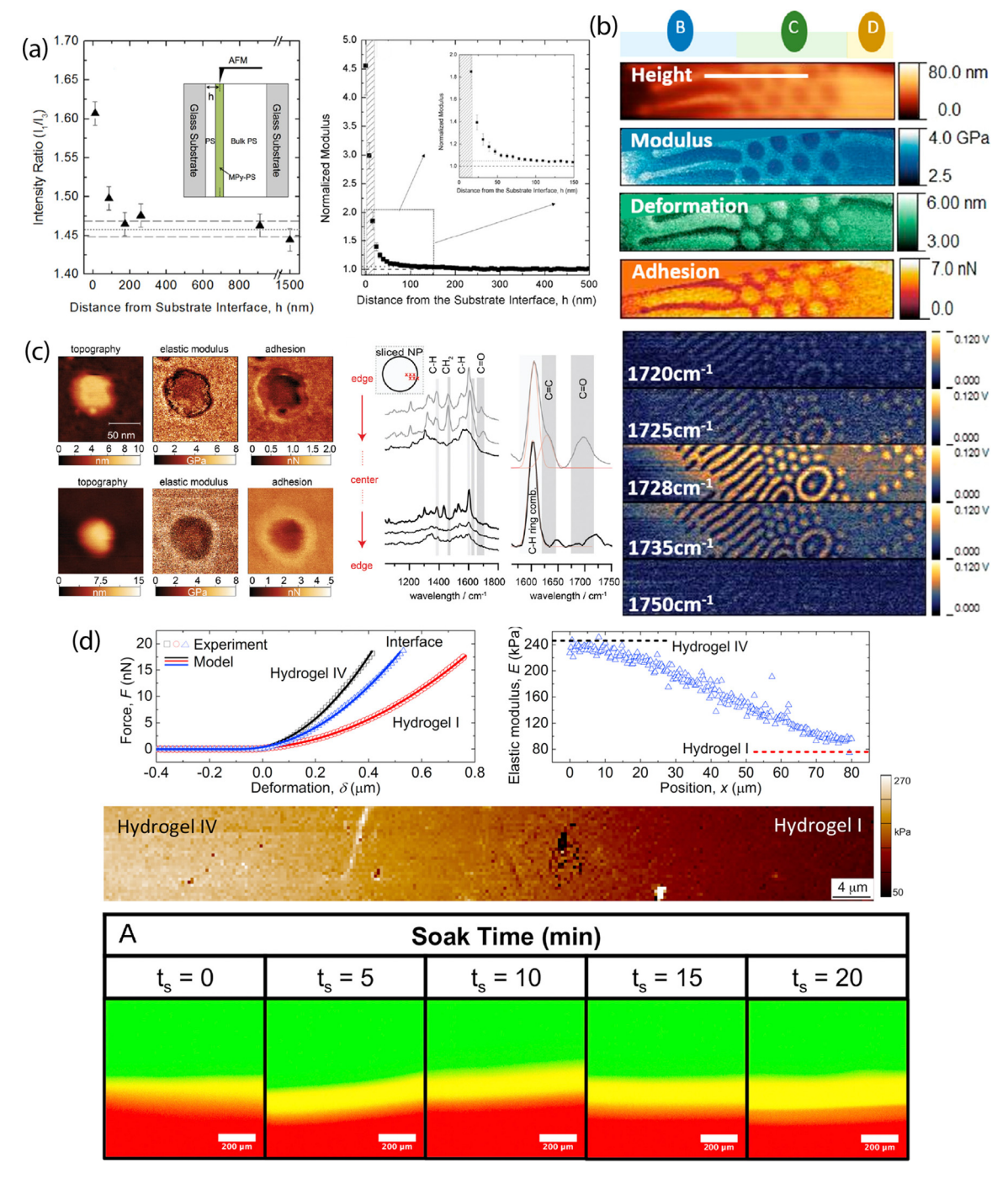


Fig. 21. (a) Comparison of measurement of DMT modulus via PFM and molecular stiffness via fluorescence of a labelled thin film of polystyrene near a silica interface. An increase in the intensity ratio is associated with increased molecular stiffness within the labelled layer that is placed at a distance, *h* from the interface as shown in the inset. PFM measurements on the same sample show a correlated increase in modulus within 60-80 nm of the silica-PS interface. [332], Copyright 2017. Adapted with permission from the American Chemical Society. (b) PFM of a poly(styrene-block-tert-butyl acrylate) thin film resolves the sub-surface PtBuA features, which are softer than the PS domains. The mechanical property maps compare well to scanning near-field optical microscopy which shows high contrast at the 1728 cm⁻¹ wavenumber between the PS and the PtBuA due to strong absorption by the carbonyl bond in the PtBuA domains. [355], Copyright 2019. Adapted with permission from the American Chemical Society. (c) PFM and tip-enhanced Raman spectroscopy on PS nanospheres embedded in cross linked resin, with the changes in elastic modulus and adhesion at the interface correlated to asymmetry in the Raman spectra between the bulk of the PS nanosphere and at the interface. At the interface the CH ring combination band, the C=C stretching mode and the C=O suggests that the resin has infiltrated the PS nanosphere at the interface, but the lack of these features in the bulk of the PS suggests that the infiltration is localized, in agreement with PFM measurements. [356], Copyright 2020. Reproduced with permission from John Wiley and Sons Inc. (d) Example of the mechanical properties across the interface between two photo-clickable thiol-ene hydrogels. Representative force curves in the bulk of each hydrogel as well as in the interphase are provided as well as the acquired AFM map and average elastic modulus as a function of position across the interface, *x*. Representative confocal microscopy images across the same hydrog

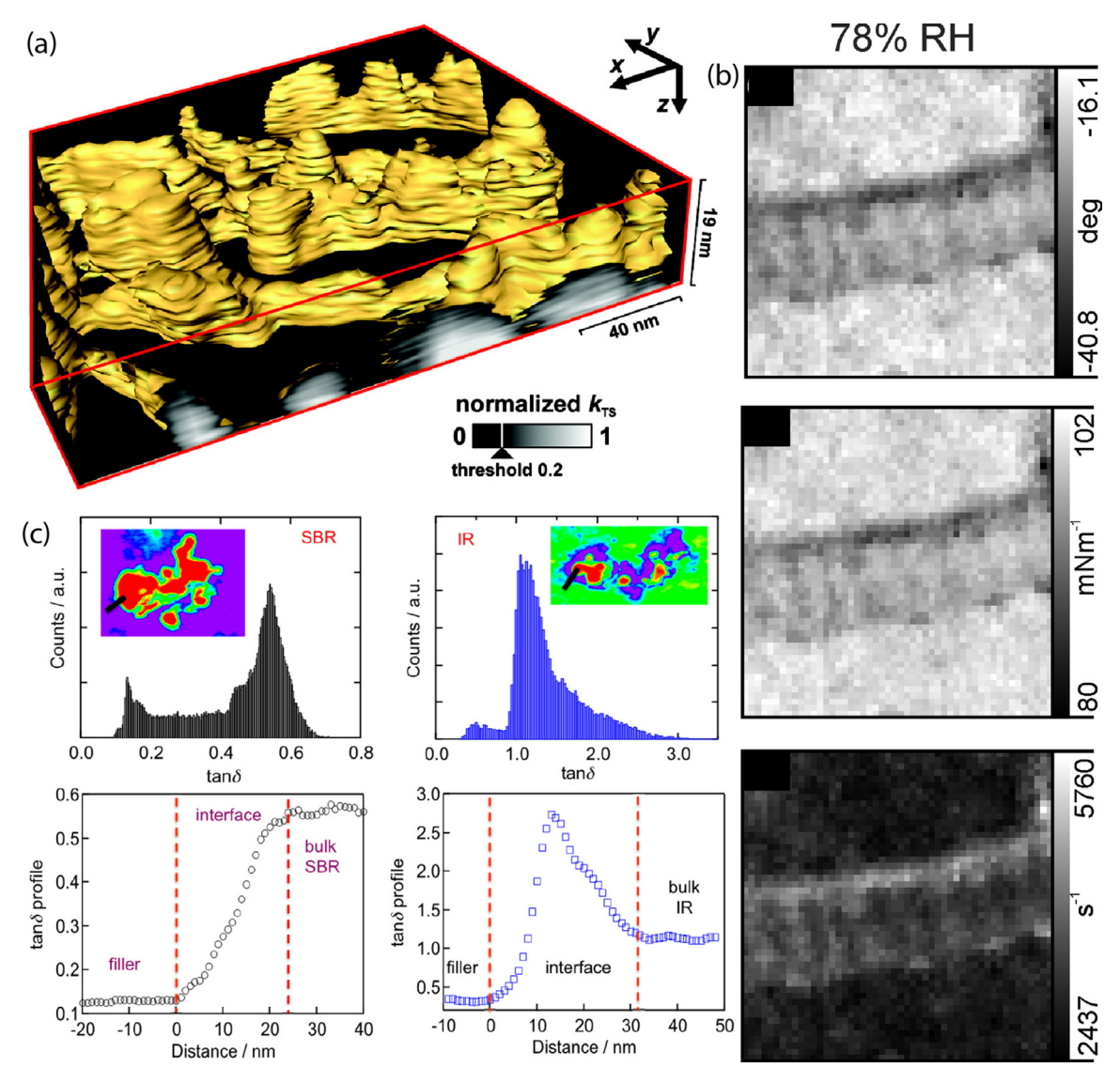


Fig. 22. (a) Depth-resolved maps of contact stiffness in an elastomeric polypropylene using Schröter's [107] harmonic approximation of AM AFM. Bright regions correspond to high contact stiffness due to the crystalline lamellae and softer, amorphous regions are dark. With increasing dynamic indentation depth, as calculated by the method from ref. [105], structure deeper in the material can be resolved. A cross section of the volumetric map shows the depth resolved contact stiffness. [364], Copyright 2010. Adapted with permission from the American Chemical Society. (b) Phase, contact stiffness and contact dissipation maps of a hydrated Type I collagen fibril. Changes in the phase channel can be correlated to conservative or dissipative contributions. Contrast in the mechanical properties of the hydrated collagen fibril is associated with uptake of water in the high humidity environment. [365], Copyright 2015. Adapted with permission from the American Chemical Society. (c) Histogram of loss tangent around a HAF grade carbon black particle in styrene-butadiene (left) and isoprene (right) rubbers. Insets: Maps of loss tangent surrounding the carbon black in each rubber and corresponding profiles of loss tangent across the bound layer between the bulk rubbers and the carbon black, with the location of the profile indicated by a black line. [366], Copyright 2018. Reproduced with permission from the American Chemical Society.

ture with decreasing interphase layer thickness at higher temperatures, while torsional resonance AFM suggested that the bound layer modulus is 53 MPa (compared to 3 MPa for neat HNBR). AM AFM measurements of the interphase around silica particles in SBR measured a larger interphase (~15 nm) than what was measured on the same system via NMR (3-5 nm). [363] The contrast was ascribed by the authors to the NMR only measuring the immobilized, directly adsorbed rubber, whereas the AFM is also sensitive to the loosely bound layer that is entangled or crosslinked with the directly bound rubber.

Mapping of material properties from AM AFM is generally limited to the loss tangent. Nguyen *et al.* used the loss tangent measurement (Eq. 36) provided by AM AFM to map the change in polymer segmental mobility (Fig. 22(c)) near carbon black for styrene-butadiene and polyisoprene rubbers (Fig. 6e-f). [366] When probed

by an AFM cantilever oscillating at resonance ($f_0 \sim 300 \text{ kHz}$), the SBR studied is below its glass transition point and as such the loss tangent monotonically decreases as the segmental mobility slows near the carbon black particle. It should be noted however that the impact of the stiff, elastic carbon black on the loss tangent measurement was not considered for this analysis. AM AFM images on carbon black-PDB rubber composites also suggest a bound layer in agreement with the above measurements. [360]

The harmonic approximations to the dynamic oscillation of the AFM cantilever developed by Schröter *et al.* [107] have been applied by Spitzner *et al.* to engineering polymers [364] and biopolymers [365] to resolve structure (Fig. 22(a-b)). In combination with the indentation depth estimation method of Knoll *et al.* [105], depth dependent contact stiffness maps can be resolved as demonstrated in semi-crystalline polypropylene (Fig. 22(a)) in a similar

manner to the stiffness tomography images collected with FV AFM data. [223]

4.3. Contact resonance

4.3.1. Introduction

Contact resonance (CR) is a powerful, highly sensitive technique for viscoelastic property measurement, [367] but acquiring the full set of frequencies used to construct the resonance peak either through a chirp (frequency sweep) or band excitation (BE) is time consuming. Fixed frequency or PLL control enable faster scanning, but they are unable to provide viscoelastic property measurements. In addition, the stiff cantilevers historically needed for accurate contact resonance spectra required high loads, limiting applicability to polymeric materials. The recently developed DART (dual-AC resonance tracking) CR and FFV CR address some of the issues surrounding long acquisition times while allowing viscoelastic analysis and, in conjunction with use of the higher-order eigenmodes of soft cantilevers, has allowed for broader use of contact resonance techniques for low-force, high-resolution analysis of complex glassy polymer blends and composites.

4.3.2. Use cases

Elastic CR AFM studies on the impact of interfaces on polymers have been conducted predominantly on fiber composites to investigate role of fiber surface treatment on the local polymer properties. One example of CR AFM for mapping on a polymer interphase is given in Fig. 23(a), where examination of the effect of adding malleated polypropylene (MAPP) to isotactic polypropylene on the interphase between a cellulose fiber and polypropylene matrix indicated a longer interphase layer up ~140 nm in length with an increase in MAPP. [368,369] Similar to some combined quasi-static indentation and FEA studies, Zhou et al. compared CR AFM measurements at the interface of a glass-fiber epoxy composite to FEA and determined that a 476 nm interphase was required to explain their results. [370] DART-CR AFM was also used to examine the mechanical properties of several clay/PEDOT:PSS nanocomposites, with conductivity measured through conductive AFM. It was observed that the mechanical properties and conductivity were through application of a compressive force to the surface of the nanocomposite films, which was attributed to compaction of the brick-and-mortar structure of the composite [371].

The high sensitivity of CR AFM to changes in contact stiffness [372] has resulted in frequent application of CR to detecting buried nanoparticles [225-227,373] and imaging of subsurface features buried under a layer of polymer, an example of which is provided in Fig. 23(b). Imaging of sub-surface features with DART-CR AFM was applied to Au circuits buried in PMMA, with defects detected in the printed circuit as small as 100 nm, the smallest feature size tested. [374]

Viscoelastic CR measurements have also been applied to study several composite systems. The sensitivity of CR measurements to VE properties was demonstrated on a cartilage-bone interface where a measured $2.3 \pm 1.2~\mu m$ wide interphase gradient in modulus and loss tangent (Fig. 23(c)) was associated with a gradual decrease in mineral content in the cartilage away from the bone. [375] A study looking at temperature dependence provided the average surface loss tangent of a CNT/epoxy composite, showing a lower loss tangent in the nanocomposite than the neat epoxy at low temperatures. [376] One study employed BE contact resonance for the imaging of the elastic and dissipative components of the tip-surface interactions around silica particles in PVAc, with alterations to the local stiffness and dissipation of the polymer modified over a similar length scale. [377]

4.4. Multi-modal dynamic AFM

4.4.1. Introduction

The high resolution, high sensitivity, and low applied force of bimodal AFM techniques allow for precise analysis of subtle changes in polymer surface dynamics and stiffness. There have been a number of studies demonstrating AM-FM and other bimodal methods on polymer blends, individual polymer chains and biological systems [19] showing that AM-FM is capable of high resolution, sensitive imaging in liquid and gaseous environments across a range of samples and moduli (1 MPa to 100 GPa). [27] AM-FM AFM is also less impacted by the quasi-static mode requirement that the cantilever stiffness be similar to the contact stiffness. [27] Despite this flexibility, application of AM-FM to the systematic study of polymers under confinement or near interfaces remains limited. While the assumption of Hertzian contact mechanics limits the quantitative accuracy of AM-FM on soft materials [143] due to adhesion and other non-linear effects, AM-FM has a broad range of application for high resolution imaging on glassy and rubbery polymers, particularly in a liquid environment, in which the influence of adhesion on the tip is minimized.

4.4.2. Use cases

Several recent studies have used multimodal techniques for the study of polymer composites, but the use of the high-resolution viscoelastic property mapping capabilities of these modes remains underutilized. A study that used intermodulation AFM to map the surface of PDMS-silica composites [147] with nanoscale resolution demonstrated the ability to resolve the changes in local stiffness and dissipation around the silica particles (Fig. 24(a)). Inter modulation AFM has also been used for the mapping of a thermoplastic alloy. [378] Trimodal AFM operation has been demonstrated for the simultaneous measurement of topography and mechanical contrast while also modulating indentation depth and has been implemented to image nanoparticles buried in PDMS. [379] Other studies have used AM-FM AFM for mechanical property imaging of biochar-starch and polymer composites, [380] as well as glass fiber/epoxy composites. [381] The capability of AM-FM AFM and other bimodal methods to map viscoelastic properties with high sensitivity and high resolutionhave been demonstrated on several block co-polymers [25] (Fig. 24(b)) and in molecular biology. [9]

Outside of polymer composites, AM-FM has been applied to a wide range of materials and systems. An AM-FM study was able to demonstrate the influence of sepsis on collagen fibers and mineral in the bones of mice and found that there are initial changes in the elastic modulus, related to the chemical composition of the collagen and bone for 96 h after the sepsis insult. [384] The viscoelastic mapping capabilities of AM-FM have also recently been applied to map the properties of a DPPC lipid bilayer, [382] where the modulation of the storage and loss moduli through the addition of cholesterol was measured (Fig. 24(c)). Temperature dependent AM-FM measurements on a spin cross-over (SCO) complex [383] show a phase transition from a low spin state to a high spin state and an associated decrease in the storage modulus (Fig. 24(d)). AM-FM imaging near a defect in the SCO complex found a premature phase change in the SCO complex at lower temperatures than in the bulk due to the defect.

4.5. Conclusions

AFM maintains a niche in the study of nanostructured polymers due to the direct real space measurement at the nanoscale and unique ability to map phases and their respective mechani-

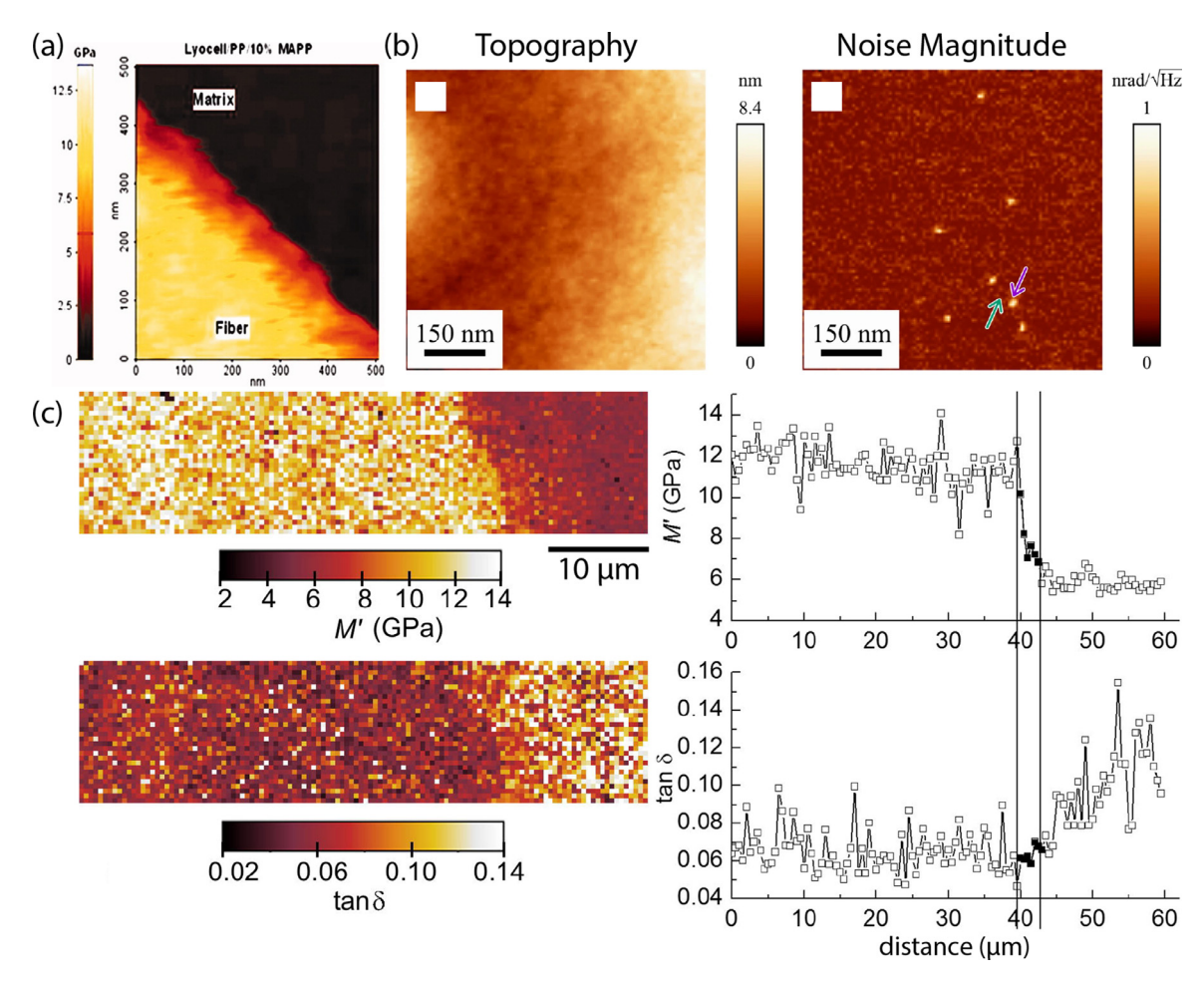


Fig. 23. (a) Indentation modulus maps as measured by contact resonance AFM across a cellulose fiber – polypropylene interface with 10% malleated polypropylene incorporated into the matrix. [368], Copyright 2012. Adapted with permission from John Wiley and Sons Inc. (b) Height and thermal noise magnitude acquired from scanning thermal noise contact resonance measurements on a spin coated photopolymer film with Au particles 40 nm in diameter buried 300 nm beneath the surface. The high sensitivity of the thermal noise contact resonance measurement allows for observation of the small Au NP far below the surface that are not featured in topographical maps. [227], Copyright 2017. Adapted with permission under CC BY 4.0 – published by SpringerNature. (c) Gradient of storage modulus (M) and loss tangent (tan δ) across the osteochondral interface, with the interphase region extending up to 5 μ m correlated with a decrease in mineral fraction as measured by quantitative backscattered electron measurements in SEM. [375], Copyright 2012. Adapted with permission from Elsevier Science Ltd.

cal properties, thereby expanding the toolbox of nanoscale analysis in heterogeneous polymers. In comparison, scattering techniques have provided a wealth of information but are limited by the inversion of their reciprocal space measurements. Molecular and atomistic simulations have also provided detailed insight into polymer structure and configuration but still require experimental validation. We believe that the contributions of AFM to the nanoscale analysis of polymers and other soft materials are still not yet fully explored, especially with the emergent viscoelastic techniques that are, in combination, capable of directly probing dynamics and elasticity simultaneously across 7 decades or more in frequency with nanoscale resolution.

A major barrier for accurate characterization of the interphase and interfaces in multicomponent systems is the influence that a neighboring domain has on an AFM indentation, where complementary modeling methods and experimental techniques can offer valuable insight in interpreting the experimental results. Future AFM studies in heterogenous systems should consider whether the gradient measured is significant relative to the size of the contact area, tip radius and stress interaction effects. Methods and best practices for minimizing or accounting for the impact of structural effects on AFM measurements are detailed in Section 3.2.

Furthermore, the wide variance in execution of an AFM mode and calibration makes informed comparison between studies on similar systems difficult. In general, we recommend that calibration details, the measured or assumed tip radius, and examples of raw force spectroscopy data should be reported as standard in nanomechanical AFM studies. In addition, it may be beneficial to pursue well-characterized and standardized samples to test the calibration and operation of specific modes across a range of moduli and viscoelastic behavior. Such a library of standardized samples would also include multiphase samples, which would help establish the quantitative contrast and resolution achievable with a given mode. We suggest that as part of a study, a researcher could present their nanomechanical measurements (using their desired operation parameters) on a standard sample in addition to their system of interest to help provide context and a reference point between AFM studies. The materials to be included in the standardized library should aim to be isotropic with minimal surface effects, resistant to chemical and physical aging, resistant to humidity, washable and simple to source or manufacture. While specifying the exact materials or specimens to be included in this library is outside the scope of this review, we believe efforts in establishing a standardized library would support the push towards truly quantitative nanomechanical AFM.

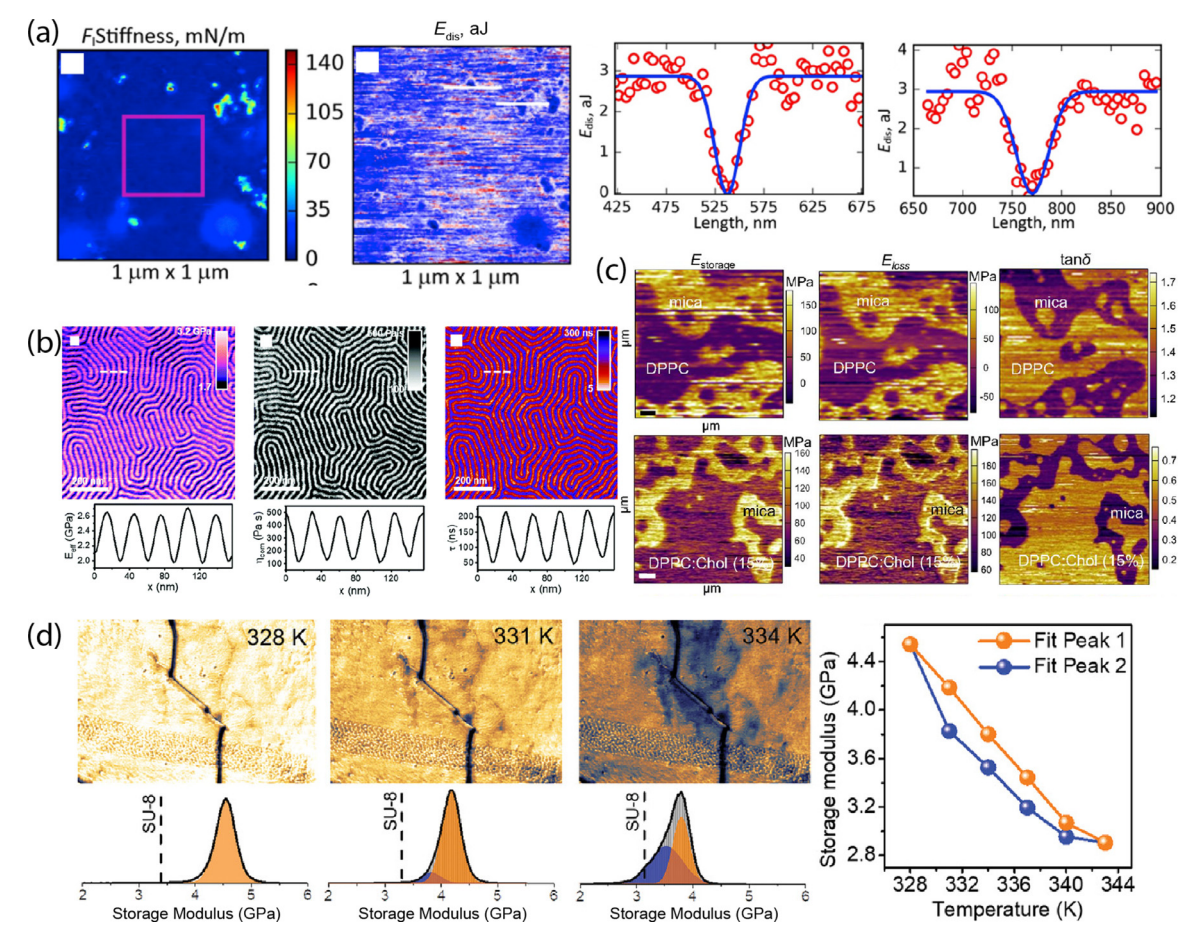


Fig. 24. (a) Map of dissipation as measured by Intermodulation AFM on the surface of a PDMS-silica nanocomposite. The profiles of $E_{\rm dis}$ are acquired from locations indicated by the white lines. A corresponding map of the conservative interactions as represented by the stiffness is given below the dissipation map. The nominal silica particle size is 16 nm, with a measured interphase thickness of 10-30 nm measured. Adapted from [147] with permission from Elsevier Science Ltd. (b) AM-FM maps of elastic modulus ($E_{\rm eff}$), viscosity (η) and characteristic relaxation time (τ) for a PS-PMMA block co-polymer. [25], Copyright 2019. Adapted with permission under CC BY-NC 3.0 – published by the Royal Society of Chemistry. (c) AM-FM maps of storage modulus, loss modulus and loss tangent of a DPPC lipid bi-layer with a molar fraction insert of 0% (top row) and 15% (bottom row) cholesterol. An increase in the fraction of cholesterol stiffens the model DPPC lipid bi-layer, which is observable in the measured AM-FM variables. Scale bar is 500 nm. [382], Copyright 2017. Adapted with permission from the National Academy of Sciences. (d) AM-FM measurement of storage modulus around a defect on a SCO complex film. An increase in temperature demonstrates a softening, with the crack serving as a nucleation site for a premature spin transition temperature, leading to a bimodal distribution of modulus. Scan size is 5 × 3.5 μm² [383], Copyright 2019. Adapted with permission from John Wiley and Sons Inc.

5. Summary

In summary, we have provided the dedicated AFM user and curious experimentalists a guidebook for assessing the capabilities of quasi-static and dynamic AFM modes for elastic and viscoelastic characterization of polymers, as well as current best practices for achieving accurate and reliable results. In Section 2, current AFM modes (Table 1) are reviewed and their current capabilities for elastic and viscoelastic property measurement are discussed. Section 3 details the efforts over the past decade to improve the procedures for AFM calibration (Section 3.1) and conducting measurements on polymer systems (Sections 3.2). On the basis of the current literature, we have collated best practices for AFM calibration (Table 5), operating conditions (Table 6) and accounting for various phenomena in mechanical property measurement (Table 8). To demonstrate some of the current capabilities of high resolution AFM mechanical property measurement, we have also provided an overview of studies (Section 4) that utilize quantitative AFM modes to investigate viscoelastic and elastic property gradients and heterogeneity in nanostructured polymers.

Improvements in the calibration of the AFM instrument have improved the quantitative accuracy of nanoscale property measurements but the approximations made for inferring the nanoscale AFM contact area still limits analysis. Efforts to standardize calibration procedures, including independently calibrated cantilever spring constants, have been beneficial for improving repeatability and accuracy of property measurements. The quantitative accuracy of dynamic AFM methods is still hindered by the Hertzian contact mechanics assumptions currently used to interpret measurements, particularly on elastomers and other materials with low modulus. As such, quasi-static AFM remains better suited to addressing adhesive tip-sample interactions, but advancements in modelling of the tip-sample contact in dynamic AFM [102,385] may prove critical for accurately interpreting collected data on adhesive materials with dynamic AFM modes. For both dynamic and quasi-static modes, comparison of shallow AFM indentations with sharp (R < 30 nm) tips to macroscale mechanical properties and even instrumented nanoindentation is fraught due to size effects as a result of polymer structure and the proximity of the free surface. Further investigation with other, independent measures of mechanical properties near the surface would be immensely beneficial to determine the accuracy of measurements that probe within the layer of polymer affected by the free surface.

AFM is a powerful technique for nanoscale characterization of surface properties but remains subject to convoluting artifacts due to the deformation behavior of the surface, changes in or

contamination of the probe tip and structural effects due to the sample geometry. Future studies on mapping the *in situ* properties of polymers should make use of the available tools to identify whether measured mechanical property gradients or heterogeneities are affected by continuum level artifacts and either account for their influence or adjust the experiment to minimize them. In addition, advancements in compensation for surface topography during AFM operation or gentle surface preparation methods to reduce surface roughness, particularly for samples that include large, hard components that thwart typical surface preparation techniques, would be beneficial for reduction of mechanical artifacts.

The last decade has seen the emergence and development of a range of AFM methods to probe viscoelastic properties with high resolution and sensitivity. The construction of viscoelastic master curves with nanoscale resolution has been demonstrated by multiple - predominantly quasi-static - techniques. Multi-frequency dynamic AFM modes have emerged as a tool for highly sensitive nanomechanical measurement and mapping across a broad range of soft materials. Quasi-static modes, due to the direct visualization of force with indentation depth are the subject of ever more detailed analysis for the interpretation of material deformation in a variety of conditions and systems. Continued development of advanced AFM techniques that combine either dynamic or quasistatic AFM with complementary ex situ and in situ electrical, chemical, optical, or scattering measurements will help correlate mechanical property measurements to underlying structure and function. The next decade promises important new advances in these areas and will lead to higher accuracy mechanical property measurements on complex soft materials that will enhance material discovery and design.

Declaration of Competing Interest

The authors declare that they have no known competing financial interests or personal relationships that could have appeared to influence the work reported in this paper.

Acknowledgements

The authors acknowledge support from NSF BCS-1734981, AFOSR FA9550-18-1-0381 and NSF-CMMI-DMREF grant 1818574. The authors would also like to thank Heer Majitha for her valuable discussion and comments as well as Christopher M. Stafford for his constructive feedback.

References

- [1] Binnig G, Quate CF, Gerber C. Atomic force microscope. Phys Rev Lett 1986;56:930–3.
- [2] Butt H-J, Cappella B, Kappl M. Force measurements with the atomic force microscope: Technique, interpretation and applications. Surf Sci Rep 2005;59:1–152.
- [3] Garcia R, Herruzo ET. The emergence of multifrequency force microscopy. Nat Nanotechnol 2012;7:217–26.
- [4] Chyasnavichyus M, Young SL, Tsukruk VV. Recent advances in micromechanical characterization of polymer, biomaterial, and cell surfaces with atomic force microscopy. JaJAP 2015;54 08LA2/1-13.
- [5] Killgore JP, DelRio FW. Contact Resonance Force Microscopy for Viscoelastic Property Measurements: From Fundamentals to State-of-the-Art Applications. Macromolecules 2018:51:6977–96.
- [6] Garcia R. Nanomechanical mapping of soft materials with the atomic force microscope: methods, theory and applications. Chem Soc Rev 2020:49:5850–84.
- [7] Wang D, Russell TP. Advances in Atomic Force Microscopy for Probing Polymer Structure and Properties. Macromolecules 2017;51:3–24.
- [8] Krieg M, Fläschner G, Alsteens D, Gaub BM, Roos WH, Wuite GJL, et al. Atomic force microscopy-based mechanobiology. Nature Reviews Physics 2018;1:41–57.
- [9] Dufrene YF, Ando T, Garcia R, Alsteens D, Martinez-Martin D, Engel A, et al. Imaging modes of atomic force microscopy for application in molecular and cell biology. Nat Nanotechnol 2017;12:295–307.

- [10] Chyasnavichyus M, Young SL, Tsukruk VV. Probing of polymer surfaces in the viscoelastic regime. Langmuir 2014;30:10566–82.
- [11] Efremov YM, Shpichka AI, Kotova SL, Timashev PS. Viscoelastic mapping of cells based on fast force volume and PeakForce Tapping. Soft Matter 2019;15:5455–63.
- [12] Tsukruk VV, Singamaneni S. Scanning Probe Microscopy of Soft Matter: Fundamentals and Practices. Hoboken: John Wiley & Sons, Inc.; 2011. p. 642.
- [13] Johnson KL, Greenwood JA. An Adhesion Map for the Contact of Elastic Spheres. J Colloid Interface Sci 1997;192:326–33.
- [14] Efremov YM, Wang WH, Hardy SD, Geahlen RL, Raman A. Measuring nanoscale viscoelastic parameters of cells directly from AFM force-displacement curves. Sci Rep 2017;7 1541/1-14.
- [15] Gigler AM, Marti O. Quantitative Measurement of Materials Properties with the (Digital) Pulsed Force Mode. In: Tomitori M, Bhushan B, Fuchs H, editors. Applied Scanning Probe Methods IX: Characterization. Berlin, Heidelberg: Springer Berlin Heidelberg; 2008. p. 23–54.
- [16] Amo CA, Garcia R. Fundamental High-Speed Limits in Single-Molecule, Single-Cell, and Nanoscale Force Spectroscopies. ACS Nano 2016;10:7117–24.
- [17] Pittenger B, Erina N, Su C. Quantitative mechanical property mapping at the nanoscale with PeakForce QNM. Application Note Veeco Instruments Inc 2010:1.
- [18] Proksch R, Yablon DG. Loss tangent imaging: Theory and simulations of repulsive-mode tapping atomic force microscopy. Appl Phys Lett 2012;100 073106/1-3.
- [19] Amo CA, Perrino AP, Payam AF, Garcia R. Mapping Elastic Properties of Heterogeneous Materials in Liquid with Angstrom-Scale Resolution. ACS Nano 2017:11:8650-9.
- [20] García R. Dynamic atomic force microscopy methods. Surf Sci Rep 2002;47:197–301.
- [21] Korolkov VV, Summerfield A, Murphy A, Amabilino DB, Watanabe K, Taniguchi T, et al. Ultra-high resolution imaging of thin films and single strands of polythiophene using atomic force microscopy. Nat Commun 2019;10:1537.
- [22] Yamashita H, Taoka A, Uchihashi T, Asano T, Ando T, Fukumori Y. Single– Molecule Imaging on Living Bacterial Cell Surface by High-Speed AFM. J Mol Biol 2012;422:300–9.
- [23] Kikuchi Y, Obana N, Toyofuku M, Kodera N, Soma T, Ando T, et al. Diversity of physical properties of bacterial extracellular membrane vesicles revealed through atomic force microscopy phase imaging. Nanoscale 2020;12:7950–9.
- [24] Liu YH, Wang D, Nakajima K, Zhang W, Hirata A, Nishi T, et al. Characterization of Nanoscale Mechanical Heterogeneity in a Metallic Glass by Dynamic Force Microscopy. Phys Rev Lett 2011;106 125504/1-4.
- [25] Benaglia S, Amo CA, Garcia R. Fast, quantitative and high resolution mapping of viscoelastic properties with bimodal AFM. Nanoscale 2019;11:15289–97.
- [26] Garcia R, Proksch R. Nanomechanical mapping of soft matter by bimodal force microscopy. Eur Polym J 2013;49:1897–906.
- [27] Kocun M, Labuda A, Meinhold W, Revenko I, Fast Proksch R. High Resolution, and Wide Modulus Range Nanomechanical Mapping with Bimodal Tapping Mode. ACS Nano 2017;11:10097–105.
- [28] Labuda A, Kocun M, Meinhold W, Walters D, Proksch R. Generalized Hertz model for bimodal nanomechanical mapping. Beilstein J Nanotechnol 2016;7:970–82.
- [29] Yuya PA, Hurley DC, Turner JA. Contact-resonance atomic force microscopy for viscoelasticity. J Appl Phys 2008;104 074916/1-7.
- [30] Seal K, Jesse S, Rodriguez BJ, Baddorf AP, Kalinin SV. High frequency piezoresponse force microscopy in the 1-10MHz regime. Appl Phys Lett 2007;91 232904/1-3.
- [31] Yablon DG, Gannepalli A, Proksch R, Killgore J, Hurley DC, Grabowski J, et al. Quantitative Viscoelastic Mapping of Polyolefin Blends with Contact Resonance Atomic Force Microscopy. Macromolecules 2012;45:4363–70.
- [32] Killgore JP, Yablon DG, Tsou AH, Gannepalli A, Yuya PA, Turner JA, et al. Viscoelastic property mapping with contact resonance force microscopy. Langmuir 2011;27:13983-7.
- [33] Stan G, Solares SD, Pittenger B, Erina N, Su C. Nanoscale mechanics by tomographic contact resonance atomic force microscopy. Nanoscale 2014:6:962-9.
- [34] Kolluru PV, Eaton MD, Collinson DW, Cheng X, Delgado DE, Shull KR, et al. AFM-based Dynamic Scanning Indentation (DSI) Method for Fast, High-resolution Spatial Mapping of Local Viscoelastic Properties in Soft Materials. Macromolecules 2018;51:8964–78.
- [35] Pittenger B, Osechinskiy S, Yablon D, Mueller T. Nanoscale DMA with the Atomic Force Microscope: A New Method for Measuring Viscoelastic Properties of Nanostructured Polymer Materials. JOM 2019;71:3390–8.
- [36] Igarashi T, Fujinami S, Nishi T, Asao N, aK Nakajima. Nanorheological Mapping of Rubbers by Atomic Force Microscopy. Macromolecules 2013;46:1916–22.
- [37] Nalam PC, Gosvami NN, Caporizzo MA, Composto RJ, Carpick RW. Nano-rheology of hydrogels using direct drive force modulation atomic force microscopy. Soft Matter 2015;11:8165–78.
- [38] Nakajima K, Ito M, Wang D, Liu H, Nguyen HK, Liang X, et al. Nano-pal-pation AFM and its quantitative mechanical property mapping. Microscopy 2014;63:193–208.
- [39] Cappella B. Physical Principles of Force–Distance Curves by Atomic Force Microscopy. In: Mechanical Properties of Polymers Measured through AFM Force-Distance Curves. Cham: Springer International Publishing; 2016. p. 3–66.

- [40] Kashfipour MA, Mehra N, Zhu J. A review on the role of interface in mechanical, thermal, and electrical properties of polymer composites. Advanced Composites and Hybrid Materials 2018;1:415–39.
- [41] Kumar SK, Benicewicz BC, Vaia RA, Winey KI. 50th Anniversary Perspective: Are Polymer Nanocomposites Practical for Applications? Macromolecules 2017:50:714–31.
- [42] Bansal A, Yang H, Li C, Cho K, Benicewicz BC, Kumar SK, et al. Quantitative equivalence between polymer nanocomposites and thin polymer films. Nat Mater 2005;4:693–8.
- [43] Berthier L, Biroli G. Theoretical perspective on the glass transition and amorphous materials. RvMP 2011;83:587–645.
- [44] Schweizer KS, Simmons DS. Progress towards a phenomenological picture and theoretical understanding of glassy dynamics and vitrification near interfaces and under nanoconfinement. J Chem Phys 2019;151 240901/1-27.
 [45] Bostanabad R, Zhang Y, Li X, Kearney T, Brinson LC, Apley DW, et al. Com-
- [45] Bostanabad R, Zhang Y, Li X, Kearney T, Brinson LC, Apley DW, et al. Computational microstructure characterization and reconstruction: Review of the state-of-the-art techniques. Prog Mater Sci 2018;95:1–41.
- [46] Benaglia S, Gisbert VG, Perrino AP, Amo CA, Garcia R. Fast and high-resolution mapping of elastic properties of biomolecules and polymers with bimodal AFM. Nat Protoc 2018;13:2890–907.
- [47] Dokukin M, Sokolov I. High-resolution high-speed dynamic mechanical spectroscopy of cells and other soft materials with the help of atomic force microscopy. Sci Rep 2015;5 12630/1-14.
- [48] Galluzzi M, Tang G, Biswas CS, Zhao J, Chen S, Stadler FJ. Atomic force microscopy methodology and AFMech Suite software for nanomechanics on heterogeneous soft materials. Nat Commun 2018;9 3584/1-10.
- [49] Pimenta-Lopes C, Suay-Corredera C, Velázquez-Carreras D, Sánchez-Ortiz D, Alegre-Cebollada J. Concurrent atomic force spectroscopy. Communications Physics 2019;2 91/1-11.
- [50] Efremov YM, Okajima T, Raman A. Measuring viscoelasticity of soft biological samples using atomic force microscopy. Soft Matter 2020;16:64–81.
- [51] Cappella B, Dietler G. Force-distance curves by atomic force microscopy. Surf Sci Rep 1999;34:1–104.
- [52] Hertz HR. Über Die Berührung Fester Elastischer Körper. J für die Reine und Angew Math 1881;92:156–71.
- [53] Derjaguin BV, Muller VM, Toporov YP. Effect of contact deformations on the adhesion of particles. J Colloid Interface Sci 1975;53:314–26.
- [54] Johnson KL, Kendall K, Roberts AD, Tabor D. Surface energy and the contact of elastic solids. Proceedings of the Royal Society of London A Mathematical and Physical Sciences 1997;324:301–13.
- [55] Maugis D. Adhesion of spheres: The JKR-DMT transition using a dugdale model. J Colloid Interface Sci 1992;150:243–69.
- [56] Oliver WC, Pharr GM. An improved technique for determining hardness and elastic modulus using load and displacement sensing indentation experiments. J Mater Res 2011;7:1564–83.
- [57] Johnson KL. One Hundred Years of Hertz Contact. Proceedings of the Institution of Mechanical Engineers 1982;196:363–78.
- [58] Sneddon IN. The relation between load and penetration in the axisymmetric boussinesq problem for a punch of arbitrary profile. IJES 1965;3:47–57.
- [59] Jiang Y, Turner KT. Measurement of the strength and range of adhesion using atomic force microscopy. Extreme Mechanics Letters 2016;9:119–26.
- [60] Attard P. Measurement and interpretation of elastic and viscoelastic properties with the atomic force microscope. J Phys: Condens Matter 2007;19 473201/1-33.
- [61] Tranchida D, Kiflie Z, Acierno S, Piccarolo S. Nanoscale mechanical characterization of polymers by atomic force microscopy (AFM) nanoindentations: viscoelastic characterization of a model material. Meas Sci Technol 2009;20 095702/1-9
- [62] Efremov YM, Bagrov DV, Kirpichnikov MP, Shaitan KV. Application of the Johnson-Kendall-Roberts model in AFM-based mechanical measurements on cells and gel. Colloids Surf B Biointerfaces 2015;134:131–9.
- [63] Wang D, Liang X-B, Liu Y-H, Fujinami S, Nishi T, Nakajima K. Characterization of Surface Viscoelasticity and Energy Dissipation in a Polymer Film by Atomic Force Microscopy. Macromolecules 2011;44:8693–7.
- [64] Thorén P-A, Borgani R, Forchheimer D, Dobryden I, Claesson PM, Kassa HG, et al. Modeling and Measuring Viscoelasticity with Dynamic Atomic Force Microscopy. Physical Review Applied 2018;10 024017/1-13.
- [65] Lopez-Guerra EA, Banfi F, Solares SD, Ferrini G. Theory of Single-Impact Atomic Force Spectroscopy in liquids with material contrast. Sci Rep 2018;8 7534(1):16
- [66] Solares SD. Nanoscale effects in the characterization of viscoelastic materials with atomic force microscopy: coupling of a quasi-three-dimensional standard linear solid model with in-plane surface interactions. Beilstein J Nanotechnol 2016;7:554–71.
- [67] Johnson KL. Contact Mechanics and Adhesion of Viscoelastic Spheres. Microstructure and Microtribology of Polymer Surfaces. American Chemical Society; 1999. p. 24–41.
- [68] Ting TCT. The Contact Stresses Between a Rigid Indenter and a Viscoelastic Half-Space. Journal of Applied Mechanics 1966;33:845–54.
- [69] Hui CY, Baney JM, Kramer EJ. Contact Mechanics and Adhesion of Viscoelastic Spheres. Langmuir 1998;14:6570–8.
- [70] Ahn D, Shull KR. JKR Studies of Acrylic Elastomer Adhesion to Glassy Polymer Substrates. Macromolecules 1996;29:4381–90.
- [71] Shull KR. Contact mechanics and the adhesion of soft solids. Materials Science and Engineering: R: Reports 2002;36:1–45.

- [72] Attard P. Interaction and Deformation of Viscoelastic Particles. 2. Adhesive Particles. Langmuir 2001;17:4322–8.
- [73] Attard P. Interaction and deformation of viscoelastic particles: nonadhesive particles. Phys Rev E Stat Nonlin Soft Matter Phys 2001;63 061604/1-9.
- [74] Gillies G, Prestidge CA, Attard P. An AFM Study of the Deformation and Nanorheology of Cross-Linked PDMS Droplets. Langmuir 2002;18: 1674–1679.
- [75] Rajabifar B, Jadhav JM, Kiracofe D, Meyers GF, Raman A. Dynamic AFM on Viscoelastic Polymer Samples with Surface Forces. Macromolecules 2018:51:9649–61.
- [76] Lin DC, Dimitriadis EK, Horkay F. Robust strategies for automated AFM force curve analysis-II: adhesion-influenced indentation of soft, elastic materials. J Biomech Eng 2007;129:904–12.
- [77] Lin DC, Shreiber DI, Dimitriadis EK, Horkay F. Spherical indentation of soft matter beyond the Hertzian regime: numerical and experimental validation of hyperelastic models. Biomech Model Mechanobiol 2009;8:345–58.
- [78] Meyer E, Heinzelmann H, Grütter P, Jung T, Weisskopf T, Hidber HR, et al. Comparative study of lithium fluoride and graphite by atomic force microscopy (AFM). [Mic 1988;152:269–80.
- [79] Rosa-Zeiser A, Weilandt E, Hild S, Marti O. The simultaneous measurement of elastic, electrostatic and adhesive properties by scanning force microscopy: pulsed-force mode operation. Meas Sci Technol 1997;8:1333–8.
- [80] Lin DC, Dimitriadis EK, Horkay F. Robust strategies for automated AFM force curve analysis-I. Non-adhesive indentation of soft, inhomogeneous materials. J Biomech Eng 2007;129:430-40.
- [81] Lin DC, Horkay F. Nanomechanics of polymer gels and biological tissues: A critical review of analytical approaches in the Hertzian regime and beyond. Soft Matter 2008;4:669–82.
- [82] Fujinami S, Ueda E, Nakajima K, Nishi T. Analytical methods to derive the elastic modulus of soft and adhesive materials from atomic force microcopy force measurements. J Polym Sci, Part B: Polym Phys 2019;57:1279–86.
- [83] Nievergelt AP, Brillard C, Eskandarian HA, McKinney JD, Fantner GE. Photothermal Off-Resonance Tapping for Rapid and Gentle Atomic Force Imaging of Live Cells. Int J Mol Sci 2018;19 2984/1-11.
- [84] Meng X, Zhang H, Song J, Fan X, Sun L, Xie H. Broad modulus range nanomechanical mapping by magnetic-drive soft probes. Nat Commun 2017;8 1944/1-10.
- [85] García R. Amplitude Modulation Force Microscopy. Weinheim: Wiley VCH; 2010. p. 179.
- [86] Voigtländer B. Atomic Force Microscopy. 2 ed.. Cham: Springer International Publishing; 2019. p. 331.
- [87] Haugstad G. Atomic Force Microscopy: Understanding Basic Modes and Advanced Applications. New York: John Wiley and Sons Inc.; 2012. p. 528.
- [88] Garcia R. Theory of Amplitude Modulation AFM. Amplitude Modulation Atomic Force Microscopy; 2010. p. 41–57.
- [89] Preiner J, Tang J, Pastushenko V, Hinterdorfer P. Higher harmonic atomic force microscopy: imaging of biological membranes in liquid. Phys Rev Lett 2007;99 046102/1-4.
- [90] Crittenden S, Raman A, Reifenberger R. Probing attractive forces at the nanoscale using higher-harmonic dynamic force microscopy. PhRvB 2005;72 235422/1-13.
- [91] Stark RW, Drobek T, Heckl WM. Tapping-mode atomic force microscopy and phase-imaging in higher eigenmodes. Appl Phys Lett 1999;74:3296–8.
- [92] Rodríguez TR, Garciá R. Compositional mapping of surfaces in atomic force microscopy by excitation of the second normal mode of the microcantilever. Appl Phys Lett 2004;84:449–51.
- [93] Tamayo J, García R. Deformation, Contact Time, and Phase Contrast in Tapping Mode Scanning Force Microscopy. Langmuir 1996;12:4430-5.
- [94] Hölscher H. Quantitative measurement of tip-sample interactions in amplitude modulation atomic force microscopy. Appl Phys Lett 2006;89 123109/1-3.
- [95] Hu S, Raman A. Inverting amplitude and phase to reconstruct tip-sample interaction forces in tapping mode atomic force microscopy. Nanot 2008;19 375704/1-11.
- [96] Payam AF, Martin-Jimenez D, Garcia R. Force reconstruction from tapping mode force microscopy experiments. Nanot 2015;26 185706/1-12.
- [97] Sader JE, Jarvis SP. Accurate formulas for interaction force and energy in frequency modulation force spectroscopy. Appl Phys Lett 2004;84:1801–3.
- [98] Stark M, Stark RW, Heckl WM, Guckenberger R. Inverting dynamic force microscopy: from signals to time-resolved interaction forces. Proc Natl Acad Sci U S A 2002;99:8473–8.
- [99] García R, San Paulo A. Attractive and repulsive tip-sample interaction regimes in tapping-mode atomic force microscopy. PhRvB 1999;60:4961–7.
- [100] Garciá R, San Paulo A. Amplitude curves and operating regimes in dynamic atomic force microscopy. Ultmi 2000;82:79–83.
 [101] Hölscher H, Schwarz UD, Wiesendanger R. Calculation of the frequency shift
- [101] Hölscher H, Schwarz UD, Wiesendanger R. Calculation of the frequency shift in dynamic force microscopy. Appl Surf Sci 1999;140:344–51.
- [102] Kiracofe D, Melcher J, Raman A. Gaining insight into the physics of dynamic atomic force microscopy in complex environments using the VEDA simulator. Rev Sci Instrum 2012;83 013702/1-17.
- [103] Paulo ÁS, García R. Tip-surface forces, amplitude, and energy dissipation in amplitude-modulation (tapping mode) force microscopy. PhRvB 2001;64 193411/1-4.
- [104] Gomez CJ, Garcia R. Determination and simulation of nanoscale energy dissipation processes in amplitude modulation. AFM. Ultmi. 2010;110:626–33.

- [105] Knoll A, Magerle R, Krausch G. Tapping Mode Atomic Force Microscopy on Polymers: Where Is the True Sample Surface? Macromolecules 2001;34:4159–65.
- [106] Tamayo J, Garciá R. Effects of elastic and inelastic interactions on phase contrast images in tapping-mode scanning force microscopy. Appl Phys Lett 1997;71:2394–6.
- [107] Schröter K, Petzold A, Henze T, Thurn-Albrecht T. Quantitative Analysis of Scanning Force Microscopy Data Using Harmonic Models. Macromolecules 2009;42:1114–24.
- [108] Martinez NF, Patil S, Lozano JR, Garcia R. Enhanced compositional sensitivity in atomic force microscopy by the excitation of the first two flexural modes. Appl Phys Lett 2006;89 153115/1-3.
- [109] Dietz C. Sensing in-plane nanomechanical surface and sub-surface properties of polymers: local shear stress as function of the indentation depth. Nanoscale 2017:10:460–8.
- [110] Lozano JR, Garcia R. Theory of multifrequency atomic force microscopy. Phys Rev Lett 2008:100 076102/1-4.
- [111] Kiracofe D, Raman A, Yablon D. Multiple regimes of operation in bimodal AFM: understanding the energy of cantilever eigenmodes. Beilstein J Nanotechnol 2013;4:385–93.
- [112] Herruzo ET, Perrino AP, Garcia R. Fast nanomechanical spectroscopy of soft matter. Nat Commun 2014;5 3126/1-8.
- [113] Gigler AM, Dietz C, Baumann M, Martinez NF, Garcia R, Stark RW. Repulsive bimodal atomic force microscopy on polymers. Beilstein J Nanotechnol 2012;3:456–63.
- [114] Rabe U, Arnold W. Acoustic microscopy by atomic force microscopy. Appl Phys Lett 1994:64:1493-5.
- [115] Yamanaka K, Ogiso H, Kolosov O. Ultrasonic force microscopy for nanometer resolution subsurface imaging. Appl Phys Lett 1994;64:178–80.
- [116] Rabe U, Janser K, Arnold W. Vibrations of free and surface-coupled atomic force microscope cantilevers: Theory and experiment. Rev Sci Instrum 1996;67:3281–93.
- [117] Wright OB, Nishiguchi N. Vibrational dynamics of force microscopy: Effect of tip dimensions. Appl Phys Lett 1997;71:626–8.
- [118] Turner JA, Hirsekorn S, Rabe U, Arnold W. High-frequency response of atomic-force microscope cantilevers. J Appl Phys 1997;82:966–79.
- [119] Rabe U, Amelio S, Kester E, Scherer V, Hirsekorn S, Arnold W. Quantitative determination of contact stiffness using atomic force acoustic microscopy. Ultra 2000;38:430-7.
- [120] Dupas E, Gremaud G, Kulik A, Loubet JL. High-frequency mechanical spectroscopy with an atomic force microscope. Rev Sci Instrum 2001;72:3891-7.
- [121] Turner JA, Wiehn JS. Sensitivity of flexural and torsional vibration modes of atomic force microscope cantilevers to surface stiffness variations. Nanot 2001;12:322–30.
- [122] Hurley DC, Turner JA. Humidity effects on the determination of elastic properties by atomic force acoustic microscopy. J Appl Phys 2004;95:2403–7.
- [123] Rezaei E, Turner JA. Contact resonances of U-shaped atomic force microscope probes. J Appl Phys 2016;119 034303/1-11.
- [124] Hurley DC, Turner JA. Measurement of Poisson's ratio with contact-resonance atomic force microscopy. J Appl Phys 2007;102 033509/1-8.
- [125] Rezaei E, Turner JA. Contact resonance AFM to quantify the in-plane and out-of-plane loss tangents of polymers simultaneously. Appl Phys Lett 2017;110 101902/1-4.
- [126] Jesse S, Kalinin SV, Proksch R, Baddorf AP, Rodriguez BJ. The band excitation method in scanning probe microscopy for rapid mapping of energy dissipation on the nanoscale. Nanot 2007;18 435503/1-8.
- [127] Stan G, King SW, Cook RF. Nanoscale mapping of contact stiffness and damping by contact resonance atomic force microscopy. Nanot 2012;23 215703/1-9.
- [128] Rodriguez BJ, Callahan C, Kalinin SV, Proksch R. Dual-frequency resonancetracking atomic force microscopy. Nanot 2007;18 475504/1-6.
- [129] Gannepalli A, Yablon DG, Tsou AH, Proksch R. Mapping nanoscale elasticity and dissipation using dual frequency contact resonance AFM. Nanot 2011;22 355705/1-8.
- [130] Kos AB, Hurley DC. Nanomechanical mapping with resonance tracking scanned probe microscope. Meas Sci Technol 2008;19 015504/1-9.
- [131] Kos AB, Killgore JP, Hurley DC. SPRITE: a modern approach to scanning probe contact resonance imaging. Meas Sci Technol 2014;25 025405/1-9.
- [132] Pittenger B, Yablon D. Quantitative Measurements of Elastic and Viscoelastic Properties with FASTForce Volume CR. Bruker Application Notes 2017;148:1-7.
- [133] Yablon DG, Grabowski J, Chakraborty I. Measuring the loss tangent of polymer materials with atomic force microscopy based methods. Meas Sci Technol 2014;25 055402/1-7.
- [134] Kiracofe D, Raman A. On eigenmodes, stiffness, and sensitivity of atomic force microscope cantilevers in air versus liquids. J Appl Phys 2010;107 033506/1-9.
- [135] Zhou X, Fu J, Li F. Contact resonance force microscopy for nanomechanical characterization: Accuracy and sensitivity. J Appl Phys 2013;114 064301/1-13.
- [136] Killgore JP, Hurley DC. Low-force AFM nanomechanics with higher-eigenmode contact resonance spectroscopy. Nanot 2012;23 055702/1-10.
- [137] Wagner R, Killgore JP, Tung RC, Raman A, Hurley DC. Vibrational shape tracking of atomic force microscopy cantilevers for improved sensitivity and accuracy of nanomechanical measurements. Nanot 2015;26 045701/1-9.
 [138] Waeytens J, Doneux T, Napolitano S. Evaluating Mechanical Properties of
- [138] Waeytens J, Doneux T, Napolitano S. Evaluating Mechanical Properties of Polymers at the Nanoscale Level via Atomic Force Microscopy-Infrared Spectroscopy. ACS Applied Polymer Materials 2018;1:3–7.

- [139] Chakraborty I, Yablon DG. Temperature dependent loss tangent measurement of polymers with contact resonance atomic force microscopy. Poly 2014:55:1609–12.
- [140] Kocun M, Labuda A, Gannepalli A, Proksch R. Contact resonance atomic force microscopy imaging in air and water using photothermal excitation. Rev Sci Instrum 2015:86 083706/1-5.
- [141] Labuda A, Cleveland J, Geisse NA, Kocun M, Ohler B, Proksch R, et al. Photothermal excitation for improved cantilever drive performance in tapping mode atomic force microscopy. Microscopy and Analysis28 2014;3 S21-S5.
- [142] Proksch R, Kocun M, Hurley D, Viani M, Labuda A, Meinhold W, et al. Practical loss tangent imaging with amplitude-modulated atomic force microscopy. J Appl Phys 2016;119 134901/1-11.
- [143] Nguyen HK, Ito M, Nakajima K. Elastic and viscoelastic characterization of inhomogeneous polymers by bimodal atomic force microscopy. JaJAP 2016;55 08NB6/1-6
- [144] Yuya PA, Hurley DC, Turner JA. Relationship between Q-factor and sample damping for contact resonance atomic force microscope measurement of viscoelastic properties. J Appl Phys 2011;109 113528/1-5.
 [145] Hurley DC, Campbell SE, Killgore JP, Cox LM, Ding Y. Measurement of Viscoelastic properties.
- [145] Hurley DC, Campbell SE, Killgore JP, Cox LM, Ding Y. Measurement of Viscoelastic Loss Tangent with Contact Resonance Modes of Atomic Force Microscopy. Macromolecules 2013;46:9396–402.
- [146] Hutter C, Platz D, Tholen EA, Hansson TH, Haviland DB. Reconstructing nonlinearities with intermodulation spectroscopy. Phys Rev Lett 2010;104 050801/1-4.
- [147] Huang H, Dobryden I, Thorén PA, Ejenstam L, Pan J, Fielden ML, et al. Local surface mechanical properties of PDMS-silica nanocomposite probed with Intermodulation AFM. Compos Sci Technol 2017;150:111–19.
- [148] Haviland DB. Quantitative force microscopy from a dynamic point of view. Current Opinion in Colloid & Interface Science 2017;27:74–81.
- [149] Napolitano S, Glynos E, Tito NB. Glass transition of polymers in bulk, confined geometries, and near interfaces. Rep Prog Phys 2017;80 036602/1-51.
- [150] Moeller G. AFM nanoindentation of viscoelastic materials with large end-radius probes. J Polym Sci, Part B: Polym Phys 2009;47:1573–87.
- [151] Brinson HF, Brinson LC. Time and Temperature Behavior of Polymers. In: Polymer Engineering Science and Viscoelasticity. Boston, MA: Springer US; 2015. p. 231–85.
- [152] Ueda E, Liang X, Ito M, Nakajima K. Dynamic Moduli Mapping of Silica-Filled Styrene-Butadiene Rubber Vulcanizate by Nanorheological Atomic Force Microscopy. Macromolecules 2018;52:311–19.
- [153] Young SL, Chyasnavichyus M, Erko M, Barth FG, Fratzl P, Zlotnikov I, et al. A spider's biological vibration filter: micromechanical characteristics of a biomaterial surface. Acta Biomater 2014;10:4832–42.
- [154] Gołek F, Mazur P, Ryszka Z, Zuber S. AFM image artifacts. Appl Surf Sci. 2014;304:11–19.
- [155] Yacoot A, Koenders L. Aspects of scanning force microscope probes and their effects on dimensional measurement. J Phys D: Appl Phys 2008;41 103001/1-46.
- [156] Jacobs TD, Wabiszewski GE, Goodman AJ, Carpick RW. Characterizing nanoscale scanning probes using electron microscopy: A novel fixture and a practical guide. Rev Sci Instrum 2016;87 013703/1-10.
- [157] Jacobs TDB, Martini A. Measuring and Understanding Contact Area at the Nanoscale: A Review. ApMRv 2017;69:1–18.
- [158] Chung K-H. Wear characteristics of atomic force microscopy tips: A review. International journal of precision engineering and manufacturing 2014;15:2219–30.
- [159] Villarrubia JS. Algorithms for Scanned Probe Microscope Image Simulation, Surface Reconstruction, and Tip Estimation. J Res Natl Inst Stand Technol 1997;102:425–54.
- [160] Flater EE, Zacharakis-Jutz GE, Dumba BG, White IA, Clifford CA. Towards easy and reliable AFM tip shape determination using blind tip reconstruction. Ultmi 2014;146:130-43.
- [161] Dongmo LS, Villarrubia JS, Jones SN, Renegar TB, Postek MT, Song JF. Experimental test of blind tip reconstruction for scanning probe microscopy. Ultmi 2000:85:141–53.
- [162] Jozwiak G, Henrykowski A, Masalska A, Gotszalk T. Regularization mechanism in blind tip reconstruction procedure. Ultmi 2012;118:1–10.
- [163] Tian F, Qian X, Villarrubia JS. Blind estimation of general tip shape in AFM imaging. Ultmi 2008;109:44–53.
- [164] Dokukin ME, Sokolov I. On the Measurements of Rigidity Modulus of Soft Materials in Nanoindentation Experiments at Small Depth. Macromolecules 2012;45:4277–88.
- [165] Liu J, Notbohm JK, Carpick RW, Turner KT. Method for characterizing nanoscale wear of atomic force microscope tips. ACS Nano 2010;4:3763–72.
- [166] Maragliano C, Glia A, Stefancich M, Chiesa M. Effective AFM cantilever tip size: methods for in-situ determination. Meas Sci Technol 2015;26 015002/1-9.
- [167] Santos S, Guang L, Souier T, Gadelrab K, Chiesa M, Thomson NH. A method to provide rapid in situ determination of tip radius in dynamic atomic force microscopy. Rev Sci Instrum 2012;83 043707/1-11.
- [168] Gotsmann B, Lantz MA. Atomistic wear in a single asperity sliding contact. Phys Rev Lett 2008;101 125501/1-4.
- [169] Knoll AW. Nanoscale contact-radius determination by spectral analysis of polymer roughness images. Langmuir 2013;29:13958–66.
- [170] Clifford CA, Seah MP. Quantification issues in the identification of nanoscale regions of homopolymers using modulus measurement via AFM nanoindentation. Appl Surf Sci 2005;252:1915–33.

- [171] Young TJ, Monclus MA, Burnett TL, Broughton WR, Ogin SL, Smith PA. The use of the PeakForceTM quantitative nanomechanical mapping AFM-based method for high-resolution Young's modulus measurement of polymers. Meas Sci Technol 2011;22 125703/1-6.
- [172] Smith DPE. Limits of force microscopy. Rev Sci Instrum 1995;66:3191-5.
- [173] Wastl DS, Weymouth AJ, Giessibl FJ. Optimizing atomic resolution of force microscopy in ambient conditions. PhRvB 2013;87 245415/1-10.
- [174] Wagner R, Moon R, Pratt J, Shaw G, Raman A. Uncertainty quantification in nanomechanical measurements using the atomic force microscope. Nanot 2011;22 455703/1-9.
- [175] Higgins MJ, Proksch R, Sader JE, Polcik M, Mc Endoo S, Cleveland JP, et al. Noninvasive determination of optical lever sensitivity in atomic force microscopy. Rev Sci Instrum 2006;77 013701/1-5.
- [176] Hutter JL, Bechhoefer J. Calibration of atomic-force microscope tips. Rev Sci Instrum 1993:64:1868–73.
- [177] Shaw GA, Kramar J, Pratt J. SI-traceable spring constant calibration of microfabricated cantilevers for small force measurement. ExM 2007;47:143-51.
- [178] Cleveland JP, Manne S, Bocek D, Hansma PK. A nondestructive method for determining the spring constant of cantilevers for scanning force microscopy. Rev Sci Instrum 1993;64:403–5.
- [179] Proksch R, Schäffer TE, Cleveland JP, Callahan RC, Viani MB. Finite optical spot size and position corrections in thermal spring constant calibration. Nanot 2004;15:1344–50.
- [180] Sader JE, Chon JWM, Mulvaney P. Calibration of rectangular atomic force microscope cantilevers. Rev Sci Instrum 1999;70:3967–9.
- [181] Sader JE, Sanelli JA, Adamson BD, Monty JP, Wei X, Crawford SA, et al. Spring constant calibration of atomic force microscope cantilevers of arbitrary shape. Rev Sci Instrum 2012;83 103705/1-16.
- [182] Sader JE, Borgani R, Gibson CT, Haviland DB, Higgins MJ, Kilpatrick JI, et al. A virtual instrument to standardise the calibration of atomic force microscope cantilevers. Rev Sci Instrum 2016;87 093711/1-14.
- [183] Labuda A, Kocun M, Lysy M, Walsh T, Meinhold J, Proksch T, et al. Calibration of higher eigenmodes of cantilevers. Rev Sci Instrum 2016;87 073705/1-12.
- [184] Ohler B. Cantilever spring constant calibration using laser Doppler vibrometry. Rev Sci Instrum 2007;78 063701/1-5.
- [185] Lozano JR, Kiracofe D, Melcher J, Garcia R, Raman A. Calibration of higher eigenmode spring constants of atomic force microscope cantilevers. Nanot 2010;21 465502/1-7.
- [186] Schillers H, Rianna C, Schape J, Luque T, Doschke H, Walte M, et al. Standardized Nanomechanical Atomic Force Microscopy Procedure (SNAP) for Measuring Soft and Biological Samples. Sci Rep 2017;7 5117/1-9.
- [187] Sader JE, Lu J, Mulvaney P. Effect of cantilever geometry on the optical lever sensitivities and thermal noise method of the atomic force microscope. Rev Sci Instrum 2014;85 113702/1-6.
- [188] Hues SM, Draper CF, Lee KP, Colton RJ. Effect of PZT and PMN actuator hysteresis and creep on nanoindentation measurements using force microscopy. Rev Sci Instrum 1994;65:1561–5.
- [189] Holman AE, Scholte PMLO, Heerens WC, Tuinstra F. Analysis of piezo actuators in translation constructions. Rev Sci Instrum 1995;66:3208–15.
- [190] Kindt JH, Thompson JB, Viani MB, Hansma PK. Atomic force microscope detector drift compensation by correlation of similar traces acquired at different setpoints. Rev Sci Instrum 2002;73:2305–7.
- [191] Montgomery D. Design and Analysis of Experiments. New York: John Wiley and Sons Inc.; 2019. p. 688.
- [192] Ebenstein DM, Wahl KJ. A comparison of JKR-based methods to analyze quasi-static and dynamic indentation force curves. J Colloid Interface Sci 2006:298:652–62.
- [193] Benitez R, Moreno-Flores S, Bolos VJ, Toca-Herrera JL. A new automatic contact point detection algorithm for AFM force curves. Microsc Res Tech 2013;76:870-6.
- [194] Dimitriadis EK, Horkay F, Maresca J, Kachar B, Chadwick RS. Determination of Elastic Moduli of Thin Layers of Soft Material Using the Atomic Force Microscope. Biophys J 2002;82:2798–810.
- [195] Rudoy D, Yuen SG, Howe RD, Wolfe PJ. Bayesian change-point analysis for atomic force microscopy and soft material indentation. Journal of the Royal Statistical Society: Series C (Applied Statistics) 2010;59 no-no.
- [196] Melzak KA, Moreno-Flores S, Yu K, Kizhakkedathu J, Toca-Herrera JL. Rationalized approach to the determination of contact point in force-distance curves: application to polymer brushes in salt solutions and in water. Microsc Res Tech 2010:73:959-64.
- [197] Roy R, Chen W, Cong L, Goodell LA, Foran DJ, Desai JP. Probabilistic estimation of mechanical properties of biomaterials using atomic force microscopy. IEEE Trans Biomed Eng 2014;61:547–56.
- [198] Sheridan RJ, Collinson DW, Brinson LC. Vanishing Cantilever Calibration Error with Magic Ratio Atomic Force Microscopy. Advanced Theory and Simulations 2020;3 2000090/1-6.
- [199] Valotteau C, Sumbul F, Rico F. High-speed force spectroscopy: microsecond force measurements using ultrashort cantilevers. Biophysical Reviews 2019;11:689–99.
- [200] Ando T, Uchihashi T, Fukuma T. High-speed atomic force microscopy for nano-visualization of dynamic biomolecular processes. Prog Surf Sci 2008;83:337–437.
- [201] Fantner GE, Schitter G, Kindt JH, Ivanov T, Ivanova K, Patel R, et al. Components for high speed atomic force microscopy. Ultmi 2006;106:881–7.

- [202] Eslami B, López-Guerra EA, Diaz AJ, Solares SD. Optimization of the excitation frequency for high probe sensitivity in single-eigenmode and bimodal tapping-mode AFM. Nanot 2015;26 165703/1-12.
- [203] Martínez NF, García R. Measuring phase shifts and energy dissipation with amplitude modulation atomic force microscopy. Nanot 2006;17 S167-S72.
- [204] Garcia R, Gómez CJ, Martinez NF, Patil S, Dietz C, Magerle R. Identification of Nanoscale Dissipation Processes by Dynamic Atomic Force Microscopy. Phys Rev Lett 2006;97 016103/1-4.
- [205] Rodriguez TR, Garciá R. Tip motion in amplitude modulation (tapping-mode) atomic-force microscopy: Comparison between continuous and point-mass models. Appl Phys Lett 2002;80:1646–8.
- [206] Mertz J, Marti O, Mlynek J. Regulation of a microcantilever response by force feedback. Appl Phys Lett 1993;62:2344–6.
- [207] Adams JD, Erickson BW, Grossenbacher J, Brugger J, Nievergelt A, Fantner GE. Harnessing the damping properties of materials for high-speed atomic force microscopy. Nat Nanotechnol 2016;11:147–51.
- [208] Giessibl FJ. Forces and frequency shifts in atomic-resolution dynamic-force microscopy. PhRvB 1997;56:16010–15.
- [209] Kodera N, Sakashita M, Ando T. Dynamic proportional-integral-differential controller for high-speed atomic force microscopy. Rev Sci Instrum 2006;77 083704
- [210] Tung RC, Killgore JP, Hurley DC. Hydrodynamic corrections to contact resonance atomic force microscopy measurements of viscoelastic loss tangent. Rev Sci Instrum 2013;84 073703/1-7.
- [211] Wagner R, Moon RJ, Raman A. Mechanical properties of cellulose nanomaterials studied by contact resonance atomic force microscopy. Cellu 2016;23:1031–41.
- [212] Hess KM, Killgore JP, Srubar WV. Nanoscale hygromechanical behavior of lignin. Cellu. 2018;25:6345–60.
- [213] Tsukruk VV, Gorbunov VV, Huang Z, Chizhik SA. Dynamic microprobing of viscoelastic polymer properties. Polym Int 2000;49:441–4.
- [214] Pirzer T, Hugel T. Atomic force microscopy spring constant determination in viscous liquids. Rev Sci Instrum 2009;80 035110/1-6.
- [215] Green CP, Sader JE. Frequency response of cantilever beams immersed in viscous fluids near a solid surface with applications to the atomic force microscope. J Appl Phys 2005;98 114913/1-12.
- [216] Janovjak H, Struckmeier J, Muller DJ. Hydrodynamic effects in fast AFM single-molecule force measurements. Eur Biophys J 2005;34:91–6.
- [217] Churnside AB, Tung RC, Killgore JP. Quantitative Contact Resonance Force Microscopy for Viscoelastic Measurement of Soft Materials at the Solid-Liquid Interface. Langmuir 2015;31:11143–9.
- [218] Vahdat V, Carpick RW. Practical method to limit tip-sample contact stress and prevent wear in amplitude modulation atomic force microscopy. ACS Nano 2013;7:9836–50.
- [219] Belec L, Joliff Y. Mechanically affected zone in AFM force measurements Focus on actual probe tip geometry. Materials & Design 2016;104:217–26.
- [220] Oommen B, Van Vliet KJ. Effects of nanoscale thickness and elastic nonlinearity on measured mechanical properties of polymeric films. Thin Solid Films 2006;513:235–42.
- [221] King RB. Elastic analysis of some punch problems for a layered medium. IJSS 1987;23:1657–64.
- [222] Song J, Kahraman R, Collinson DW, Xia W, Brinson LC, Keten S. Temperature effects on the nanoindentation characterization of stiffness gradients in confined polymers. Soft Matter 2019;15:359–70.
- [223] Roduit C, Sekatski S, Dietler G, Catsicas S, Lafont F, Kasas S. Stiffness tomography by atomic force microscopy. Biophys J 2009;97:674–7.
- [224] Collinson DW, Eaton MD, Shull KR, Brinson LC. Deconvolution of Stress Interaction Effects from Atomic Force Spectroscopy Data across Polymer—Particle Interfaces. Macromolecules 2019;52:8940–55.
- [225] Malave V, Killgore JP, Garboczi EJ. Decoupling subsurface inhomogeneities: a 3D finite element approach for contact nanomechanical measurements. Nanot 2019;30 285703/1-13.
- [226] Killgore JP, Kelly JY, Stafford CM, Fasolka MJ, Hurley DC. Quantitative subsurface contact resonance force microscopy of model polymer nanocomposites. Nanot 2011;22 175706/1-7.
- [227] Yao A, Kobayashi K, Nosaka S, Kimura K, Yamada H. Visualization of Au Nanoparticles Buried in a. Polymer Matrix by Scanning Thermal Noise Microscopy. Sci Rep. 2017;7 42718/1-8.
- [228] Zhang CY, Zhang YW, Zeng KY. Extracting the mechanical properties of a viscoelastic polymeric film on a hard elastic substrate. J Mater Res 2004;19:3053–61.
- [229] Garcia PD, Guerrero CR, Garcia R. Nanorheology of living cells measured by AFM-based force-distance curves. Nanoscale 2020;12:9133-43.
- [230] Garcia PD, Garcia R. Determination of the Elastic Moduli of a Single Cell Cultured on a Rigid Support by Force Microscopy. Biophys J 2018;114:2923–32.
- [231] Cappella B, Silbernagl D. Nanomechanical properties of mechanical double-layers: a novel semiempirical analysis. Langmuir 2007;23:10779–87.
- [232] Silbernagl D, Cappella B. Mechanical properties of thin polymer films on stiff substrates. Scanning 2010;32:282–93.
- [233] Kovalev A, Shulha H, Lemieux M, Myshkin N, Tsukruk VV. Nanomechanical Probing of Layered Nanoscale Polymer Films With Atomic Force Microscopy. | Mater Res 2011;19:716–28.
- [234] Tsukruk VV, Sidorenko A, Gorbunov VV, Chizhik SA. Surface Nanomechanical Properties of Polymer Nanocomposite Layers. Langmuir 2001;17:6715–19.

- [235] Gavara N, Chadwick RS. Determination of the elastic moduli of thin samples and adherent cells using conical atomic force microscope tips. Nat Nanotechnol 2012;7:733–6.
- [236] Long R, Hall MS, Wu M, Hui CY. Effects of gel thickness on microscopic indentation measurements of gel modulus. Biophys J 2011;101:643–50.
- [237] Li L, Encarnacao LM, Brown KA. Polymer nanomechanics: Separating the size effect from the substrate effect in nanoindentation. Appl Phys Lett 2017;110 043105/1-5.
- [238] Sakai M. Elastic and viscoelastic contact mechanics of coating/substrate composites in axisymmetric indentation. PMag 2006;86:5607–24.
 [239] Mahaffy RE, Park S, Gerde E, Käs J, Shih CK. Quantitative Analysis of the Vis-
- [239] Mahaffy RE, Park S, Gerde E, Käs J, Shih CK. Quantitative Analysis of the Viscoelastic Properties of Thin Regions of Fibroblasts Using Atomic Force Microscopy. Biophys J 2004;86:1777–93.
- [240] Nguyen HK, Fujinami S, Nakajima K. Size-dependent elastic modulus of ultrathin polymer films in glassy and rubbery states. Poly 2016;105:64–71.
- [241] Bahrami A, Bailly C, Nysten B. Spatial resolution and property contrast in local mechanical mapping of polymer blends using AFM dynamic force spectroscopy. Poly 2019;165:180–90.
- [242] Zlotnikov I, Shilo D, Dauphin Y, Blumtritt H, Werner P, Zolotoyabko E, et al. In situ elastic modulus measurements of ultrathin protein-rich organic layers in biosilica: towards deeper understanding of superior resistance to fracture of biocomposites. RSC Advances 2013;3:5798–802.
- [243] Voigtländer B. Artifacts in AFM. Atomic Force Microscopy. Cham: Springer International Publishing; 2019. p. 137–47.
- [244] Nguyen QD, Chung KH. Effect of tip shape on nanomechanical properties measurements using. AFM. Ultmi. 2019;202:1–9.
- [245] Dokukin ME, Sokolov I. Quantitative mapping of the elastic modulus of soft materials with HarmoniX and PeakForce QNM AFM modes. Langmuir 2012;28:16060-71.
- [246] Chyasnavichyus M, Young SL, Geryak R, Tsukruk VV. Probing elastic properties of soft materials with AFM: Data analysis for different tip geometries. Poly 2016;102:317–25.
- [247] Nguyen HK, Fujinami S, Nakajima K. Elastic modulus of ultrathin polymer films characterized by atomic force microscopy: The role of probe radius. Poly 2016;87:114–22.
- [248] Segedin CM. The relation between load and penetration for a spherical punch. Mat 1957:4:156–61.
- [249] Su D, Li X. Investigation of near-surface mechanical properties of materials using atomic force microscopy. ExM 2014;54:11–24.
- [250] Hillborg H, Tomczak N, Olah A, Schonherr H, Vancso GJ. Nanoscale hydrophobic recovery: A chemical force microscopy study of UV/ozone-treated cross-linked poly(dimethylsiloxane). Langmuir 2004;20:785–94.
- [251] Ievlev AV, Brown C, Burch MJ, Agar JC, Velarde GA, Martin LW, et al. Chemical Phenomena of Atomic Force Microscopy Scanning. Anal Chem 2018;90:3475–81.
- [252] Lo Y-S, Huefner ND, Chan WS, Dryden P, Hagenhoff B, Beebe TP. Organic and Inorganic Contamination on Commercial AFM Cantilevers. Langmuir 1999;15:6522-6.
- [253] Sirghi L, Kylian O, Gilliland D, Ceccone G, Rossi F. Cleaning and hydrophilization of atomic force microscopy silicon probes. J Phys Chem B 2006;110:25975–81.
- [254] Miller EJ, Trewby W, Farokh Payam A, Piantanida L, Cafolla C, Voitchovsky K. Sub-nanometer Resolution Imaging with Amplitude-modulation Atomic Force Microscopy in Liquid. J Vis Exp 2016 e54924/1-10.
- [255] Nie HY, McIntyre NS. Unstable amplitude and noisy image induced by tip contamination in dynamic force mode atomic force microscopy. Rev Sci Instrum 2007;78 023701/1-5.
- [256] Vahdat V, Grierson DS, Turner KT, Carpick RW. Mechanics of interaction and atomic-scale wear of amplitude modulation atomic force microscopy probes. ACS Nano 2013;7:3221–35.
- [257] Chung KH, Lee YH, Kim DE. Characteristics of fracture during the approach process and wear mechanism of a silicon AFM tip. Ultmi 2005;102:161–71.
- [258] Nečas D, Klapetek P. Gwyddion: an open-source software for SPM data analysis. CEJPh 2012;10:181–8.
- [259] Heinze K, Arnould O, Delenne JY, Lullien-Pellerin V, Ramonda M, George M. On the effect of local sample slope during modulus measurements by contact-resonance atomic force microscopy. Ultmi 2018;194:78–88.
- [260] Krämer G, Griepentrog M, Bonaccurso E, Cappella B. Study of morphology and mechanical properties of polystyrene-polybutadiene blends with nanometre resolution using AFM and force-distance curves. Eur Polym J 2014;55:123–34.
- [261] Wilkinson TM, Zargari S, Prasad M, Packard CE. Optimizing nano-dynamic mechanical analysis for high-resolution, elastic modulus mapping in organic-rich shales. JMatS 2014;50:1041–9.
- [262] Odin C, Aimé JP, El Kaakour Z, Bouhacina T. Tip's finite size effects on atomic force microscopy in the contact mode: simple geometrical considerations for rapid estimation of apex radius and tip angle based on the study of polystyrene latex balls. Surf Sci 1994;317:321–40.
- [263] Stan G, Cook RF. Mapping the elastic properties of granular Au films by contact resonance atomic force microscopy. Nanot 2008;19 235701/1-10.
- [264] Munz M, Sturm H, Schulz E, Hinrichsen G. The scanning force microscope as a tool for the detection of local mechanical properties within the interphase of fibre reinforced polymers. Composites Part A: Applied Science and Manufacturing 1998;29:1251–9.
- [265] Tsukruk VV, Huang Z. Micro-thermomechanical properties of heterogeneous polymer films. Poly 2000;41:5541–5.

- [266] Shen J, Zhang D, Zhang F-H, Gan Y. AFM tip-sample convolution effects for cylinder protrusions. Appl Surf Sci 2017;422:482–91.
- [267] Wang D, Fujinami S, Nakajima K, Nishi T. True Surface Topography and Nanomechanical Mapping Measurements on Block Copolymers with Atomic Force Microscopy. Macromolecules 2010;43:3169–72.
- [268] Wang D, Fujinami S, Liu H, Nakajima K, Nishi T. Investigation of True Surface Morphology and Nanomechanical Properties of Poly(styrene-b-ethylene-co-butylene-b-styrene) Using Nanomechanical Mapping: Effects of Composition. Macromolecules 2010;43:9049–55.
- [269] Weisenhorn AL, Khorsandi M, Kasas S, Gotzos V, Butt HJ. Deformation and height anomaly of soft surfaces studied with an AFM. Nanot 1993;4:106–13.
- [270] Weisenhorn A, Kasas S, Solletti J, Khorsandi M, Gotzos V, Roemer D, et al. Deformation observed on soft surfaces studied with an AFM. Proceedings OF SPIE 1993;1855:26–34.
- [271] Cuellar JL, Llarena I, Iturri JJ, Donath E, Moya SE. A novel approach for measuring the intrinsic nanoscale thickness of polymer brushes by means of atomic force microscopy: application of a compressible fluid model. Nanoscale 2013;5:11679–85.
- [272] Mazeran P-E, Odoni L, Loubet J-L. Curvature radius analysis for scanning probe microscopy. Surf Sci 2005;585:25–37.
- [273] Ohashi T, Sato T, Nakajima T, Junkong P, Ikeda Y. Necessity of two-dimensional visualization of validity in the nanomechanical mapping of atomic force microscopy for sulphur cross-linked rubber. RSC Advances 2018:8:32930-41.
- [274] Harton SE, Kumar SK, Yang H, Koga T, Hicks K, Lee H, et al. Immobilized Polymer Layers on Spherical Nanoparticles. Macromolecules. 2010;43:3415–21.
- [275] Cao Y, Duan P, Chen J. Modelling the nanomechanical response of a micro particle-matrix system for nanoindentation tests. Nanot 2016;27 195703/1-10.
- [276] Duan P, Bull S, Chen J. Modeling the nanomechanical responses of biopolymer composites during the nanoindentation. Thin Solid Films 2015;596:277–81.
- [277] Tang G, Galluzzi M, Biswas CS, Stadler FJ. Investigation of micromechanical properties of hard sphere filled composite hydrogels by atomic force microscopy and finite element simulations. J Mech Behav Biomed Mater 2018;78:496–504.
- [278] Clifford CA, Seah MP. Modelling of surface nanoparticle inclusions for nanomechanical measurements by an AFM or nanoindenter: spatial issues. Nanot 2012:23 165704/1-7.
- [279] Chen X, Ashcroft IA, Wildman RD, Tuck CJ. A combined inverse finite element elastoplastic modelling method to simulate the size-effect in nanoin-dentation and characterise materials from the nano to micro-scale. IJSS 2017;104-105:25-34.
- [280] Koumi KE, Nelias D, Chaise T, Duval A. Modeling of the contact between a rigid indenter and a heterogeneous viscoelastic material. Mech Mater 2014;77:28–42.
- [281] Qu M, Deng F, Kalkhoran SM, Gouldstone A, Robisson A, Van Vliet KJ. Nanoscale visualization and multiscale mechanical implications of bound rubber interphases in rubber-carbon black nanocomposites. Soft Matter 2011;7:1066-77.
- [282] Brune PF, Blackman GS, Diehl T, Meth JS, Brill D, Tao Y, et al. Direct Measurement of Rubber Interphase Stiffness. Macromolecules 2016;49:4909–22.
- [283] Zhang M, Li Y, Kolluru PV, Brinson LC. Determination of Mechanical Properties of Polymer Interphase Using Combined Atomic Force Microscope (AFM) Experiments and Finite Element Simulations. Macromolecules 2018;51:8229–40.
- [284] Boccaccio A, Lamberti L, Papi M, De Spirito M, Pappalettere C. Effect of AFM probe geometry on visco-hyperelastic characterization of soft materials. Nanot 2015;26 325701/1-15.
- [285] Fakhraai Z, Forrest JA. Measuring the surface dynamics of glassy polymers. Sci 2008;319:600–4.
- [286] Karim TB, McKenna GB. Comparison of surface mechanical properties among linear and star polystyrenes: Surface softening and stiffening at different temperatures. Poly 2013;54:5928–35.
- [287] Ediger MD, Forrest JA. Dynamics near Free Surfaces and the Glass Transition in Thin Polymer Films: A View to the Future. Macromolecules 2013;47:471–8.
- [288] Vogt BD. Mechanical and viscoelastic properties of confined amorphous polymers. J Polym Sci, Part B: Polym Phys 2018;56:9–30.
- [289] Chai Y, Salez T, Forrest JA. Using Mw Dependence of Surface Dynamics of Glassy Polymers to Probe the Length Scale of Free-Surface Mobility. Macromolecules 2020;53:1084–9.
- [290] Satomi N, Takahara A, Kajiyama T. Determination of Surface Glass Transition Temperature of Monodisperse Polystyrene Based on Temperature-Dependent Scanning Viscoelasticity Microscopy. Macromolecules 1999;32:4474–6.
- [291] Hv Melick, Av Duken, Jd Toonder, Govaert L, Meijer H. Near-surface mechanical properties of amorphous polymers. Philos Mag A 2002;82:2093–102.
- [292] Lorenzoni M, Evangelio L, Verhaeghe S, Nicolet C, Navarro C, Perez-Murano F. Assessing the Local Nanomechanical Properties of Self-Assembled Block Copolymer Thin Films by Peak Force Tapping. Langmuir 2015;31:11630–8.
- [293] Miyake K, Satomi N, Sasaki S. Elastic modulus of polystyrene film from near surface to bulk measured by nanoindentation using atomic force microscopy. Appl Phys Lett 2006;89 031925/1-3.
- [294] Olek M, Kempa K, Jurga S, Giersig M. Nanomechanical Properties of Silica-Coated Multiwall Carbon NanotubesPoly(methyl methacrylate) Composites. Langmuir 2005;21:3146-52.

- [295] Hammerschmidt JA, Gladfelter WL, Haugstad G. Probing Polymer Viscoelastic Relaxations with Temperature-Controlled Friction Force Microscopy. Macromolecules 1999;32:3360-7.
- [296] Kajiyama T, Tanaka K, Takahara A. Analysis of surface mobility in polystyrene films with monodisperse and bimodal molecular weights by lateral force microscopy. J Polym Sci, Part A: Polym Chem 2004;42:639–47.
- [297] Tocha E, Schönherr H, Vancso GJ. Surface relaxations of poly(methyl methacrylate) assessed by friction force microscopy on the nanoscale. Soft Matter 2009;5:1489–95.
- [298] Fu J, Li B, Han Y. Molecular motions of different scales at thin polystyrene film surface by lateral force microscopy. The Journal of Chemical Physics 2005;123 064713.
- [299] Sondhauß J, Lantz M, Gotsmann B, Schirmeisen A. β-Relaxation of PMMA: Tip Size and Stress Effects in Friction Force Microscopy. Langmuir 2015;31:5398–405.
- [300] Evans CM, Deng H, Jager WF, Torkelson JM. Fragility is a Key Parameter in Determining the Magnitude of Tg-Confinement Effects in Polymer Films. Macromolecules 2013;46:6091–103.
- [301] Shavit A, Riggleman RA. Influence of Backbone Rigidity on Nanoscale Confinement Effects in Model Glass-Forming Polymers. Macromolecules 2013;46:5044–52.
- [302] Tanaka K, Takahara A, Kajiyama T. Rheological Analysis of Surface Relaxation Process of Monodisperse Polystyrene Films. Macromolecules 2000;33:7588-93.
- [303] Tweedie CA, Constantinides G, Lehman KE, Brill DJ, Blackman GS, Van Vliet KJ. Enhanced Stiffness of Amorphous Polymer Surfaces under Confinement of Localized Contact Loads. Adv Mater 2007;19:2540–6.
- [304] Qian Z, Risan J, Stadnick B, McKenna GB. Apparent depth-dependent modulus and hardness of polymers by nanoindentation: Investigation of surface detection error and pressure effects. J Polym Sci, Part B: Polym Phys 2018:56:414–28.
- [305] Tracht U, Wilhelm M, Heuer A, Feng H, Schmidt-Rohr K, Spiess HW. Length Scale of Dynamic Heterogeneities at the Glass Transition Determined by Multidimensional Nuclear Magnetic Resonance. Phys Rev Lett 1998;81:2727–30.
- [306] Thurau CT, Ediger MD. Spatially heterogeneous dynamics during physical aging far below the glass transition temperature. J Polym Sci, Part B: Polym Phys 2002;40:2463–72.
- [307] Fragiadakis D, Casalini R, Roland CM. Comparing dynamic correlation lengths from an approximation to the four-point dynamic susceptibility and from the picosecond vibrational dynamics. Phys Rev E Stat Nonlin Soft Matter Phys 2011;84 042501/1-4.
- [308] Nguyen HK, Wang D, Russell TP, Nakajima K. Observation of dynamical heterogeneities and their time evolution on the surface of an amorphous polymer. Soft Matter 2015;11:1425–33.
- [309] Russell EV, Israeloff NE. Direct observation of molecular cooperativity near the glass transition. Natur 2000;408:695–8.
- [310] Wang D, Liu Y, Nishi T, Nakajima K. Length scale of mechanical heterogeneity in a glassy polymer determined by atomic force microscopy. Appl Phys Lett 2012;100 251905/1-4.
- [311] Alisafaei F, Han C-S. Indentation depth dependent mechanical behavior in polymers. Advances in Condensed Matter Physics 2015;391579:1–20.
- [312] Chattaraj S, Pant P, Nanavati H. Inter-relationships between mechanical properties of glassy polymers from nanoindentation and uniaxial compression. Poly 2018;144:128–41.
- [313] Tranchida D, Piccarolo S, Soliman M. Nanoscale Mechanical Characterization of Polymers by AFM Nanoindentations: Critical Approach to the Elastic Characterization. Macromolecules 2006;39:4547–56.
- [314] Mate CM. Tribology on the Small Scale: A Bottom Up Approach to Friction, Lubrication, and Wear. Oxford: Oxford University Press; 2008. p. 331.
- [315] Ikeshima D, Miyamoto K, Yonezu A. Molecular deformation mechanism of polycarbonate during nano-indentation: Molecular dynamics simulation and experimentation. Poly 2019;173:80-7.
- [316] Argon AS. The Physics of Deformation and Fracture of Polymers. Cambridge: Cambridge University Press; 2013. p. 511.
- [317] Samadi-Dooki A, Malekmotiei L, Voyiadjis GZ. Characterizing shear transformation zones in polycarbonate using nanoindentation. Poly 2016;82:238–45.
- [318] Voyiadjis GZ, Malekmotiei L, Samadi-Dooki A. Indentation size effect in amorphous polymers based on shear transformation mediated plasticity. Poly 2018;137:72–81.
- [319] Voyiadjis GZ, Samadi-Dooki A. Constitutive modeling of large inelastic deformation of amorphous polymers: Free volume and shear transformation zone dynamics. J Appl Phys 2016;119 225104/1-9.
- [320] Malekmotiei L, Samadi-Dooki A, Voyiadjis GZ. Nanoindentation Study of Yielding and Plasticity of Poly(methyl methacrylate). Macromolecules 2015;48:5348-57.
- [321] Papakonstantopoulos GJ, Riggleman RA, Barrat JL, de Pablo JJ. Molecular plasticity of polymeric glasses in the elastic regime. Phys Rev E Stat Nonlin Soft Matter Phys 2008;77 041502/1-6.
- [322] Han C-S, Nikolov S. Indentation size effects in polymers and related rotation gradients. J Mater Res 2011;22:1662–72.
- [323] Han C-S. Influence of the molecular structure on indentation size effect in polymers. Materials Science and Engineering: A 2010;527:619–24.
- [324] Asay DB, Kim SH. Effects of adsorbed water layer structure on adhesion force of silicon oxide nanoasperity contact in humid ambient. J Chem Phys 2006;124 174712/1-5.

- [325] Chen L, Gu X, Fasolka MJ, Martin JW, Nguyen T. Effects of Humidity and Sample Surface Free Energy on AFM Probe—Sample Interactions and Lateral Force Microscopy Image Contrast. Langmuir 2009;25:3494–503.
- [326] Sahagún E, García-Mochales P, Sacha GM, Sáenz JJ. Energy Dissipation due to Capillary Interactions: Hydrophobicity Maps in Force Microscopy. Phys Rev Lett 2007;98 176106/1-4.
- [327] Barcons V, Verdaguer A, Font J, Chiesa M, Santos S. Nanoscale Capillary Interactions in Dynamic Atomic Force Microscopy. The Journal of Physical Chemistry C 2012;116:7757–66.
- [328] Verdaguer A, Santos S, Sauthier G, Segura JJ, Chiesa M, Fraxedas J. Water-mediated height artifacts in dynamic atomic force microscopy. Phys Chem Chem Phys 2012;14:16080-7.
- [329] Zitzler L, Herminghaus S, Mugele F. Capillary forces in tapping mode atomic force microscopy. PhRvB 2002;66 155436/1-8.
- [330] Genix AC, Bocharova V, Carroll B, Lehmann M, Saito T, Krueger S, et al. Understanding the Static Interfacial Polymer Layer by Exploring the Dispersion States of Nanocomposites. ACS Appl Mater Interfaces 2019;11:17863-72.
 [331] Zuo B, Zhou H, Davis MJB, Wang X, Priestley RD. Effect of Local Chain Con-
- [331] Zuo B, Zhou H, Davis MJB, Wang X, Priestley RD. Effect of Local Chain Conformation in Adsorbed Nanolayers on Confined Polymer Molecular Mobility. Phys Rev Lett 2019;122 217801/1-7.
- [332] Zhang M, Askar S, Torkelson JM, Brinson LC. Stiffness Gradients in Glassy Polymer Model Nanocomposites: Comparisons of Quantitative Characterization by Fluorescence Spectroscopy and Atomic Force Microscopy. Macromolecules 2017;50:5447-58.
- [333] Cheng X, Putz KW, Wood CD, Brinson LC. Characterization of local elastic modulus in confined polymer films via AFM indentation. Macromol Rapid Commun 2015;36:391–7.
- [334] Tian C, Chu G, Feng Y, Lu Y, Miao C, Ning N, et al. Quantitatively identify and understand the interphase of SiO2/rubber nanocomposites by using nanomechanical mapping technique of AFM. Compos Sci Technol 2019;170:1–6.
- [335] Houssat M, Lahoud Dignat N, Cambronne J-P, Diaham S. AFM Measurements of Polyimide/Silicon Nitride Nanocomposite Interphase. IEEE Transactions on Nanotechnology 2018;17:1146–50.
- [336] Meddeb AB, Tighe T, Ounaies Z, Lopez-Pamies O. Extreme enhancement of the nonlinear elastic response of elastomer nanoparticulate composites via interphases. Composites Part B: Engineering 2019;156:166–73.
- [337] Tian C, Feng Y, Chu G, Lu Y, Miao C, Ning N, et al. Interfacial nanomechanical properties and chain segment dynamics of fibrillar silicate/elastomer nanocomposites. Composites Part B: Engineering 2020;193 108048/1-9.
- [338] Qi Y, Jiang D, Ju S, Zhang J, Cui X. Determining the interphase thickness and properties in carbon fiber reinforced fast and conventional curing epoxy matrix composites using peak force atomic force microscopy. Compos Sci Technol 2019;184 107877/1-7.
- [339] Niu Y-F, Yang Y, Gao S, Yao J-W. Mechanical mapping of the interphase in carbon fiber reinforced poly(ether-ether-ketone) composites using peak force atomic force microscopy: Interphase shrinkage under coupled ultraviolet and hydro-thermal exposure. Polym Test 2016;55:257–60.
- [340] Babu LK, Mishra K, Singh RP. Near-fiber effects of UV irradiation on the fiber-matrix interphase: A combined experimental and numerical investigation. Materials & Design 2018;157:294–302.
- [341] Belec L, Nguyen TH, Nguyen DL, Chailan JF. Comparative effects of humid tropical weathering and artificial ageing on a model composite properties from nano- to macro-scale. Composites Part A: Applied Science and Manufacturing 2015;68:235–41.
- [342] Joliff Y, Rekik W, Belec L, Chailan JF. Study of the moisture/stress effects on glass fibre/epoxy composite and the impact of the interphase area. Compos Struct 2014;108:876–85.
- [343] Yekani Fard M, Raji B, Pankretz H. Time-scale through-thickness interphase in polymer matrix composites including hygrothermal treatment. Polym Test 2020;83 106365/1-9.
- [344] He C, Shi S, Wu X, Russell TP, Wang D. Atomic Force Microscopy Nanomechanical Mapping Visualizes Interfacial Broadening between Networks Due to Chemical Exchange Reactions. J Am Chem Soc 2018;140:6793–6.
- [345] Wang D, Nakajima K, Liu F, Shi S, Russell TP. Nanomechanical Imaging of the Diffusion of Fullerene into Conjugated Polymer. ACS Nano 2017;11:8660-7.
- [346] Wang D, Fujinami S, Nakajima K, Inukai S, Ueki H, Magario A, et al. Visualization of nanomechanical mapping on polymer nanocomposites by AFM force measurement. Poly 2010;51:2455–9.
- [347] Zhang S, Liu H, Gou J, Ying J, Wang Y, Liu C, et al. Quantitative nanomechanical mapping on poly(lactic acid)/poly(ɛ-caprolactone)/carbon nanotubes bionanocomposites using atomic force microscopy. Polym Test 2019;77
- [348] Xavier P, Bose S. Nanomechanical Mapping, Hierarchical Polymer Dynamics, and Miscibility in the Presence of Chain-End Grafted Nanoparticles. Macromolecules 2016;49:1036–48.
- [349] Huang H, Dobryden I, Ihrner N, Johansson M, Ma H, Pan J, et al. Temperature-dependent surface nanomechanical properties of a thermoplastic nanocomposite. J Colloid Interface Sci 2017;494:204–14.
- [350] Megevand B, Pruvost S, Lins LC, Livi S, Gérard J-F, Duchet-Rumeau J. Probing nanomechanical properties with AFM to understand the structure and behavior of polymer blends compatibilized with ionic liquids. RSC Advances 2016;6:96421–30.
- [351] Lorenzoni M, Evangelio L, Fernández-Regúlez M, Nicolet C, Navarro C, Pérez-Murano F. Sequential Infiltration of Self-Assembled Block Copolymers: A Study by Atomic Force Microscopy. The Journal of Physical Chemistry C 2017;121:3078–86.

- [352] Chung PC, Glynos E, Green PF. The elastic mechanical response of supported thin polymer films. Langmuir 2014;30:15200–5.
- [353] Chung PC, Green PF. The Elastic Mechanical Response of Nanoscale Thin Films of Miscible Polymer/Polymer Blends. Macromolecules 2015;48:3991–6.
- [354] Chung PC, Glynos E, Sakellariou G, Green PF. Elastic Mechanical Response of Thin Supported Star-Shaped Polymer Films. ACS Macro Letters 2016:5:439–43.
- [355] Ho K, Kim KS, Gilburd L, Mirzoyan R, de Beer S, Walker GC. Nanoscale Subsurface Morphologies in Block Copolymer Thin Films Revealed by Combined Near-Field Infrared Microscopy and Mechanical Mapping. ACS Applied Polymer Materials 2019;1:933–8.
- [356] Hoppener C, Schacher FH, Deckert V. Multimodal Characterization of Resin Embedded and Sliced Polymer Nanoparticles by Means of Tip-Enhanced Raman Spectroscopy and Force-Distance Curve Based Atomic Force Microscopy. Small 2020:16 e1907418/1-11
- [357] Aziz AH, Wahlquist J, Sollner A, Ferguson V, DelRio FW, Bryant SJ. Mechanical characterization of sequentially layered photo-clickable thiol-ene hydrogels. J Mech Behav Biomed Mater 2017;65:454–65.
- [358] Young TJ, Crocker LE, Broughton WR, Ogin SL, Smith PA. Observations on interphase characterisation in polymer composites by nano-scale indentation using AFM and FEA. Composites Part A: Applied Science and Manufacturing 2013;50:39–43.
- [359] Payton OD, Picco L, Scott TB. High-speed atomic force microscopy for materials science. Int Mater Rev 2016;61:473–94.
- [360] Robertson CG, Lin CJ, Rackaitis M, Roland CM. Influence of Particle Size and Polymer–Filler Coupling on Viscoelastic Glass Transition of Particle-Reinforced Polymers. Macromolecules 2008;41:2727–31.
- [361] Liu RYF, Bernal-Lara TE, Hiltner A, Baer E. Polymer Interphase Materials by Forced Assembly. Macromolecules 2005;38:4819–27.
- [362] Cech V, Palesch E, Lukes J. The glass fiber-polymer matrix inter-face/interphase characterized by nanoscale imaging techniques. Compos Sci Technol 2013;83:22-6.
- [363] Tadiello L, D'Arienzo M, Di Credico B, Hanel T, Matejka L, Mauri M, et al. The filler-rubber interface in styrene butadiene nanocomposites with anisotropic silica particles: morphology and dynamic properties. Soft Matter 2015;11:4022-33.
- [364] Spitzner EC, Riesch C, Magerle R. Subsurface imaging of soft polymeric materials with nanoscale resolution. ACS Nano 2011;5:315–20.
- [365] Spitzner EC, Roper S, Zerson M, Bernstein A, Magerle R. Nanoscale Swelling Heterogeneities in Type I Collagen Fibrils. ACS Nano 2015;9:5683–94.
- [366] Nguyen HK, Liang X, Ito M, Nakajima K. Direct Mapping of Nanoscale Viscoelastic Dynamics at Nanofiller/Polymer Interfaces. Macromolecules 2018;51:6085–91.
- [367] Gonzalez-Martinez JF, Kakar E, Erkselius S, Rehnberg N, Sotres J. Effect of Relative Humidity on the Viscoelasticity of Thin Organic Films Studied by Contact Thermal Noise AFM. Langmuir 2019;35:6015–23.
- [368] Nair SS, Hurley DC, Wang S, Young TM. Nanoscale characterization of interphase properties in maleated polypropylene-treated natural fiber-reinforced polymer composites. Polymer Engineering & Science 2013;53:888–96.
- [369] Nair SS, Wang S, Hurley DC. Nanoscale characterization of natural fibers and their composites using contact-resonance force microscopy. Composites Part A: Applied Science and Manufacturing 2010;41:624–31.
- [370] Zhou X, Fu J, Li Y, Li F. Nanomechanical mapping of glass fiber reinforced polymer composites using atomic force acoustic microscopy. J Appl Polym Sci 2014;131:1–10.

- [371] Diaz AJ, Noh H, Meier T, Solares SD. High-stress study of bioinspired multifunctional PEDOT:PSS/nanoclay nanocomposites using AFM, SEM and numerical simulation. Beilstein | Nanotechnol 2017;8:2069–82.
- [372] Zhang W, Chen Y, Hou Y, Wang W, Liu H, Zheng L. Subsurface imaging of rigid particles buried in a polymer matrix based on atomic force microscopy mechanical sensing. Ultmi 2019;207 112832/1-8.
- [373] Reggente M, Passeri D, Angeloni L, Scaramuzzo FA, Barteri M, De Angelis F, et al. Detection of stiff nanoparticles within cellular structures by contact resonance atomic force microscopy subsurface nanomechanical imaging. Nanoscale 2017;9:5671–6.
- [374] Wang W, Ma C, Chen Y, Zheng L, Liu H, Chu J. Subsurface imaging of flexible circuits via contact resonance atomic force microscopy. Beilstein J Nanotechnol 2019;10:1636–47.
- [375] Campbell SE, Ferguson VL, Hurley DC. Nanomechanical mapping of the osteochondral interface with contact resonance force microscopy and nanoindentation. Acta Biomater 2012;8:4389–96.
- [376] Natali M, Passeri D, Reggente M, Tamburri E, Terranova ML, Rossi M. Contact resonance atomic force microscopy for viscoelastic characterization of polymer-based nanocomposites at variable temperature. AIP Conf Proc 2016;1749 020008/1-8
- [377] Cheng S, Bocharova V, Belianinov A, Xiong S, Kisliuk A, Somnath S, et al. Unraveling the Mechanism of Nanoscale Mechanical Reinforcement in Glassy Polymer Nanocomposites. Nano Lett 2016;16:3630-7.
- [378] Kassa HG, Stuyver J, Bons A-J, Haviland DB, Thorén P-A, Borgani R, et al. Nano-mechanical properties of interphases in dynamically vulcanized thermoplastic alloy. Poly 2018;135:348–54.
- [379] Ebeling D, Eslami B, Solares Sde J. Visualizing the subsurface of soft matter: simultaneous topographical imaging, depth modulation, and compositional mapping with triple frequency atomic force microscopy. ACS Nano 2013;7:10387–96.
- [380] George J, Azad LB, Poulose AM, An Y, Sarmah AK. Nano-mechanical behaviour of biochar-starch polymer composite: Investigation through advanced dynamic atomic force microscopy. Composites Part A: Applied Science and Manufacturing 2019;124 105486/1-9.
- [381] Kumar S, Falzon BG, Kun J, Wilson E, Graninger G, Hawkins SC. High performance multiscale glass fibre epoxy composites integrated with cellulose nanocrystals for advanced structural applications. Composites Part A: Applied Science and Manufacturing 2020;131 105801/1-12.
- [382] Al-Rekabi Z, Contera S. Multifrequency AFM reveals lipid membrane mechanical properties and the effect of cholesterol in modulating viscoelasticity. Proc Natl Acad Sci U S A 2018;115:2658–63.
- [383] Shalabaeva V, Bas AC, Piedrahita-Bello M, Ridier K, Salmon L, Thibault C, et al. Direct Visualization of Local Spin Transition Behaviors in Thin Molecular Films by Bimodal AFM. Small 2019;15 e1903892/1-6.
- [384] Sun Y, Vu LH, Chew N, Puthucheary Z, Cove ME, Zeng K. A Study of Perturbations in Structure and Elastic Modulus of Bone Microconstituents Using Bimodal Amplitude Modulated-Frequency Modulated Atomic Force Microscopy. ACS Biomaterials Science & Engineering 2018;5:478–86.
- [385] Guzman HV, Garcia PD, Garcia R. Dynamic force microscopy simulator (dForce): A tool for planning and understanding tapping and bimodal AFM experiments. Beilstein | Nanotechnol 2015;6:369-79.